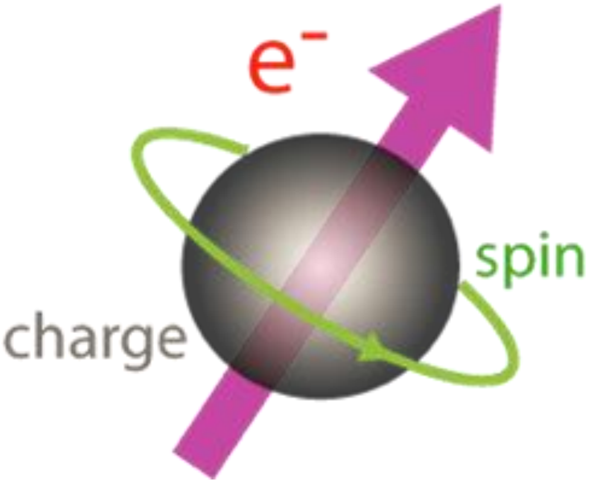

Electrical Spin Injection into p-type Silicon using SiO_2- Cobalt Tunnel Devices: The Role of Schottky Barrier

Thesis for Erasmus Mundus Master of Science in
Nanoscience and Nanotechnology

RAVI SHARMA DULAL

Department of Microtechnology and Nanoscience – MC2
Quantum Device Physics Laboratory
CHALMERS UNIVERSITY OF TECHNOLOGY
Göteborg, Sweden, 2012

Thesis for the Master's degree of Science in Erasmus Mundus Master programme in
Nanoscience and Nanotechnology

Electrical Spin Injection into p-type Silicon using SiO_2- Cobalt Tunnel Devices: The Role of Schottky Barrier

Ravi Sharma Dulal

Promotor: Dr. Saroj Prasad Dash
Co-promotor: Dr. Michel Houssa
Daily superviser: Mr. André Dankert
Examiner: Dr. Thilo Bauch

KATHOLIEKE UNIVERSITEIT
LEUVEN

CHALMERS

Quantum Device Physics Laboratory
Department of Microtechnology and Nanoscience (MC2)
Chalmers University of Technology
Göteborg, Sweden, 2012

This Master thesis is conducted in the framework of the Erasmus Mundus Master programme in Nanoscience and Nanotechnology

Electrical Spin Injection into p-type Silicon using SiO_2- Cobalt Tunnel Devices: The Role of Schottky Barrier

Ravi Sharma Dulal

©Ravi Sharma Dulal, 2012

Thesis work carried out at:
Quantum Device Physics Laboratory
Department of Microtechnology and Nanoscience (MC2)
Chalmers University of Technology, SE-412 96 Göteborg, Sweden

Promotor:
Dr. Saroj Prasad Dash
Department of Microtechnology and Nanoscience (MC2)
Chalmers University of Technology, SE-412 96 Göteborg, Sweden
Telephone: +46 31 772 5170

Co-promotor:
Dr. Michel Houssa
Faculty of Science – Semiconductor Physics Section
Katholieke Universiteit Leuven, B-3001 Leuven, Belgium
Telephone: +32 16 3 27291

Daily supervisor:
Mr. André Dankert
Department of Microtechnology and Nanoscience (MC2)
Chalmers University of Technology, SE-412 96 Göteborg, Sweden
Telephone: +46 31 772 3471

Examiner:
Dr. Thilo Bauch
Department of Microtechnology and Nanoscience (MC2)
Chalmers University of Technology, SE-412 96 Göteborg, Sweden
Telephone: +46 31 772 3397

Cover picture: Electron with charge e^- and spin

Printed by Chalmers Reproservice
Göteborg, Sweden 2012

Acknowledgement

I would like to express my sincere gratitude and indebtedness to my supervisor Dr. Saroj P. Dash for his invaluable guidance and constant motivation to complete my thesis work. He was always available for discussions and I am thankful for your high expertise in this Si spintronic field, which has been a privilege to do research.

I would also like to thank André Dankert who guided me for all the fabrication steps and electrical measurements. He has always inspired me in learning and doing work systematically and efficiently. I also take profound privilege to express my sincere gratitude to Dr. Michel Houssa, who guided me as a co-promoter from KU Leuven. I would also like to convey my special thanks to my coordinators of EMM-Nano program from KU Leuven, Dr. Guido Groeseneken and from Chalmers University, Dr. Göran Johansson. I would also like to convey my deep gratitude to my examiner Dr. Thilo Bauch who kindly accepted to be the examiner of my thesis work.

I also want to thank all the MC2 staffs from Quantum Device Physics group and Nanofabrication laboratory in Chalmers University who provided me great assistance in various ways. I would like to appreciate my colleagues from Chalmers University for their generous support.

Finally, I would like to thank my parents, for their inspiration, support and appreciation towards my pursuit of higher education.

Abstract

Spin angular momentum of electronic charge carriers is being explored currently for integration of non-volatile memory and processor in a single device. The main challenges in this research field are to integrate a spin polarized electron source to a semiconductor, and demonstrate an efficient spin injection, detection, transport, and manipulation mechanisms in such devices. At present, a large research effort is being dedicated to realize silicon based spintronic devices, because of its industrial dominance and expected long spin coherence length. Recently, it has been possible to inject and detect spin polarized electrons into silicon from a ferromagnet at room temperature. This has created possibilities to further investigate and understand the behavior of spin accumulation and depolarization in semiconductors with more details.

This thesis aims to investigate the effect of the Schottky barrier, present at the interface, on spin injection and spin accumulation in silicon. Both electrical and spin transport measurements were performed on microfabricated Cobalt/SiO_2 tunnel barrier/p-type silicon devices. SiO_2 tunnel barrier was grown by ozone oxidation that gives a much better interface because of the creation of very thin transition region, which makes it a robust method for high quality, extremely thin oxide layers. The Schottky barrier parameter has been tailored by changing the boron doping concentration in the silicon. These studies involve determining the carrier densities, mobility, diffusion coefficients, etc. in differently doped silicon substrates using Hall measurement technique, the Schottky barrier properties at the tunnel junction interfaces, as well as the change in the spin-signal with a magnetic field, temperature, and applied electrical bias voltage. With increasing the Schottky barrier width, a transition from direct spin polarized tunneling to an anomalous tunneling could be observed, giving rise to a change in the sign of spin accumulation. For the devices with larger Schottky barrier width, the effect of defects at the semiconductor/tunnel barrier interfaces on the spin injection and detection mechanism were discussed. The Schottky barrier resistance is found to determine the spin transport behavior, which can be dominated by either direct tunneling or two-step tunneling. The role of local spin dipole formation at the interface during spin extraction process with two step tunneling has also been proposed.

Table of Contents

Acknowledgement iii

Abstract v

Table of Figures xi

1. Introduction & Motivation 1

1.1. Introduction 1

1.2. Motivation 2

1.3. Outline 4

2. Semiconductor spintronics 5

2.1 Spintronics 5

  2.1.1. Semiconductor Spintronics 6

2.2. Spin polarized current using ferromagnet 7

2.3. Spin Injection in Semiconductors 9

  2.3.1. Spin injection in Si via tunneling 12

  2.3.2 Effect of Schottky barrier and contact resistance – Doping dependence 13

2.4. Manipulation of Spin Accumulation 15

  2.4.1 Manipulation of spins by external magnetic field 16

  2.4.2 Theoretical description of Hanle effect 17

  2.4.3 Inverted Hanle effect 19

2.5. Spin Detection 20

2.6. Spin relaxation and dephasing in semiconductors 21

  2.6.1. Spin Orbit Coupling 21

  2.6.2 Main spin relaxation mechanisms 22

2.7 Schottky barrier 23

3. Device Fabrication 26

3.1 Fabrication 26

3.1. 1. Wafer Cleaning 26

3.1.2. Photolithography 27

3.1.2.1. Surface Preparation 27

3.1.2.2. Photoresist layer 28

3.1.2.3. Resist Exposure & Development 28

3.1.3. Oxide Etching 28

3.1.4. Silicon Oxidation: The Tunnel Barrier & Pad Oxide 28

3.1.4.1. Thermal Oxidation 29

3.1.4.2. Ozone Oxidation 30

3.1.5. Physical vapor deposition (PVD): Ferro-magnet /Gold contacts 31

3.1.5.1. E-beam evaporation 31

3.1.5.2. Ion beam etching – Contact definition 32

3.2. Device Fabrication Process Steps 33

3.1.1. Wafer cleaning & Thermal oxidation 33

3.1.2. Contact hole etching: Mask 1 34

3.1.3. Tunnel barrier, Ferro Magnet (Co) and Gold (Au) deposition and Contact patterning: Mask 2 34

3.1.4. Contact pads deposition and patterning: Mask 3 36

4. Measurements and Discussions 38

4.1. Hall measurement 38

4.1.1. Resistivity measurement 40

4.1.2. Doping concentration, mobility and diffusion coefficients 43

4.2. Schottky barrier height and width 43

4.3. Hanle measurement : Spin accumulation and detection 46

4.3.1. Very highly doped p++ Silicon 47

4.3.1.1. Spin Lifetime & Diffusion length 47

4.3.1.2. High Spin Polarization 48

4.3.1.3. Temperature dependence Spin accumulation 49

4.3.1.4. Bias dependence plot 50

4.3.2. Doping dependence – Schottky barrier width variation 53

4.3.2.1. Medium doped p+ Silicon 54

4.3.2.2. Low doped p Silicon 57

4.3.2.4. Very low doped p- Silicon 59

4.3.2.5. Detailed comparison – Doping dependence 61

4.3.3 Role of Localized states at the interface 62

4.3.2.1 Proposed reason for spin reversal during extraction 66

4.3.2.1. Tunneling between Ferromagnet and Localized states 68

5. Conclusions & Outlook 71

Bibliography 73

Table of Figures

Figure 2.1. Description of Julliere's model of TMR in MTJ. Thin insulator between two ferromagnet provides spin dependent tunneling. When magnetization of both ferromagnets are parallel, majority spin of one ferromagnet find state in another ferromagnet, leads to low resistance. When antiparallel, unavailability of states leads to high resistance. 5

Figure 2.2. Spin transistor, one ferromagnet is used as injector and other as detector. Gate is used to manipulate the spin accumulation so that it can have two states, accumulated state and relaxed state. 7

Figure 2.3. Current polarization at the FM/SC interface, for direct FM-SC contact, spin polarization is reduced rapidly at the interface from ferromagnet side due to high conductance mismatch that leads to the spin flipping [19]. 9

Figure 2. 4. a. Spin injection without tunnel barrier (diffusive regime) b. Spin injection with tunnel barrier (tunneling regime) 10

Figure 2.5. (a) Schematic energy band diagram of electrical spin injection in an FM/I/Si contact for lowly doped Si, thicker Schottky barrier. *V* is the bias voltage. The dashed lines show the Fermi energy. Here, electron with higher thermal energy are tunneling (b) Schematic energy band diagram depicting the electrical spin accumulation by splitting of energy bands by $\Delta\mu = \mu_{up} - \mu_{down}$ in an FM/I/Si contact for a highly doped Si, thinner Schottky barrier, with direct tunneling dominated [9]. 11

Figure 2.6. Effect of contact resistance for spin-tunnel devices: Computed normalized magneto-resistance of a two-terminal FM/I/Si/I/FM spin-MOSFET against the contact resistance of the tunnel interface at 300K for spin lifetime of a. 100 ps b. 1 ns 14

Figure 2.7. MR Vs. contact resistance for different value of Si channel thickness between two FMs in spin-MOSFET. For smaller thickness, there is larger MR and also wider contact resistance window. Spin lifetime was assumed to be 1 ns. 15

Figure 2.8. A characteristic Hanle curve with highest spin accumulation at B=0 and Lorentzian decrease in accumulation of spin signal as the perpendicular magnetic field is increased. At higher magnetic field, it is reaching equilibrium condition with no polarization. 16

Figure 2.9. a. Energy band diagram showing electron spin injection into conduction band, accumulation of majority spin causes spin splitting of electrochemical potential; b. Hanle

effect observed at room temperature for n type Si with Al_2O_3 tunnel barrier, spin accumulation decreasing with increase in magnetic field that causes spin precession [9]. 19
Figure 2.10. Precession of spin in semiconductor near a ferromagnetic tunnel interface: (a) Illustration of inhomogeneous local magnetostatic fields arising from the roughness. (b) Hanle curves of $Si.Al_2O_3$/ferromagnet devices with different ferromagnetic electrodes. (c) Hanle and Inverted Hanle effect [32] 20
Figure 2.11. Band diagram of metal and semiconductor a. before contact b. after close contact with each other. Valence band and conduction band will be at the same distance from the Fermi level and also due to high density of states in metal, Fermi level remains constant. So, there is band bending when Fermi level aligned at the same level after reaching equilibrium condition.......... 24

Figure 3.1. A Thermal Oxidation Chamber, it use either water vapor (usually UHP steam) or molecular oxygen as the oxidant; called as *wet* oxidation and *dry* oxidation respectively...... 29
Figure 3.2. Ozone oxidation (a) Oxidation configuration, (b) Pictorial representation of oxidation at Si surface by ozone molecule [39] 30
Figure 3.3. E-Beam Evaporation [41], It consists of a vacuum chamber, where the substrate is loaded upside down on a holder. An electron arc acts as the source of e-beam. A high voltage is applied between the crucible and the electron gun. The electrons from the arc are focused on to the crucible by using a perpendicular magnetic field and it vaporizes the metal to deposit over substrate.......... 32
Figure 3.4. The Ion Beam Etching chamber [42], the chamber is pumped to very low vacuum. Ar gas is pumped via the inlet and is ionized. The ionized Ar is accelerated using a high electric field and the accelerated beam is collimated to get a highly directional beam. The high energy beam hits the substrate etching the exposed material.......... 33
Figure 3.5. Contact hole etching, first UV lithography process is done and then, BHF is used to etch out the exposed SiO_2 part. 34
Figure 3.6. Tunnel barrier deposition by Ozone oxidation and Ferro-magnet/gold contact deposition by e-beam evaporation.......... 35
Figure 3.7. Ferro-magnet/gold contact patterning, UV lithography followed by ion beam etching 36
Figure 3.8. Contact pads definition, lift off method is used to pattern the contact pads......... 37

Figure 4.1. Hall bar structure for Hall effect measurement and resistivity measurement. Current is passed along x-direction from A to E. For Hall effect measurement, magnetic field is applied in z-direction and voltage can be measured between contacts B-H, C-G or D-F. ... 39

Figure 4.2. Plot between magnetic field, B Vs. Hall voltage, V_H; magnetic field was swept for hall voltage measurement and slope dV_H/dB was used to get mobility of Si with different doping concentrations. 40

Figure 4.3. Resistivity measurement using four point probe method. Hall bar structure was used. Current was passed from contact A to E. For resistivity measurement, no magnetic field is applied and voltage can be measured between different possible combination of contacts along the same side of bar. 40

Figure 4.4. Plot between Current, I and Votage, V. Voltage is swept to measure corresponding current and resistance R was found by taking the inverse of the slope dI/dV to obtain resistivity of Si with different doping concentrations. 41

Figure 4.5. Wires are connected along the edges of four corners of Si substrate for VDP measurement........ 42

Figure 4.6. $Log_{10}I$ Vs. V plot. Line intercept which is extended from the higher forward bias $log_{10}I$ Vs. V plot to V=0 gives saturation current. 44

Figure 4.7. $Log\left[\frac{I_{sat}}{A.A^{*}T^{2}}\right]$ Vs. $\frac{1}{T}$ plot from which we can calculate the slope that gives SBH after multiplying with K_B. 45

Figure 4.8. Three terminal device, where middle electrode is FM/TB/Si contact which is used for both injection/extraction and detection, outer two electrodes are reference gold contact used for current injection/extraction and voltage detection separately. Size of middle contact is 200 μm x 100 μm........ 47

Figure 4.9. a. Hanle Lorentzian curve of spin injection for Co/Oz. SiO2/p++ Si at -800 mV bias and the amplitudes was found to be 850 μV from the Lorentzian fit; b. spin injection during reverse biased condition shown with band diagram. 48

Figure 4.10. a. Hanle Lorentzian curve of spin extraction for Co/Oz. SiO2/p++ Si at +800 mV bias and the amplitudes was found to be 220 μV from the Lorentzian fit; b. spin extraction during forward biased condition shown with band diagram. 49

Figure 4.11. Temperature dependence of spin signal, a. Hanle signal at -200 mV, injection, variation with T, b. Spin RA variation with T, c. Spin RA amplitude variation with T 50

Figure 4.12. Bias dependence plots for Co/Oz. SiO2/p++ Si device, (a) Variation of spin signals with bias voltage for Co/SiO2/p++Si, measured at 295 K. Bias asymmetry Hanle signal amplitude is shown, (b) Spin RA product $\Delta \boldsymbol{V}/\boldsymbol{J}$,which is showing bias asymmetry feature. (c) Spin polarization varying with bias. It is linearly increase with bias, significantly during injection but slowly during extraction. (d) Normalized TSP2 at room temperature (e) Spin lifetime variation with bias. 52

Figure 4.13. Two-step tunneling via localized states at the interface in parallel with direct tunneling [51]. For two-step tunneling transport, R_1 is the resistance for the current transport between FM and localized state while R_2 is the resistance for the current transport between localized state and Si. R_{tun} is the tunneling resistance for direct tunneling current. 54

Figure 4.14. Hanle Lorentzian curve for spin injection and extraction for Co/Oz. SiO2/p+ Si at (-/+)800 mV bias showing normal spin signal and at +40 mV bias showing spin reversal. However, all spin reversal signals were noisy and extracted life-times were also less compared to normal signal. 54

Figure 4.15. Bias dependence plots for Co/Oz. SiO2/p+ Si, (a) Variation of spin signals with bias voltage for Co/SiO2/p+ Si, measured at 295 K. Bias asymmetry Hanle signal amplitude and spin signal reversal are shown, (b) Spin RA product $\Delta \boldsymbol{V}/\boldsymbol{J}$,which is showing bias asymmetry feature. (c) Spin polarization varying with bias. It is linearly increase with bias, significantly during injection but slowly during extraction. (d) Normalized TSP^2 at room temperature (e) Spin lifetime variation with bias. 56

Figure 4.16. Hanle Lorentzian curve for spin injection and extraction for Co/Oz. SiO2/p+ Si at (-/+)800 mV bias showing normal spin signal and at (-/+)40 mV bias showing spin reversal, a. Normal spin extraction at 800 mV bias b. Spin reversal at 200 mV c. Normal spin injection at -800 mV bias d. Spin reversal at -200 mV. 57

Figure 4.17. Bias dependence plots for Co/Oz. SiO2/p+ Si, (a) Variation of spin signals with bias voltage for Co/SiO2/p++Si, measured at 295 K. Bias asymmetry Hanle signal amplitude and spin signal reversal are shown, (b) Spin RA product $\Delta \boldsymbol{V}/\boldsymbol{J}$,which is showing bias asymmetry feature. (c) Spin polarization varying with bias. It is linearly increase with bias, significantly during injection but slowly during extraction. (d) Normalized TSP^2 at room temperature (e) Spin lifetime variation with bias. 58

Figure 4.18. Hanle plot for spin extraction from sample Co/Oz. SiO_2/p-Si interface at room temperature. Applied bias voltage is 500 mV and Hale signal amplitude ΔV, is found to be 140 V. Spin lifetime calculated from HWHM was 63 ps. 60

Figure 4.19. Hanle plot for spin extraction from sample Co/Oz. SiO_2/p- Si interface showing sign reversal Hanle signal at a. bias 100 mV b. bias 200 mV and normal Hanle signal at c. bias 500 mV 60

Figure 4.20. Comparison between three different doping samples for a. Bias dependent Hanle signal, b. Bias dependent spin RA signal, c. Bias dependent spin polarization, d. Bias dependent normalized TSP^2, e. Bias dependent junction resistance, f. Bias dependent spin lifetime. 62

Figure 4.21. Spin hole injection from ferromagnet to semiconductor. During spin current injection, majority spin accumulation(↑) occurs in both localized states at the interface and semiconductor channel below the interface which leads to the enhanced Hanle signal amplitude. 64

Figure 4.22. Spin hole extraction from semiconductor to ferromagnet. During spin current extraction, we extract majority spin holes from semiconductor to ferromagnet by both direct and sequential tunneling. However, spin accumulation in the semiconductor channel below the interface is due to minority spin (↓) whereas spin accumulation in the localized states at the interface can also be due to majority spin (↑). 65

Figure 4.23. Three different cases for spin transport in FM/TB/SC device, 1. Direct tunneling between FM and Si, 2. Two-step tunneling, 3. Tunneling between FM and Localized states. 69

Chapter 1

Introduction & Motivation

1.1. Introduction

It is well known in scientific and engineering communities that Moore's law has now faces great challenges to meet its target. The scaling down of silicon based CMOS transistors has almost reached to its ultimate physical limitation and is expected to be ceased within the next decade. So, scientists have been forced to explore alternative materials and innovative solutions which can supplement to or extend, or even substitute existing technology. One of the most promising & emerging fields is semiconductor spintronics which takes advantage of the confluence of magnetics and semiconductor electronics in the newly emerging discipline of spin electronics. Semiconductor and Ferro-magnets have complementary properties; however they are used as the materials of information technology separately.

Spintronics is a field which uses the spin angular momentum as the functional unit rather than charge. An electron can rotate around its own axis which can be either clockwise or anticlockwise with constant frequency. This quantum property can be represented as two spin states of spin-up (+1/2) and spin-down (-1/2) respectively and can also be assigned as ‘0’ and ‘1’ states in logical operation. Mott proposed a two spin channel in 1936, stating that the electrical conductivity in ferromagnetic metals can be described in terms of two independent conducting channel [1] [2], corresponding to the spin-up and spin-down electrons which was confirmed, quantified and modeled around 1970 [3] [4].

With the discovery of gaint magneto-resistance (GMR) in metallic layers by A. Fert and P. Grunberg in 1988, new avenue towards spintronics research field was triggered which has led to tremendous storage capacity of hard disks and magnetic random access memories (MRAM) today. Then, a canonical spin transistor proposed by Datta and Das [5] in 1990s has motivated many researchers about the concept of combining both memory and logic on the same device in order to solve the current issues of high power consumption and slow speeds and remarkable improvements have been done so far.

In 1968, spin polarization of the electrons in Si was induced by Lampel where he illuminated the material with circularly polarized light [6]. However, this creation of spin by optical methods is not very efficient in Si (only few percent of spin polarization) because of having indirect band gap for which the carrier recombination time is much larger than the spin relaxation time that limits the steady-state spin polarization to a few percent. In my thesis work, electrical method was used to create the spin accumulation which is more efficient in case of Si.

Ferro-magnets are accompanied with non-volatile functionality at room temperature and also their magnetization can be switched rapidly with unlimited endurance. Whereas, semiconductor provides amplification and transistor action and it’s properties can be controlled by doping density and type of doping, by light and by electrostatic gates [7]. We can build low dimensional hetero-structures by band gap engineering technique. By integrating both Ferro-magnets and semiconductors, i.e. memory and logic computing, we can have possibility of getting superior devices.

Several spin based semiconductor devices have been proposed so far. However, they exist only in theory. Meticulous behavior of many parameters is still need to explore and only few basic characteristics and operation mechanisms are partially understood. Groundbreaking achievements have been made in silicon spintronics in the past five years. In 2007, first electrical spin injection in silicon at low temperature was reported by Jonker et al [8]. Optical detection method was used by using a light emitting diode (LED) structure in which injected spin-polarized carriers recombine with holes generating circularly polarized light. In 2009, Dash et. al. did breakthrough in demonstrating the electrical creation, detection and manipulation of spin polarization in both n-type and p-type silicon (Si) at room temperature [9]. Dash et. al. used $Ni_{80}Fe_{20}$ as Ferro-Magnet, Al_2O_3 as tunnel barrier and highly doped silicon in order to mitigate the depletion layer issue. After that, many researchers shift towards heavily doped Si and different types of researches have been done in silicon spintronics so far. Jeon et. al. successfully demonstrated spin polarization in Germanium at room temperature using crystalline MgO tunnel barrier and CoFe as Ferro-magnet [10].

1.2. Motivation

The main motivation behind interest in studying spintronics in silicon is twofold. Firstly, silicon is the mainstream semiconductor material, being used by industries all over the world.

Thus, development of devices based on spintronics does not need large financial investments as same fabrication facilities can be utilized for them. The robustness and longevity of spin, because of its weak coupling to other degrees of freedom in the material, is another reason behind gaining interest in Si spintronics. The low atomic mass & crystal inversion symmetry results in a very weak coupling to spin relaxation effects, like hyperfine interaction and spin orbit interaction, helps to maintain spin-degenerate bands, which in turn results in better spin polarization/accumulation & higher spin detection signals.

Different types of measurements and comparisons have been done in n-type silicon so far. However, to realize the spin transistor logic gate, we also require complementary device. That means, we need to give same emphasis to p-type silicon as well. Another main reason of using p-type Si was to see doping dependence measurement to see the effect of Schottky barrier resistance on spin behavior. In n type Si, using SiO_2 tunnel barrier, Schottky barrier height was found to be much larger than that in p-type, so doping dependence measurements were not suitable in n-type Si. In this thesis, I did experiments for three terminal Hanle measurements for p-type silicon with different doping concentrations. Three terminal devices allow a detailed study of spin transport between a Ferro-magnet and silicon. Also, ozone oxidized SiO_2 tunnel barrier was used because of presence of very good interface with less transition region at the interface. We expect to have very low interface defect density at Ozone oxidized SiO_2-silicon interface.

This thesis aims to investigate the effect of the Schottky barrier, present at the interface, on spin injection and spin accumulation in silicon. Both electrical and spin transport measurements were performed on microfabricated Cobalt/SiO_2 tunnel barrier/p-type silicon devices. The Schottky barrier parameter has been tailored by changing the boron doping concentration in the silicon. These studies involve determining the carrier densities, mobility, diffusion coefficients, etc. in differently doped silicon substrates using Hall measurement technique, the Schottky barrier properties at the tunnel junction interfaces, as well as the change in the spin-signal with a magnetic field, temperature, and applied electrical bias voltage. With increasing the Schottky barrier width, a transition from direct spin polarized tunneling to an anomalous tunneling could be observed, giving rise to a change in the sign of spin accumulation. For the devices with larger Schottky barrier width, the effect of localized states at the semiconductor/tunnel barrier interfaces on the spin injection and detection mechanisms were discussed.

1.3. Outline

This thesis describes about the spintronic fundamental theory, fabrication procedures, measurement techniques and discussions of the results. In chapter 2, basic theory of semiconductor spintronic, electrical creation of spin accumulation and detection mechanism, manipulation of spin signal by Hanle effect and some spin relaxation mechanisms were discussed. In Chapter 3, fabrication procedures are discussed step-wise and the advantages of using ozone oxidized SiO_2 tunnel barrier are also mentioned.

Finally, characterization results are shown in Chapter 4 and discussions are made. Both electrical and spin transport measurements performed on microfabricated Cobalt/SiO_2 tunnel barrier/p-type silicon devices are discussed. The carrier densities, mobility, diffusion coefficients, etc. in differently doped silicon substrates are determined using Hall measurement technique. The Schottky barrier properties at the tunnel junction interface, as well as the change in the spin-signal with a magnetic field, temperature, and applied electrical bias voltage are discussed. Spin signal amplitude, spin resistance-area product, spin polarization, and spin lifetime are determined. Temperature and doping dependence measurements are discussed. The role of Schottky barrier on spin signal and anomalous spin reversal behavior are also discussed. Also, the spin transport behaviors for different Schottky barrier resistances are shown which can be either direct tunneling dominant or two-step tunneling dominant.

Chapter 2

Semiconductor spintronics

In this chapter, basic theory of semiconductor spintronics, electrical creation of spin accumulation and detection mechanism, manipulation of spin signal by Hanle effect and some spin relaxation mechanisms were discussed.

2.1 Spintronics

Spintronics is a multidisciplinary field which is governed by the active manipulation of spin degrees of freedom, i.e. spin angular momentum. This quantum property of electron, i.e. it can rotate either clockwise or anticlockwise around its own axis, can be treated as two states 0 and 1 for logical operations. Spin of single electron can be described by its magnetic moment $\mathbf{2}\boldsymbol{g}\boldsymbol{\mu}_{\boldsymbol{B}}\mathbf{s}$ ($\boldsymbol{\mu}_{\boldsymbol{B}}$ is the Bohr magneton and g is the electron's Landé **g**-factor, in a semiconductor, it is generally different from the free-electron's value of $\boldsymbol{g}_{\mathbf{0}} = 2.0023$). Spins in semiconductors are not pure spins because they consist of both spin and orbital angular momentums.

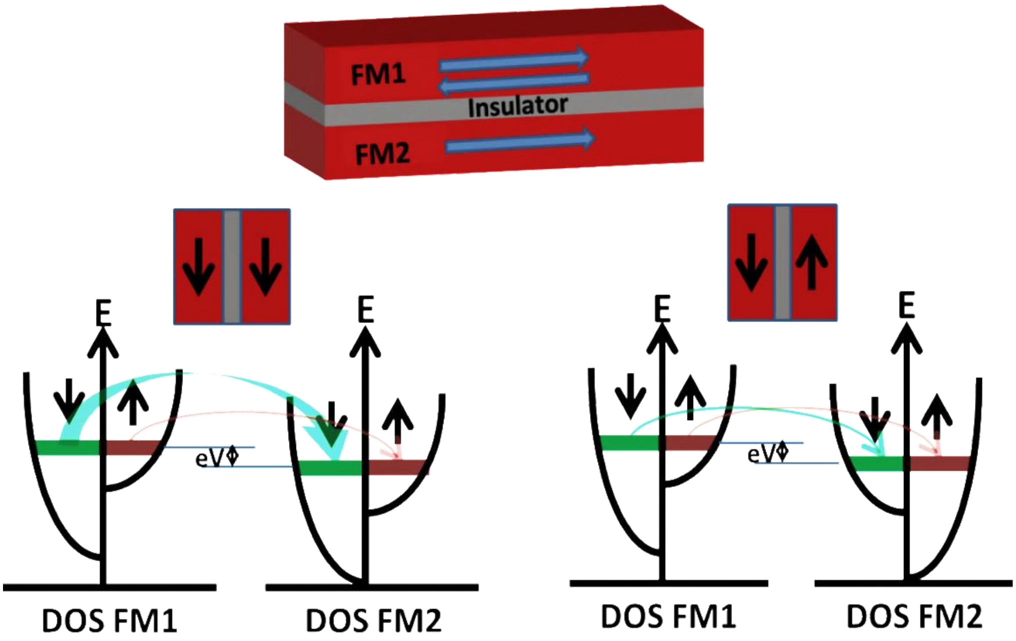

Figure 2.1. Description of Julliere's model of TMR in MTJ. Thin insulator between two ferromagnets provides spin dependent tunneling. When magnetization of both ferromagnets are parallel, majority spin of one ferromagnet find state in another ferromagnet, leads to low resistance. When antiparallel, unavailability of states leads to high resistance.

Tedrow and Messervey et al. performed the first experiments on spin-dependent electron transport phenomena using ferromagnet/insulator/superconductor (F/I/S) junction [11] and studied the magneto-resistance property. Then, magneto-resistance studied was extended to F/I/F, magnetic tunnel junction (MTJ), by Julliere which leads to the discovery of tunneling magneto-resistance (TMR) [12], shown in figure 2.1. The insulating layer is very thin (few nm) where electron can undergo quantum mechanical tunneling from one ferromagnet into the other. Based on this effect, Magnetic Random Access Memory (MRAM) has been realized.

With the discovery of giant magneto-resistance (GMR) in metallic layers by A. Fert and P. Grunberg in 1988, new avenue towards spintronics research field was triggered which has led to tremendous storage capacity of hard disks and magnetic random access memories (MRAM) today. Then, a canonical spin transistor proposed by Datta and Das [5] in 1990s has motivated many researchers about the concept of combining both memory and logic on the same device in order to solve the current issues of high power consumption & slow speeds, and remarkable improvements have been done so far.

2.1.1. Semiconductor Spintronics

To realize new novel devices by extending the application of spintronics to microelectronics, many researchers are interested in integrating magnetic devices in semiconductors by using the combination of ferromagnets and semiconductors. Carrier concentrations and transport characteristics in semiconductor can be controlled via doping and gate voltage. Ferromagnets provide the ability to store information at room temperature by switching their magnetization which can be done rapidly with unlimited endurance. In 1990s, spin injection in GaAs was demonstrated with spin diffusions length of many microns [13] [14] and spin lifetimes of > 100 ns [15]. In semiconductors, these parameters are many orders of magnitude larger than in metals because of which it has triggered high excitement for utilizing semiconductors as host for spin.

Conventional electronics is based on the number of charges & their energies, and device performance is limited in speed due to high power consumption, whereas spin electronics is based on the direction of spin & spin coupling, and is capable of much higher speeds at low power consumption. Spin manipulation of carriers is not strictly governed by physical limitations of scaling as for charge manipulation. It requires very less power to flip the spin in order to change the state in spintronic devices as compare to turn on and off the conventional transistor. This, in turn, means less heat is generated in such devices which is becoming a crucial factor in device design & scaling these days. Also, spintronic devices are more robust than charge based devices in high temperature, radiation environments as radiations or high temperature affects the charge stored in the memories but not the spin. As the magnetization or spin polarization does not change after device has been switched off, same spin based devices can integrate logic and memory devices in to the same chip easily. This one is the main target that we want to realize in future.

The most essential requirements for implementing a semiconductor-based spintronics technology are efficient spin injection mechanism, effective control & manipulation of spins inside semiconductor, and efficient spin detection mechanism. Basic structure of spin transistor is shown in figure 2.2, which requires all above mentioned criteria. One ferromagnet can be used as injector and another as detector. Gate can be used to manipulate the spin, either by electrically or by using small magnetic field, in order to take it to two states, fully relaxed state or accumulated state representing 0 and 1 state respectively.

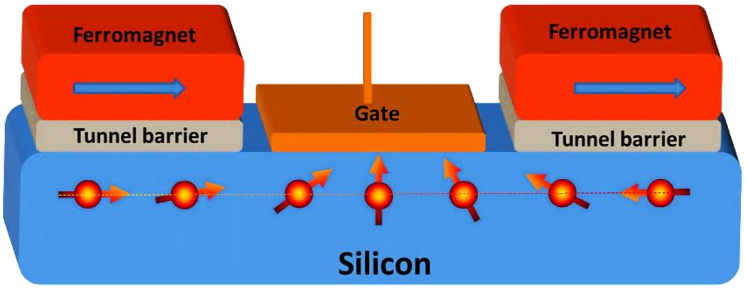

Figure 2.2. Spin transistor, one ferromagnet is used as injector and other as detector. Gate is used to manipulate the spin accumulation so that it can have two states, accumulated state and relaxed state.

2.2. Spin polarized current using ferromagnet

In ferromagnetic transition metals like Fe, Co, Ni, both the 4s and 3d electron bands contribute to the density of states at the Fermi level, E_F. As there is strong exchange interaction, it favors parallel orientation of electron spins so that the spin-up and spin-down 3d bands are shifted in energy. This exchange splitting creates the imbalance between numbers of up and down 3d electrons at the Fermi level that gives rise to the net magnetization in thermodynamic equilibrium. The spin polarization of electrons at the Fermi level is defined by following equation:

$$\boldsymbol{P} = \frac{\boldsymbol{N}\uparrow(\boldsymbol{E_F}) - \boldsymbol{N}\downarrow(\boldsymbol{E_F})}{\boldsymbol{N}\uparrow(\boldsymbol{E_F}) + \boldsymbol{N}\downarrow(\boldsymbol{E_F})} \tag{2. 1}$$

Where, $\boldsymbol{N} \uparrow (\boldsymbol{E_F})$ and $\boldsymbol{N} \downarrow (\boldsymbol{E_F})$ are the density of states (DOS) of spin-up and spin-down electrons at the Fermi level (E_F) respectively.

The conduction in ferromagnets is dominated by the un-split 4s band, the 4s electrons having a much higher mobility. 3d electrons are more localized and they are having larger effective mass, i.e. lower mobility, than 4s-electrons. However, the spin-conserving s-to-d transitions are the main source of s-electron scattering [16]. The spin-imbalanced density of states for 3d electrons at E_F results in strongly spin-dependent scattering probabilities (Fermi Golden Rule). Therefore, mobility for spin-up electrons is different than that of spin-down electrons and hence, the conductivity, which is proportional to mobility, is different. Fert and Campbell proposed ‘two-channel model’ due to different conductivities for spin-up and spin-down electrons [17]. In this model, spin-up and spin-down electrons are treated as independent entities without any spin-flip scattering events between them. Hence, the current flow in the ferromagnets through spin-up and spin-down channels is different and is given by,

$$\boldsymbol{j}_{\uparrow,\downarrow} = \frac{\boldsymbol{\sigma}_{\uparrow,\downarrow}}{\boldsymbol{e}} \frac{\partial \boldsymbol{\mu}_{\uparrow,\downarrow}}{\partial \boldsymbol{x}} \tag{2. 2}$$

Where, $j_{\uparrow,\downarrow}$ are the current densities due to flow of spin-up and spin-down electrons, $\mu_{\uparrow,\downarrow}$ are electro-chemical potential for spin-up and spin-down electrons and x is the spatial distance over which current flows.

Hence, when a current is passed through ferromagnets, it is polarized which is mainly due to different in mobility for spin-up and spin-down electrons. The bulk current polarization of a ferromagnetic metal can be defined as;

$$\boldsymbol{\alpha_F} = \frac{\boldsymbol{j}_\uparrow - \boldsymbol{j}_\downarrow}{\boldsymbol{j}_\uparrow + \boldsymbol{j}_\downarrow} \tag{2. 3}$$

With Andreev reflection measurement in quantum point contact, the value of bulk spin polarization was found to be 45% for Fe, 42% for Co and 27% for Ni at room temperature [18]. In our device fabrication Co was used as ferromagnet because of comparatively high magnetic anisotropy so that magnetization occurs along long axis direction easily. In our case, magnetization is along in plane direction. The orientation of the spin polarization is determined by the magnetization direction of the ferromagnet, which is in-plane, parallel to the interface.

2.3. Spin Injection in Semiconductors

When current is passed through the ferromagnetic metal (FM), it is spin polarized whereas in the non-magnetic material (NM), both spin-up and spin-down currents are in equilibrium. Spin injection is the process of injecting one type of spin in larger amount into the non-magnetic material in order to create the non-equilibrium spin populations, which can be achieved by applying potential differences across FM/NM interface. This causes diffusion of spin-polarized electrons from the FM into the NM and creates accumulation of majority spins inside the NM.

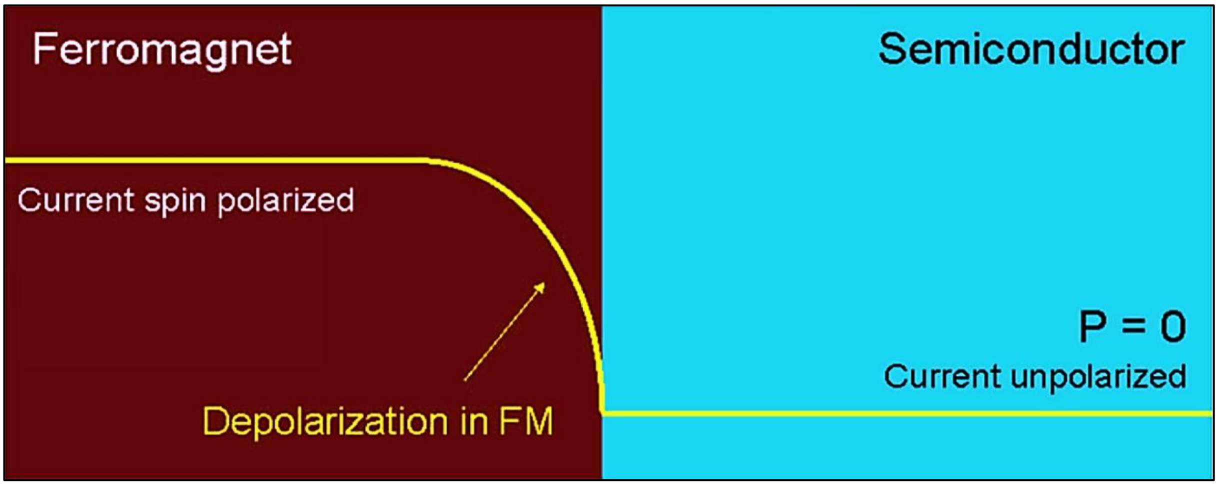

Figure 2.3. Current polarization at the FM/SC interface, for direct FM-SC contact, spin polarization is reduced rapidly at the interface from ferromagnet side due to high conductance mismatch that leads to the spin flipping [19].

However, in the case of semiconductors, direct FM contact, which is Ohmic, can’t be used as efficient spin injector. Repeated attempts were made on InAs semiconductor having 2DEG with Ohmic contacts using ferromagnetic electrodes like Co, Ni and NiFe in order to get spin injection. Non-local measurement was done however; no electrical current was detected in the second detecting ferromagnetic metal [20]. The injected spin polarized electrons could not be detected experimentally in a semiconductor (SC) with Ohmic contact in diffusive regime because there is a large difference in the band structure and the large conductivity mismatch between the FM, which is having very high conductivity, and the SC, which is having low conductivity. There is a spin-dependent resistance in the FM whereas the resistance for spin-up and spin-down electrons are the same in the case of SC. So, whatever we are measuring effectively is the voltage difference between up and down spin electrons in the FM which is negligible. A direct contact of a ferromagnetic metal on a silicon substrate in the diffusive transport regime gives a series circuit with a very small spin dependent FM resistance and a very large spin-independent SC resistance, resulting in almost zero spin asymmetry in the semiconductor. This additional resistance owing to the Schottky barrier creates a huge conductivity mismatch of many orders of magnitude between the FM tunnel contact and Si channel, resulting in a negligible spin polarization in Si. Hence, the conductivity mismatch problem was the main hurdles for creating spin accumulation inside semiconductors [21].

In the figure 2.3, variation of current polarization at the FM/SC interface can be seen where spin flips on the FM side are predominant. As the spin-electrons in FM approaches near the interface, spin flips occurs which leads to the progressive depolarization of the current.

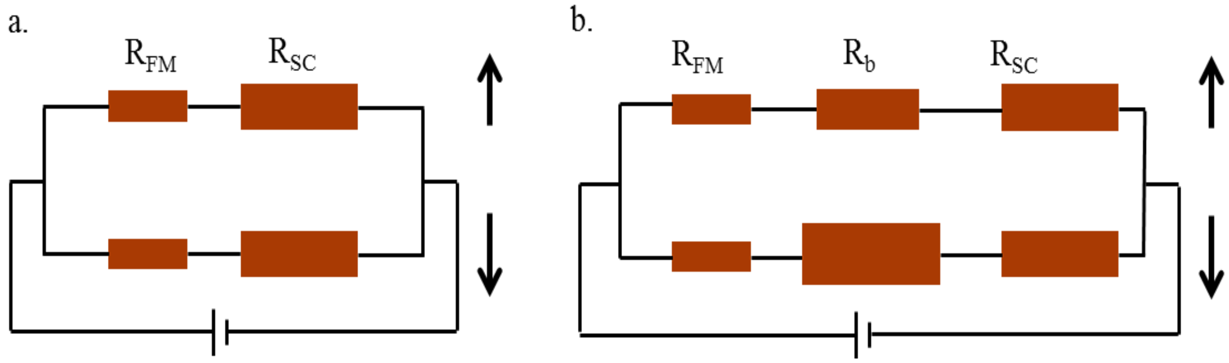

Figure 2. 4. a. Spin injection without tunnel barrier (diffusive regime) b. Spin injection with tunnel barrier (tunneling regime)

Rashba proposed that the conductivity mismatch problem can be solved, in order to have efficient spin injection from a ferromagnetic metal (FM) to a semiconductor (SC), by the insertion of a spin dependent resistance between the FM and the SC [22]. Inserting a very thin insulating layer as a tunnel barrier between FM and silicon layers improves the spin injection as tunnel barrier acts as a spin dependent resistance layer which enhances the spin polarization, under the assumption that spin does not flip during tunneling. By introducing this tunnel barrier, it will be energetically unfavorable for spins to flip back in FM leading to increase in spin accumulation in semiconductor. In this case, injection mechanism follows the quantum mechanical phenomena. The large spin-dependent resistance of the tunnel barrier leads to the measurable voltage difference across the device which is shown in figure 2.4. Inserting a tunnel barrier between FM and Si provides another benefit in that it avoids the formation of silicide at the FM/Si interface [23] which can reduce the spin injection. Various tunnel barriers have been researched upon for application like Al_2O_3, MgO, SiO_2. MgO has been found to give maximum efficiency in spin injection, partly, because of coherent injection owing to its crystalline form. But, for fabrication of such devices on silicon, SiO_2 is the preferred insulator because of its good interface properties with Si.

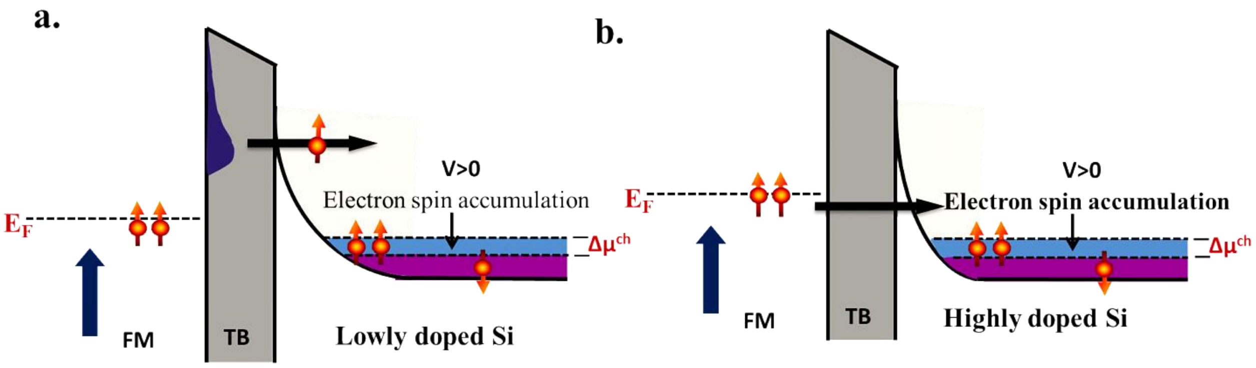

Figure 2.5. (a) Schematic energy band diagram of electrical spin injection in an FM/I/Si contact for lowly doped Si, thicker Schottky barrier. *V* is the bias voltage. The dashed lines show the Fermi energy. Here, electron with higher thermal energy are tunneling (b) Schematic energy band diagram depicting the electrical spin accumulation by splitting of energy bands by $\Delta\mu = \mu_{up} - \mu_{down}$ in an FM/I/Si contact for a highly doped Si, thinner Schottky barrier, with direct tunneling dominated [9].

One of the main challenges with FM/Si configuration is the formation of Schottky barrier which increases the effective tunnel barrier thickness and reducing the tunneling current as shown in the figure 2.5 (a). However, this problem can be overcome by reducing the Schottky barrier as it dominates in the total tunnel resistance. Various methods, possible to reduce the Schottky barrier, are in use. One method is to heavily dope the Si substrate. Although this one is not a complete solution, it effectively reduces the depletion layer width which eases the tunneling barrier as shown in figure 2.5 (b). Another more recent but much researched method of reducing the Schottky limitations is based upon the fact that Schottky barrier height depends on metal work function. Thus, by reducing the metal work function or by using a very thin layer of low work function, but still ferromagnetic metal, between the FM/SiO_2 interface, the Schottky barrier can be reduced considerably. Moreover, by varying the thickness of the low work-function material, desired Schottky barrier height can be obtained.

2.3.1. Spin injection in Si via tunneling

When a tunnel barrier is inserted between the FM and the SC, then electrons are injected from the FM into the SC via tunneling and the tunnel conductance is spin dependent. Majority spin electron (↑), whose magnetic moment are parallel to the magnetization direction of FM, have tunnel conductance, say $\mathbf{G}^{\uparrow}$, is different from that of minority spin electrons (↓), say $\mathbf{G}^{\downarrow}$, whose magnetic moment are antiparallel to the magnetization direction of FM. Therefore, one type of spin is injected at higher rate than the other type, resulting in the net spin accumulation in the SC and can be described by spin splitting $\boldsymbol{\Delta\mu=\mu^{\uparrow}-\mu^{\downarrow}}$ of the electrochemical potential, where $\boldsymbol{\Delta\mu}$ is the spin accumulation.

In the linear transport regime, the tunnel currents due to majority and minority spin electrons, denoted as $\mathbf{I}^{\uparrow}$ and $\mathbf{I}^{\downarrow}$ respectively, can be written as:

$$\boldsymbol{I^{\uparrow} = G^{\uparrow}\left(V - \frac{\Delta\mu}{2}\right)} \tag{2. 4}$$

$$\boldsymbol{I^{\downarrow} = G^{\downarrow}\left(V - \frac{\Delta\mu}{2}\right)} \tag{2. 5}$$

The voltage is defined as $\mathbf{V_{Si} - V_{FM}}$, where $\mathbf{V_{Si}}$ and $\mathbf{V_{FM}}$ are the spin-averaged potential of the silicon electrode and the ferromagnet, respectively. The total charge tunnel current $\mathbf{I = I^{\uparrow} + I^{\downarrow}}$ and the spin current $\mathbf{I_S = I^{\uparrow} + I^{\downarrow}}$ are written as:

$$\boldsymbol{I = GV - P_G G\left(\frac{\Delta\mu}{2}\right)} \tag{2. 6}$$

$$\boldsymbol{I_S = P_G GV - G\left(\frac{\Delta\mu}{2}\right)} \tag{2. 7}$$

Where, $\mathbf{G = G^{\uparrow} + G^{\downarrow}}$ is the total conductance and $\mathbf{P_G = (G^{\uparrow} - G^{\downarrow}) / (G^{\uparrow} + G^{\downarrow})}$ is the tunnel spin polarization (TSP). Note that TSP is different than the polarization of the tunnel current ($\mathbf{I_S/I}$) owing to the presence of a non-zero $\boldsymbol{\Delta\mu}$.

Steady-state condition of the spin accumulation in the non-magnetic material is obtained when the spin current, $\mathbf{I_S}$, injected by tunneling is balanced by the spin current due to relaxation of spin in the material, which can be expressed in terms of material parameters.

$$\boldsymbol{\Delta\mu = 2\, I_S\, r_S} \tag{2. 8}$$

Where, $\mathbf{r_S}$ describes the spin accumulation, $\Delta\boldsymbol{\mu}$ that occurs right at the interface, in terms of the spin current, $\mathbf{I_S}$ injected by tunneling. Spin accumulation decays exponentially with distance from the injection interface with the spin diffusion length $\mathbf{L_{sd}}$.

The solutions for the spin accumulation and spin current are:

$$\Delta\boldsymbol{\mu} = \frac{\boldsymbol{2r_sR_{tun}}}{\boldsymbol{R_{tun}+(1-P_G^2)P_G}}\boldsymbol{P_GI} \tag{2. 9}$$

$$\boldsymbol{I_S} = \frac{\boldsymbol{R_{tun}}}{\boldsymbol{R_{tun}+(1-P_G^2)P_G}}\boldsymbol{P_GI} \tag{2. 10}$$

Where, $\boldsymbol{R_{tun}}$ is **1/G**. Two regimes:

1. When $\boldsymbol{R_{tun}} > \boldsymbol{r_s}$, $\Delta\boldsymbol{\mu}$ remains small and has negligible effect on spin/charge current.
2. When $\boldsymbol{R_{tun}} < \boldsymbol{r_s}$, the spin current is reduced by the built-up of large spin accumulation.

When we have real spin dependent tunnel resistance such that $\boldsymbol{R_{tun}} = \boldsymbol{(1-P_G^2)r_B^*}$, where $\boldsymbol{r_B^*}$ is the effective tunnel resistance, the expressions for $\Delta\boldsymbol{\mu}$ and $\boldsymbol{I_S}$ simplifies as:

$$\Delta\boldsymbol{\mu} = \frac{\boldsymbol{2r_sr_B^*}}{\boldsymbol{r_B^*+P_G}}\boldsymbol{P_GI} \tag{2. 11}$$

$$\boldsymbol{I_S} = \frac{\boldsymbol{r_B^*}}{\boldsymbol{r_B^*+P_G}}\boldsymbol{P_GI} \tag{2. 12}$$

2.3.2 Effect of Schottky barrier and contact resistance – Doping dependence

Min et al. studied about the factors affecting the contact resistance on Si by changing the doping concentration from low to moderate value and found that the contact resistance is not determined by the tunnel oxide, but the Schottky barrier which is making it larger by the orders of magnitude [24] [25]. At low doping concentrations, depletion region is very wide which causes large contact resistance which introduces the complications for spin transport by changing the transport process to thermionic emission.

By having a structures with a semiconductor channel between two ferromagnetic contacts, Jaffres and Fert found that certain value of the contact resistance in a relatively narrow window is essential to have a large magneto-resistance (MR) value [26] [27] [28]. If contact resistance is too small, then the effect of the impedance mismatch is pronounced and the spins cannot be injected into the semiconductor. If the contact resistance is too large, then the average time an electron resides in the channel becomes longer than the spin-relaxation time which vanishes the spin accumulation in the channel.

The relation between the MR and the contact resistance of a two terminal FM/I/Si/I/FM spin-MOSFET is shown in figure 2.6 (a) and (b) for spin lifetime of 1 ns and 100 ps respectively. For large value of $\boldsymbol{\tau}_s$ (1 ns), there is a wide window of the contact resistance for a significant MR and maximum MR of about 90% is obtained (considering state of the art MgO based ferromagnetic tunnel contacts with TSP of 70% at room temperature [29]). When $\boldsymbol{\tau}_s$ is smaller, the window of contact resistance for a significant MR also becomes narrow. The reason behind this is due to shift of the high resistance cut-off which is determined by the ratio of the dwell time and $\boldsymbol{\tau}_s$.

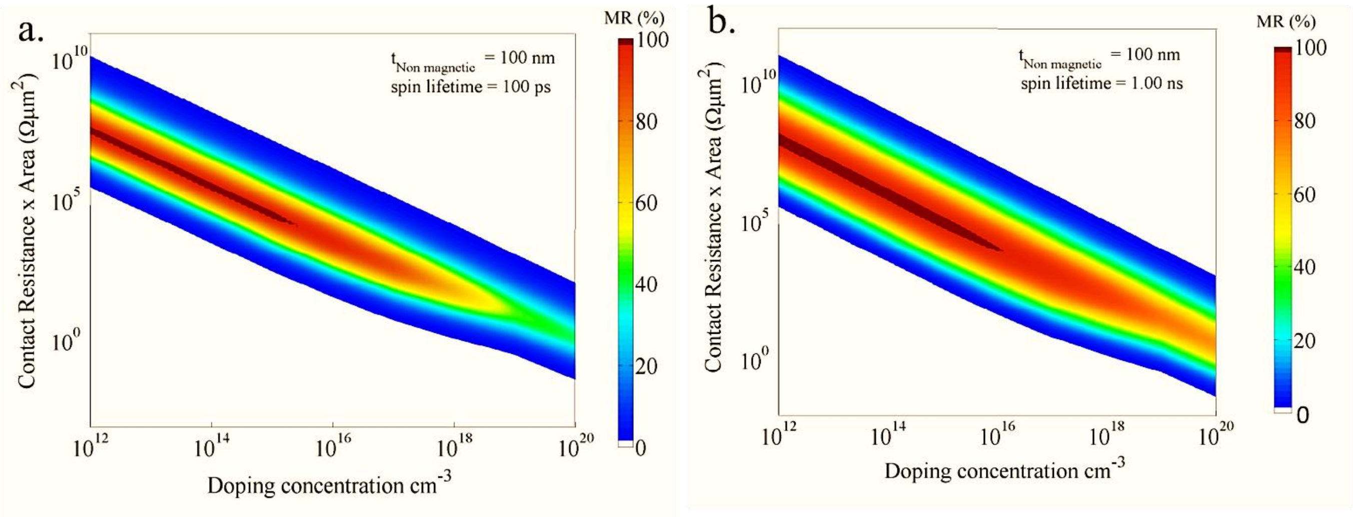

Figure 2.6. Effect of contact resistance for spin-tunnel devices: Computed normalized magneto-resistance of a two-terminal FM/I/Si/I/FM spin-MOSFET against the contact resistance of the tunnel interface at 300K for spin lifetime of a. 100 ps b. 1 ns

Also, for three different values of Si channel thickness (10 nm, 100 nm and 1000 nm) between two FMs for above mentioned spin-MOSFET devices, MR is plotted against contact resistance with spin lifetime of 1 ns, shown in figure 2.7, and widest contact resistance window was found for smallest thickness of Si channel with largest MR.

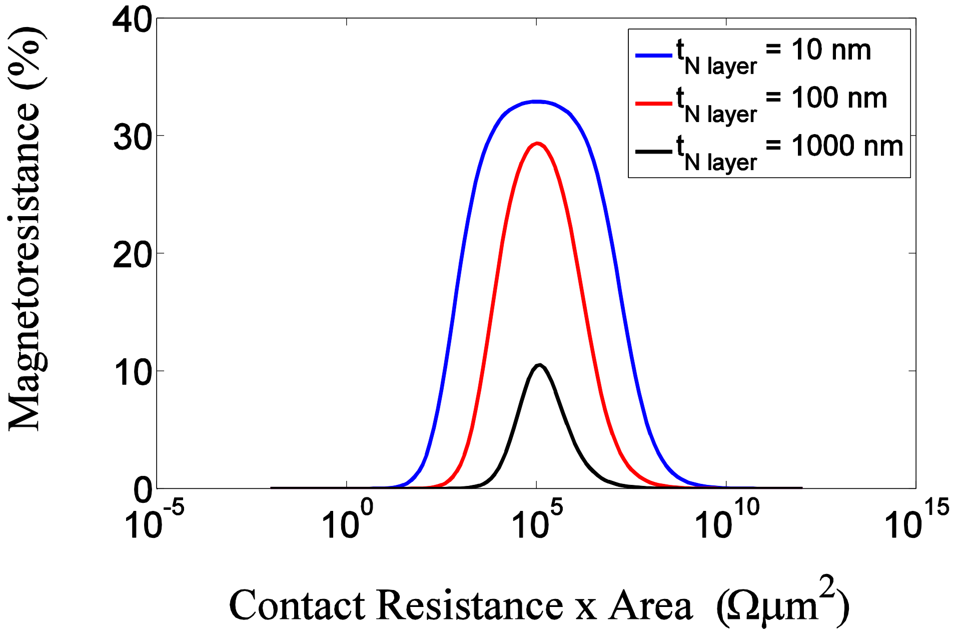

Figure 2.7. MR Vs. contact resistance for different value of Si channel thickness between two FMs in spin-MOSFET. For smaller thickness, there is larger MR and also wider contact resistance window. Spin lifetime was assumed to be 1 ns.

2.4. Manipulation of Spin Accumulation

Controlling the spin polarization direction or population is crucial to the application of spintronics in order to realize it as switching devices. Similar to its charge analog, where the amount of charge or width of channel is controlled by an externally applied field for switching, in spintronics too, a control knob is required for operation and efficient detection of spin in the device. This control can be done by applying an electric field utilizing Rashba effect as proposed by Datta and Das in 1990 [5]. When an electric field transverse to the carrier's direction of motion is applied, it transforms into magnetic field due to strong spin-orbit coupling which acts on the spin [5] [30]. Spin precession is momentum dependent and hence requires the motion of carriers. However, relatively large distance is required to use this method of spin control and also, materials with high spin-orbit coupling is essential. Thus, this method is not suitable for Si, having weak spin-orbit coupling and also, with present sub-100 nm scaling. Another, practical approach is to manipulate by applying small magnetic field.

2.4.1 Manipulation of spins by external magnetic field

In this thesis work, external magnetic field was used to control the spin polarization with the help of Hanle effect, shown in figure 2.6. When magnetic field B is applied perpendicular to the axis of spin orientation (transverse magnetic field), it will induce spin precession with the Larmor frequency $\boldsymbol{\omega_L = \mu_B g B/h}$, where $\boldsymbol{\mu_B}$ is the Bohr magneton and **g** is the electron g factor (assuming 2, in case of silicon). The spin precession, together with the random character of carrier generation or diffusion, leads to the spin dephasing. Consequently, precession makes electron spin acquire random phases relative to those which were excited or have arrived at different times. As a result, the projection of the electron spin along the magnetization direction of ferromagnet will decrease with the increase of transverse magnetic field, leading to depolarization of the SC. This is known as the Hanle effect.

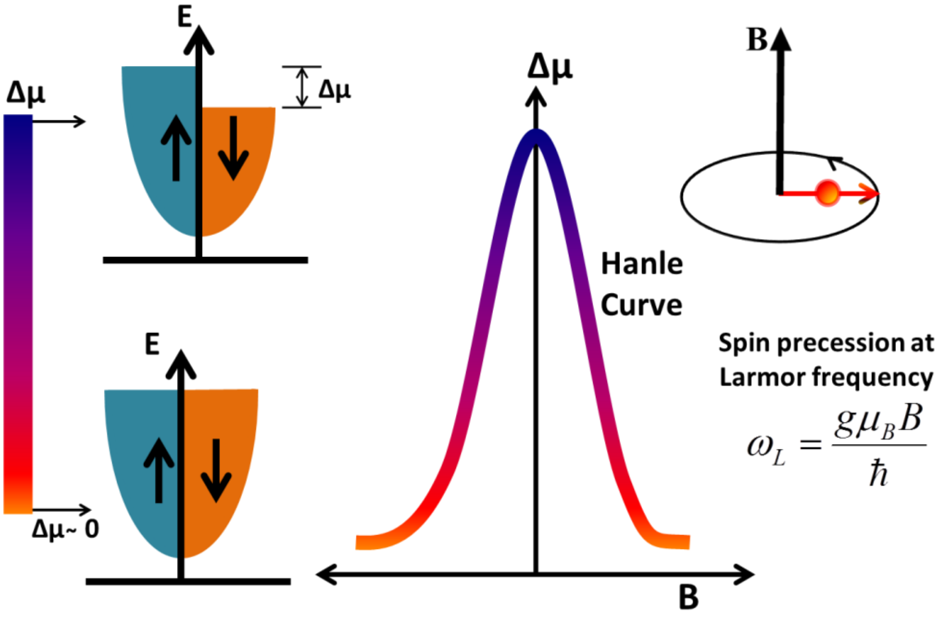
Δμ
E
Δμ
Δμ~ 0
E
Δμ
Hanle Curve
B
B
Spin precession at Larmor frequency
$\omega_L = \frac{g\mu_B B}{\hbar}$

Figure 2.8. A characteristic Hanle curve with highest spin accumulation at B=0 and Lorentzian decrease in accumulation of spin signal as the perpendicular magnetic field is increased. At higher magnetic field, it is reaching equilibrium condition with no polarization.

The spin accumulation decays as a function of magnetic field, B with an approximately Lorentzian line shape given by $\boldsymbol{\Delta\mu(B)=\Delta\mu(0)/(1+(\omega_L\tau)^2)}$, where $\boldsymbol{\tau}$ is the spin lifetime, $\boldsymbol{\Delta\mu(B)}$ is the spin accumulation in the presence of a perpendicular B-field, and $\boldsymbol{\Delta\mu(0)}$ is the spin accumulation in zero applied field. At small B, the Larmor frequency, $\boldsymbol{\omega_L}$ is much smaller than **$1/\tau$** and the spins precess only over a small angle during the time τ. In this case, precession has little influence on the spin accumulation. For large B-field, the Larmor frequency becomes much larger than **$1/\tau$** and spins make several complete cycles of coherent precession during the time **τ** which causes the time average of the spin accumulation to gradually reduce to zero with increasing B. The spin accumulation is reduced to half of its initial value when **$\omega_L = 1/\tau$.** The half width at half maximum of the Lorentzian Hanle curve, thus, allows extraction of the spin lifetime **τ**. Moreover, by varying the perpendicular magnetic field, spin accumulation inside silicon can be controlled. Typical spin accumulation with varying magnetic field is represented in characteristic Hanle curve, shown in figure 2.8. The maximum and minimum values of **$\Delta\mu$** can be obtained for **$\omega_L = 0$** and **$\omega_L \tau >> 1$** respectively.

In practice, shape of Hanle signal can be deviated from a Lorentzian line shape. Firstly, if the semiconductor is thicker compared to **L_{sd}**, spin diffusion length, then there is modification of Hanle curve by the spin diffusion perpendicular to the tunnel interface and the extracted spin lifetime [31] can increase by about 50% compared to that obtained from a Lorentzian fit. Secondly, when $\boldsymbol{R_{tun} < r_s}$, the magnitude of spin accumulation, $\Delta\boldsymbol{\mu}$ is reduced by the coupling of the spins to the ferromagnet and there is modification of the functional dependence of $\Delta\boldsymbol{\mu}$ on **B**. Finally, the roughness of the ferromagnetic tunnel interface can give rise to local magneto-static fringe fields [32] which can cause artificial broadening of the Hanle curve without the change of **τ**. Hence, the extracted spin lifetime from Hanle curve is considered as the lower bound of it.

2.4.2 Theoretical description of Hanle effect

When we apply an external magnetic field $\vec{\boldsymbol{B}}$, the electron spins, or say spin magnetization $\vec{m}$, experiences a torque, $\vec{\mathrm{r}}$ which is given by:

$$\vec{\mathrm{r}} = \overrightarrow{\boldsymbol{m}} \times \overrightarrow{\boldsymbol{B}} \qquad \textbf{(2. 13)}$$

This torque causes precession of spins around the axis of external magnetic field at a Larmour frequency given by:

$$\boldsymbol{\omega_L} = \left|\frac{\boldsymbol{ge}}{\boldsymbol{2m}}\boldsymbol{B}\right| \qquad \textbf{(2. 14)}$$

There is also a damping of the precessional motion which is caused by spin relaxation and the creation or recombination of electrons. Combing this spin precession with spin creation, spin relaxation and recombination, the simple equation of motion of averaged spin vector, $\vec{S}$ can be written as:

$$\frac{d\vec{S}}{dt} = \frac{\vec{S}_o - \vec{S}}{\tau} - \frac{\vec{S}}{\tau_s} + \omega_L \times \vec{S} \qquad (2.15)$$

Where, $(\vec{S}_o/\tau)$ and $(\vec{S}/\tau)$ in the first term denote spin generation and recombination with electron lifetime τ respectively, 2nd term describes the spin relaxation with spin relaxation time τ_s and third term describes the spin precession in magnetic field with frequency ω_L. Then spin lifetime, τ_{sf} can be derived using τ and τ_s which is given by:

$$\frac{1}{\tau_{sf}} = \frac{1}{\tau} + \frac{1}{\tau_s} \qquad (2.16)$$

Taking stationary state condition (dS/dt=0) and assuming that, there is no external magnetic field, we obtain:

$$S_z(0) = \frac{S_o}{1+\tau/\tau_s} \qquad (2.17)$$

Where, $S_z(0)$ is the projection of the spin on the direction of S_o (z-axis). In the presence of perpendicular magnetic field along z-axis, we get:

$$S_z(B) = \frac{S_z(0)}{1+(\omega_L \tau_{sf})^2} \qquad (2.18)$$

Thus, the projection of the electron spin along the magnetization direction of ferromagnet will decrease with the increase of transverse magnetic field that causes increase in spin precession frequency, leading to depolarization of the semiconductor. This is known as the Hanle effect. In general, spin transport in a non-magnetic channel can be confirmed by observing this effect.

Dash et al. [9] observed Hanle signal for n-type Si at room temperature for the first time, which is shown in figure 2.9. Due to injection of large number of majority spin into conduction band of n-type Si, it causes spin splitting of electrochemical potential and that accumulation decreases with increase in magnetic field in a lorentzian fashion due to spin precession.

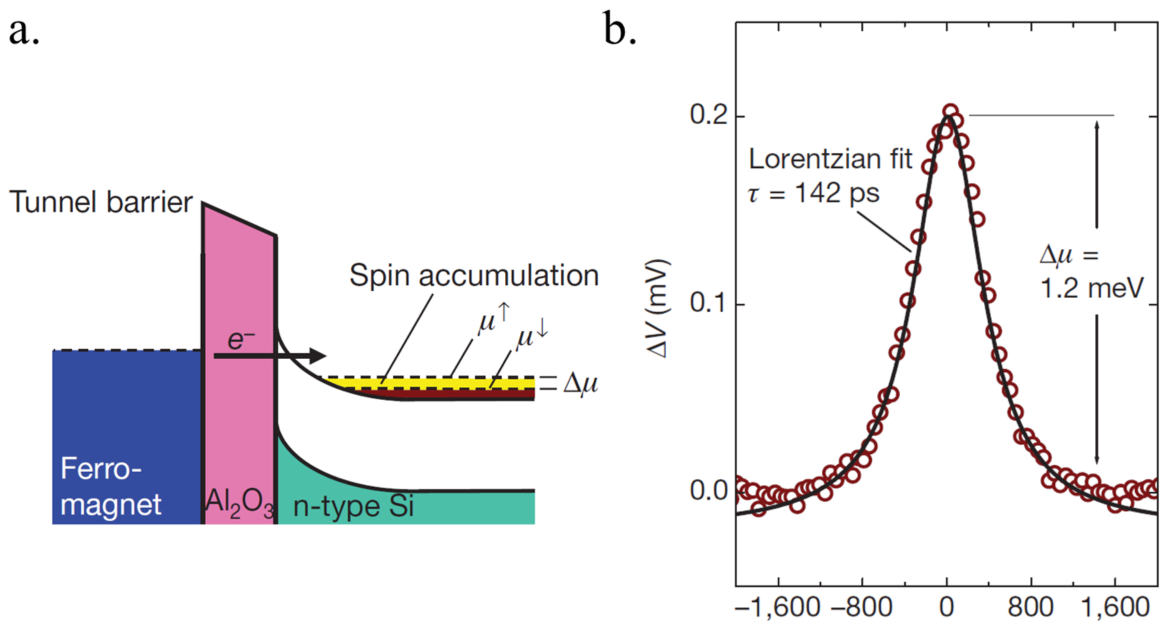

Figure 2.9. a. Energy band diagram showing electron spin injection into conduction band, accumulation of majority spin causes spin splitting of electrochemical potential; b. Hanle effect observed at room temperature for n type Si with Al_2O_3 tunnel barrier, spin accumulation decreasing with increase in magnetic field that causes spin precession [9].

2.4.3 Inverted Hanle effect

When an external magnetic field is applied parallel to the magnetization of the ferromagnet, then it enhances the spin accumulation inside semiconductor and the inverted Lorentzian curve is obtained, which is called inverted Hanle effect. Due to the finite roughness at the ferromagnetic interfaces, it produces the magneto-static fringe field which is local and spatially inhomogeneous [32]. Hence, spin precession occurs with these local magneto-static fields, shown in figure 2.9 (a), which causes the reduction of spin accumulation from its maximum value even at zero external transverse magnetic field. This effect can be clearly seen in inverted Hanle effect which depicts the recovered amount of spin accumulation.

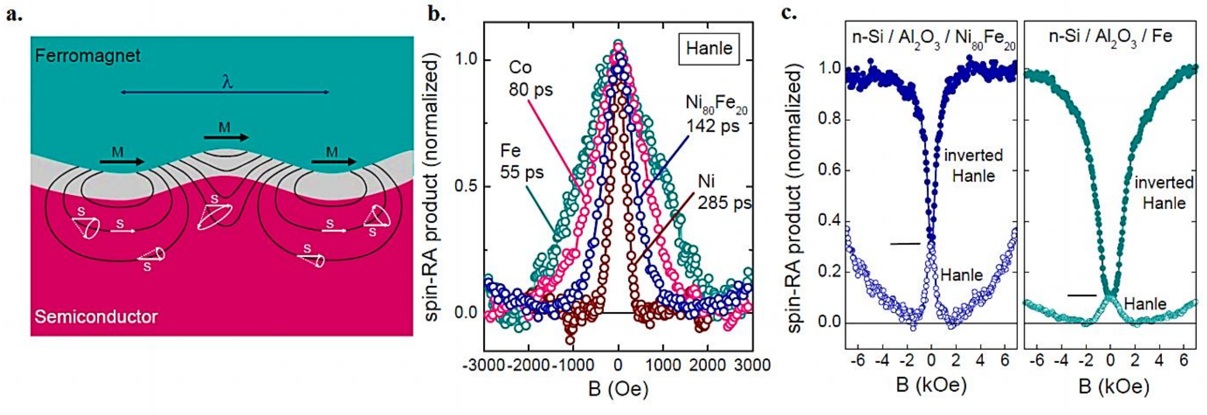

Figure 2.10. Precession of spin in semiconductor near a ferromagnetic tunnel interface: (a) Illustration of inhomogeneous local magnetostatic fields arising from the roughness. (b) Hanle curves of Si/Al_2O_3/ferromagnet devices with different ferromagnetic electrodes. (c) Hanle and Inverted Hanle effect [32]

From figure 2.10 (c), we can say that true value of spin accumulation inside semiconductor is the sum of Hanle and inverted Hanle amplitudes. Also, the Hanle signal broadened due to the local fringe fields, which scales with the roughness amplitude and with the magnetization of the ferromagnetic electrode. Dash et al. observed that the width of the Hanle curve depends on the ferromagnetic electrode [32] which is shown in figure 2.10 (b). Broadening of Hanle curve increases with the increase in the magnetization which follows the order, Ni < $Ni_{80}Fe_{20}$ < Co < Fe and it provides an important implication for the extraction of the spin life time, which no longer determined the width of Hanle curve. So, the real spin life time is larger than that extracted from the Hanle curve.

2.5. Spin Detection

Spin detection typically relies on sensing the changes in the signals caused by the presence of non-equilibrium spin in the system. The common goal in many spintronic devices is to maximize the spin detection sensitivity to the point that it detects not only the spin signal itself, but also the changes in the spin states. By keeping the rate of spin accumulation constant, control knob on spin direction of polarized electrons is varied & resulting change in output signal, because of change in spin accumulation at the detector, is observed. A change in spin accumulation **$\Delta\mu$,** with B-field translates into a measurable voltage change across the tunnel contact, because the tunnel conductance between the Si and the ferromagnetic electrode is proportional to the projection of the electron spin polarization in the Si on the fixed measurement axis given by the magnetization direction of the ferromagnetic electrode. The resulting voltage change is given by **ΔV=TSP × Δμ/2**, where TSP is the (known) tunnel spin polarization of the FM–insulator interface. Thus, by keeping the current in to the device constant, the perpendicular magnetic field is varied & corresponding voltage change across the device is measured.

The amount of spin accumulation can be detected electrically with a ferromagnetic tunnel contact and is described by the relation:

$$\boldsymbol{V = R_{tun} I + \left(\frac{P_G}{2}\right)\Delta\mu} \tag{2. 19}$$

In a non-local (NL), four terminal device, the charge current in the detector contact is zero and the detected voltage is solely due to spin accumulation, given by $\boldsymbol{\Delta V = \left(\frac{P_G}{2}\right)\Delta\mu}$. However, in practice, NL measurements always have a finite background voltage. Artifacts that can affect the spin accumulation can be local Hall effect, magneto-resistance effect, etc.

In a three-terminal (3T) device, it uses single ferromagnetic contact, which is used for both injection and detection, so that detection method is quite different from NL device. In 3T device, spin accumulation is probed right under the ferromagnetic injector contact, which is measured with higher signal as compared to NL device, where spin accumulation is probed in the tail region with exponential decay of spin accumulation with distance from the injector. With control manipulation via Hanle effect, resulting change in voltage across the contact can be measured at constant current.

2.6. Spin relaxation and dephasing in semiconductors

Spin relaxation in semiconductor is the process of bringing the accumulated spin population back to the equilibrium and it determines the rate of spin accumulation inside semiconductor and also, spin life time, τ. Several mechanisms are causing spin relaxations, mostly occur due to spin-orbit interaction in combination with momentum scattering or due to spin precessions around random fluctuating magnetic fields or due to emission/absorption of magnons, etc.

2.6.1. Spin Orbit Coupling

When a particle is moving with velocity $\vec{v}$ in an electric field $\boldsymbol{\vec{E}}$, it will experience a magnetic field given by $\boldsymbol{\vec{B} = (1/c^2)\vec{E} \times \vec{v}}$**,** where c is the velocity of light. Similarly, when electron is in rest condition, magnetic field that arises from the electric field due to nuclear charge (+Ze) acts upon the electron magnetic moment. The electric field is radial which is given by,

$$\vec{\boldsymbol{E}} = \frac{\mathbf{1}}{\boldsymbol{e}} \frac{\boldsymbol{\partial U(r)}}{\boldsymbol{\partial r}} \overrightarrow{\boldsymbol{u_r}} \tag{2. 20}$$

Where, U(r) is electric potential of the electron and the angular momentum $\vec{\boldsymbol{L}}$, can be written as $\vec{\boldsymbol{L}} = \overrightarrow{\boldsymbol{u_r}} \times \boldsymbol{m}\vec{\boldsymbol{v}}$. This results in the effective magnetic field given as:

$$\vec{\boldsymbol{B}}\boldsymbol{eff} = \frac{\mathbf{1}}{\boldsymbol{m_e ec^2}} \frac{\mathbf{1}}{\boldsymbol{r}} \frac{\boldsymbol{\partial U(r)}}{\boldsymbol{\partial r}} \vec{\boldsymbol{L}} \tag{2. 21}$$

which is perpendicular to both $\vec{E}$ and $\vec{v}$ and parallel to the orbital angular momentum L. This gives rise to the spin-orbit interaction which is relativistic and obeys quantum mechanical principle.

Electron with spin $\vec{S}$ has magnetic moment $\overrightarrow{\boldsymbol{\mu}} = -\frac{\boldsymbol{g\mu_B}}{\hbar}\overrightarrow{\boldsymbol{S}}$ **,** where g is the Lande factor and μ_B is Bohr magneton, and it has Zeeman energy, $\overrightarrow{\boldsymbol{H}} = -\vec{\boldsymbol{\mu}}.\overrightarrow{\boldsymbol{B}}$ in the presence of magnetic field. Hence, the energy associated with spin-orbit coupling due to the above magnetic field is

$$\boldsymbol{H} = \frac{\boldsymbol{\mu_B}}{\hbar \boldsymbol{m_e ec^2}} \frac{\mathbf{1}}{\boldsymbol{r}} \frac{\boldsymbol{\partial U(r)}}{\boldsymbol{\partial r}} \vec{\boldsymbol{L}}.\overrightarrow{\boldsymbol{S}} \tag{2. 22}$$

This spin-orbit interaction is also responsible for band-split off in valence band.

2.6.2 Main spin relaxation mechanisms

1. The Elliott-Yafet (EY) mechanism

Due to presence of specific defects within semiconductor, scattering of electrons occurs that causes the spin of electron to flip. These defects can be structural defects (misfit dislocations, grain boundaries or local impurities) or dynamical defects (lattice vibrations). Charged impurities or lattice vibrations possess some electric fields that can induce magnetic fields through spin-orbit coupling and mixes the spin up and spin down states [33] [34]. However, this spin-orbit coupling should be present along with momentum scattering to cause spin relaxation.

In terms of temperature dependence, spin relaxation is dominant due to impurities scattering at lower temperatures and phonon scattering at higher temperatures. This Elliott-Yafet spin relaxation mechanism is proportional to momentum scattering rate and dominant for inversion-symmetric materials like Si and Ge.

2. **The D’yakonov-perel’ mechanism**

In semiconductor crystals lacking inversion symmetry, there is presence of a finite electric field due to which electrons feel a momentum dependent effective magnetic field. This effective magnetic field leads to the spin precession. This type of spin relaxation mechanism is dominant in crystals of groups III-V (e.g. GaAs) and II-VI (e.g. ZnSe) semiconductors, where the presence of two distinct atoms in the Bravais lattice breaks the inversion symmetry. In this mechanism, the spin relaxation rate is inversely proportional to momentum scattering rate, which is in contrast to the Elliot-Yafet mechanism. The spin changes the direction by rotating between the collisions but not during collisions. Hence, this relaxation rate increases with the decrease in the impurity concentration and is dominant at higher temperatures (>70 K). For semiconductors possessing crystal inversion symmetry like Si and Ge, this D’yakonov-Perel’ mechanism is not significant so that spin lifetime in these semiconductors can be higher than that in III-V semiconductors by orders of magnitude [35].

3. **The Bir-Aronov-Pikus mechanism**

Due to exchange interaction between the electron and hole spins, the non-equilibrium electrons in p-type semiconductor undergo spin relaxation. It is significant in semiconductors with a high overlap between the electron and the hole wave functions like in heavily p-doped semiconductor. There is an effective magnetic field due to exchange interaction which causes the electron spins to precess, leading to the inhomogeneous dephasing. This spin relaxation mechanism is proportional to the hole concentration and is important at low temperatures [36].

4. **Hyperfine-interaction mechanism**

The hyperfine interaction arises from the magnetic interaction between the magnetic moments of electrons and nuclei, provides an important mechanism for ensemble spin dephasing and single-spin decoherence of localized electrons. As, this spin relaxation mechanism is mostly significant for electrons in localized states such as those confined in quantum dots or bound on donors, it is too weak to cause effective spin relaxation of free electrons in metals or in bulk semiconductors.

2.7 Schottky barrier

When a metal and a semiconductor are brought in contact, an electrostatic potential barrier is created at the interface of these two materials, which is called as Schottky barrier. The Schottky barrier is formed when there is equilibrium between the Fermi levels of metal and semiconductor. As Schottky barrier resistance is also a part of the junction resistance and the width of Schottky barrier, which changes with doping, is also one determining factor for the spin current transport through the ferromagnetic tunnel junction. Large Schottky barrier width leads to diode like behavior whereas small Schottky barrier width leads to tunnel device like behavior. We require tunneling current in order to have large spin accumulation.

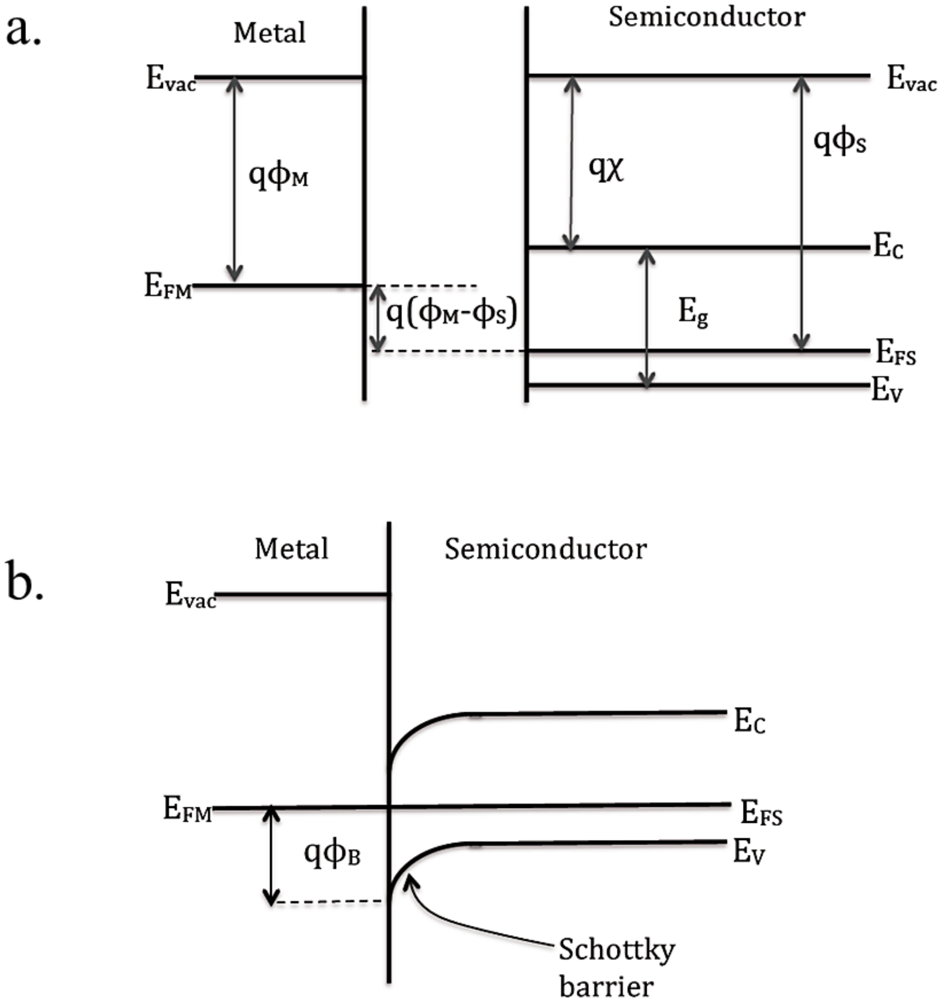
a.
Metal
Semiconductor
Evac
qφM
EFM
q(φM-φS)
qχ
qφS
Evac
Ec
Eg
EFS
Ev
b.
Metal
Semiconductor
Evac
Ec
EFM
EFS
qφB
Ev
Schottky barrier

Figure 2.11. Band diagram of metal and semiconductor a. before contact b. after close contact with each other. Valence band and conduction band will be at the same distance from the Fermi level and also due to high density of states in metal, Fermi level remains constant. So, there is band bending when Fermi level aligned at the same level after reaching equilibrium condition.

When semiconductor and metal are in close contact with each other, electrons will start to flow from material with high Fermi energy (metal) to that with low Fermi energy (p-type Si) until equilibrium state is reached. This equilibrium state is characterized by same Fermi level throughout the structure. This will cause band bending at the interface leading to the formation of Schottky barrier. As, electrons enters into p-type Si, negative charges, due to ionized acceptor atoms, is created inside p-type Si forming depletion region.

Consider the energy bands in a p-type semiconductor (here, we deal with only p-type Si) and a metal as shown in figure 2.11. E_{FM} and E_{FS} are the Fermi levels of metal and Si respectively. $q\phi_M$ is the work function of metal , χ and E_g are the electron affinity and band gap of Si. E_C and E_V are the energy level for conduction band and valence band respectively for p-type Si. So, Schottky barrier height becomes,

$$\emptyset_B = \frac{E_{FM}-E_V}{q} = \frac{E_g+q.\chi-q.\emptyset_M}{q} = \chi - \emptyset_M + \frac{E_g}{q} \tag{2.23}$$

where, band gap is given by $E_g= E_C-E_V$.

Schottky barrier width can be calculated as,

$$W = \sqrt{\frac{2\epsilon_s(V_I-V_a)}{q.n_p}} \tag{2.24}$$

$$W = \sqrt{\frac{2\epsilon_s\left(\varphi_B+\frac{kT.ln\left(\frac{n_p}{n_i}\right)}{q}-V_a\right)}{q.n_p}} \tag{2.25}$$

where, $V_I = \varphi_B + \frac{kT.ln\left(\frac{n_p}{n_i}\right)}{q}$ is built in potential, ϵ_S is the dielectric constant of the SC and n_p is the constant charge carrier density in the depletion region, q is charge, φ_B is the Schottky barrier height, $n_i = \sqrt{N_C N_V} e^{-E_g/2kT}$ is the intrinsic charge carrier density and V_a is applied voltage [37] .

Chapter 3

Device Fabrication

In this chapter, fabrication methods are discussed in details. All the fabrication processes were done in the Nanofabrication laboratory at MC2-Chalmers. Devices with ferromagnetic tunnel contacts over silicon chips were fabricated.

3.1 Fabrication

3.1. 1. Wafer Cleaning

Wafer cleaning is obligatory before any fabrication process in order to make sure that there are no undesirable organic and inorganic particles on the substrate. The reasons behind this are described below:

a. Presence of unwanted layers or particles on the surface affects device fabrication process as it degrades the adhesion properties of the photoresist. Moreover, presence of unwanted particles gives roughness to the surface which causes the non-uniform deposition of thin films over them with certain defects.
b. Another serious consequence due to the presence of impurities during fabrication is on the device characteristics because of the formation of trap centers (oxide traps, interface traps, etc.) or impurity levels inside the bulk of the substrate.

The source of such impurities or unwanted layers can be either human handling or during the process of the machines inside the clean room. Human operators can generate dust particles, dandruff, bacteria, etc. and previous photo-lithography steps can leave impurities such as solvent, water (moisture), and photoresist residues. In addition, oil (vacuum pumps), silicone (vacuum grease) or abrasive particles from Clean-room equipment can also be the reason of unwanted particles. Wafer cleaning involves the following:

- Removal of the organic contaminants (Organic Clean)
- Removal of thin oxide layer formed as a result of step 1 (Oxide Strip)
- Removal of ionic contamination (Ionic Clean)

The wafers are prepared by soaking them in ultrasonic Acetone and IPA (Iso-Propyl Alcohol) cleaning and subsequently rinsing in DI water. The first step called SC-1, where SC stands for Standard Clean, is performed with a 1:1:5 solution of NH_4OH (ammonium hydroxide), H_2O_2 (hydrogen peroxide) and H_2O (DI water) at 75 °C or 80 °C typically for 10 minutes. This treatment oxidizes the organic elements present in to CO_2 & H_2O and results in the formation of a thin SiO_2 layer (about 10 A°) on the silicon surface, along with a certain degree of metallic contamination (notably Iron) that shall be removed in subsequent steps. This is followed by immersing the wafers into a DI water bath. The second step is a short immersion in a 1:50 solution of HF + H_2O at 25 °C, in order to remove the thin oxide layer and some fraction of ionic contaminants. The third and last step (called SC-2) is performed with a 1:1:5 solutions of HCl, H_2O_2 and H_2O at 75 °C or 80 °C which efficiently removes the remaining traces of metallic (ionic) contaminants.

In addition to standard cleaning, which must be done before starting with the clean room fabrication on a wafer, cleaning must be done before each lithography steps to make sure that there are no residues left of previous processing step. This is done by ultrasonically soaking them in acetone and IPA for 5 minutes each, followed by rinsing in DI water. It should be followed by 30 seconds immersion in HF (2%) to etch out any SiO_2 formed during cleaning process just before silicon etching and tunnel barrier formation. Finally, drying with N_2 blow is done to remove any moisture. Short baking (120 °C, 5 minutes) on hot plate is preferred prior to spin coating to remove any residual moisture remaining on the chip.

3.1.2. Photolithography

Lithography is a process to generate desired patterns of thin films by removing parts of a thin film or the bulk of a substrate using a sequence of chemical steps. Photolithography uses light in order to transfer a geometric pattern from a mask to a light-sensitive photoresist on the substrate. A series of chemical treatments, as described below, then either engraves the exposure pattern into, or enables deposition of a new material in the desired pattern upon, the material underneath the photo resist.

3.1.2.1. Surface Preparation

The wafer is initially cleaned & heated to a temperature sufficient to drive off any moisture that may be present on the wafer surface, as described above. A thin layer of ‘primer’ is applied to promote adhesion of the photoresist to the wafer by dispensing it on to the wafer and spinning it at 3000 rpm for 1 minute. This layer also acts as a water-repellant layer to avoid aqueous photoresist from reaching the substrate.

3.1.2.2. Photoresist layer

A viscous, liquid solution of S1813 (photoresist) is dispensed onto the wafer, and the wafer is spun rapidly to produce a uniformly thick layer. The spin coating is run at 3000 rpm for 1 minute, and produces a layer between 1 and 1.5 µm thick. Resist thickness is proportional to the spinning velocity & viscosity of the resist. Its uniformity, to some extent, depends upon the shape of surface. A surface with sharp edges like rectangle or square produces a thick layer on edges and a uniform thin layer inside. The photo resist-coated wafer is then prebaked to drive off photoresist solvent, typically at 90°C for 2 min on a hotplate. Prebaking, in addition, improves the resist adhesion with the substrate & is essential to get a uniform line width.

3.1.2.3. Resist Exposure & Development

After prebaking, the photoresist is exposed to a pattern of intense UV light using a mask between the UV source & the resist. In order to make sure that required patterns are at desired places on the chip, mask is aligned with the chip using alignment marks before UV exposure. A small gap of around 20 um is maintained between the substrate and mask. Subsequently, substrate is exposed to the UV light for 8.5 seconds at low vacuum mode. After exposing, it is followed by post baking for 1 min at temperature of 120 °C. In a positive photoresist, on UV exposure, inter-molecular bonds break which makes it soluble in a selective chemical called resist developer (MF319). As a result, the part of resist exposed to light dissolves in the developer while the remaining part remains intact, when substrate is soaked in it for 1 minute.

3.1.3. Oxide Etching

After selectively removing the resist, it is followed by hard baking for 5 min at temperature of 120 °C in order to proceed for oxide etching. SiO_2 is removed by soaking in the solution of BHF for 5 minutes. The time required to etch depends upon the thickness of the layer present. For our fabrication, it was sufficient to remove the 300 nm layer present. After the etching processes, remaining photoresist is removed by ultrasonically soaking in acetone + IPA solution for 30 seconds, followed by nitrogen blow for drying.

3.1.4. Silicon Oxidation: The Tunnel Barrier & Pad Oxide

Silicon oxidation is the process in which a thin layer of SiO_2 is grown over the Si surface. Si oxidation can be done in various ways:

3.1.4.1. Thermal Oxidation

The technique forces an oxidizing agent to diffuse into the wafer at high temperature and react with it, shown in figure 3.1. Deal-Grove model is often used to predict the rate of oxide growth. It is usually performed at a temperature between 800°C and 1200°C, resulting in so called high temperature oxide layer [38]. It may use either water vapor (usually UHP steam) or molecular oxygen as the oxidant; called as ***wet*** oxidation and ***dry*** oxidation respectively. A wet oxidation, though faster as water molecule diffuses faster than oxygen, gives a bad quality oxide. In our device fabrication, dry oxidation was used to deposit 300 nm oxide layers over Silicon chip which gives a good quality layer but is comparatively slower. The reaction is one of the following:

Wet Oxidation: $Si + 2H_2O \rightarrow SiO_2 + 2H_{2\,(g)}$

Dry Oxidation: $Si + O_2 \rightarrow SiO_2$

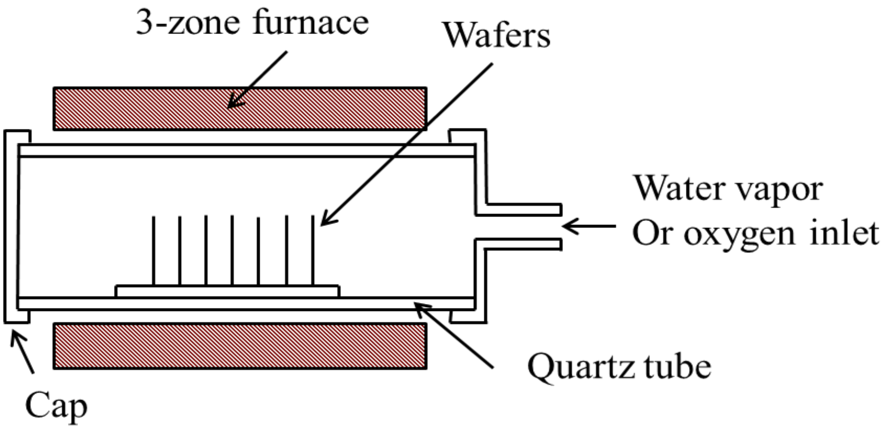

Figure 3.1. A Thermal Oxidation Chamber, it use either water vapor (usually UHP steam) or molecular oxygen as the oxidant; called as *wet* oxidation and *dry* oxidation respectively.

The oxidizing ambient may also embrace certain percent of hydrochloric acid (HCl) which helps to take away metal ions that may occur in the oxide. Thermal oxide includes silicon consumed from the substrate and oxygen supplied from the ambient. Thus, it grows both down into the wafer and up out of it. According to the Deal-Grove model, the time *t* required to grow an oxide of thickness $\boldsymbol{X_o}$, at a constant temperature, on a bare silicon surface, is:

$$\boldsymbol{t = \frac{X_o^2}{B} + \frac{X_o}{B/A}}$$

Where, the constants A and B encapsulate the properties of the reaction and the oxide layer, and represents the parabolic (diffusion-controlled) & linear (surface reaction controlled) parts of rate constant respectively. Presence of impurities like dopant atoms affects the rate of oxidation depending upon the type of dopant. Boron atoms, because of their high diffusivity, affect the diffusion of oxidant molecules in already grown oxide layer & thus affect the parabolic part of rate constant. Phosphorous & Arsenic, on the other hand, affects the surface reaction at the interface and, hence, improves the linear part of rate constant.

Advantage of thermal oxidation is that give best control of oxide thickness. However, t it has a high temperature requirement which may not be suitable for post-metal fabrication steps. It also requires a costly setup of a thermal chamber. Moreover, it's a slow process as compared to other existing oxidation processes which makes it time consuming for thick oxide layer formation. In addition, high temperatures may lead to dopant diffusion, a risky effect in current devices which requires a carefully controlled doping profile.

3.1.4.2. Ozone Oxidation

Ozone oxidation utilizes Ozone, O_3 molecule as the reactant in place of O_2 molecule for oxidation. Ozone gas can be easily formed when UV light is exposed to O_2 gas, which breaks into nascent Oxygen and react with O_2 to form O_3 . As O_3 is much more reactive than O_2, oxidation is much faster at low temperatures as compared to thermal oxidation. As no costly heating equipment is required, it's much cheaper and smaller as compared to its thermal counterpart. Brief oxidation process is shown in figure 3.2.

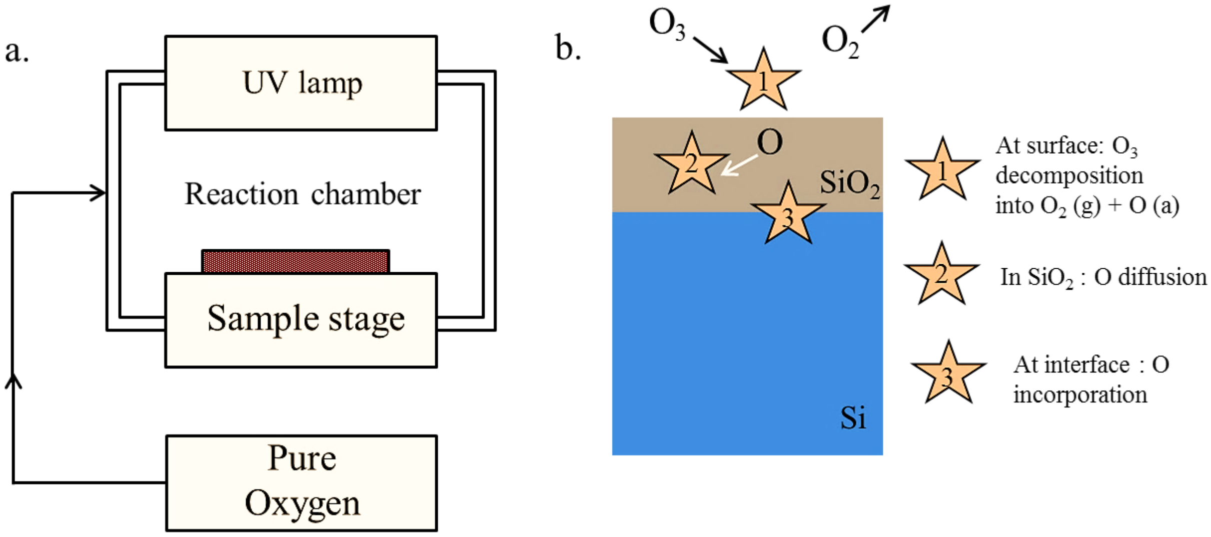

Figure 3.2. Ozone oxidation (a) Oxidation configuration, (b) Pictorial representation of oxidation at Si surface by ozone molecule [39]

It has been observed that ozone oxidation gives a much better interface because of the creation of very thin transition region which makes it a robust method for high quality, extremely thin oxide layers. In addition, oxide layer deposited is independent of the orientation of the Si lattice, which facilitated the growth of high quality oxide film at room temperature even on polycrystalline silicon [40]. It also gives constant oxide etching rate in HF. SiO_2 grown by exposure to ozone has been shown to have a reduced sub-oxide transition layer, reduced strain and greater reliability [39]. Moreover, O_3 can be generated in high concentrations, while the molecules exhibit only low kinetic energies according to the thermal velocity distribution. This is a clear advantage over plasma oxidation techniques, which causes sample damage due to highly energetic particle bombardment.

3.1.5. Physical vapor deposition (PVD): Ferro-magnet /Gold contacts

Metal deposition in the CMOS industry is primarily done through PVD methods while chemical vapor deposition (CVD) methods are used for dielectric (oxides) deposition. The two main PVD methods are evaporation and sputter deposition. E-beam evaporation technique was used in our device fabrication for the deposition of Ferro-magnet and Gold contacts.

3.1.5.1. E-beam evaporation

The Figure 3.3 shows a typical setup for e-beam evaporation. It consists of a vacuum chamber, where the substrate is loaded upside down on a holder. The bottom of the chamber consists of crucibles where the metals to be deposited are placed. An electron arc such as the ones made of tungsten acts as the source of e-beam. A high voltage is applied between the crucible and the electron gun. The electrons from the arc are focused on to the crucible by using a perpendicular magnetic field. The electron beam vaporizes the metal in the crucible and the vapor gets deposited all over the chamber but mostly on the substrate that is right on top of the crucible [41].

A microbalance consisting of a quartz crystal, which oscillating frequency depends on its mass, is placed near substrate holder. As the metal get deposited on the crystal, its frequency shifts. Based on the change in frequency, the amount of material deposited is calculated. This is used as in-situ measurement to get metal layers of desired thickness to be deposited.

The quality of layers deposited by PVD methods depends on the cleanliness of the surface and the aspect ratios of the structures in the surface.

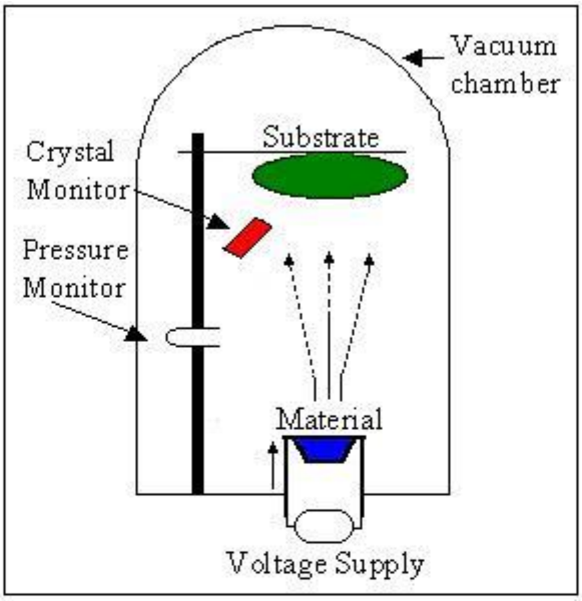

Figure 3.3. E-Beam Evaporation [41], It consists of a vacuum chamber, where the substrate is loaded upside down on a holder. An electron arc acts as the source of e-beam. A high voltage is applied between the crucible and the electron gun. The electrons from the arc are focused on to the crucible by using a perpendicular magnetic field and it vaporizes the metal to deposit over substrate.

3.1.5.2. Ion beam etching – Contact definition

Since the e-beam evaporation deposits the metal all over the substrate, we need to remove the metal except on the contact areas which can be done by Ion beam etching. This method is an anisotropic and highly directional etching method.

The type of ion beam etching depends on the ions used. Typically Ar ions are used for normal etching whereas reactive ions such as Cl^- are used in reactive ion beam etching. Sometimes, a mixture of Ar^+ and a reactive chemical is used. In this case, Ar etches the material and chemical reacts with the surface to remove any passivation layer that is formed. This is known as chemically assisted ion beam etching [42]. Figure 3.4 depicts the setup of an ion beam etching machine and is same for all of the types discussed above.

The substrate is loaded in a rotating fixture and placed at an angle of 5° with the vertical. Rotating the sample ensures uniform removal of unwanted materials. The chamber is pumped to very low vacuum. Ar gas is pumped via the inlet and is ionized. The ionized Ar is accelerated using a high electric field and the accelerated beam is collimated to get a highly directional beam. The high energy beam hits the substrate etching the exposed material. A neutralizing filament produces electrons, either to neutralize the Argon ions before they reach the substrate or the surface of the substrate in order to remove the possibility of having a trapped charge.

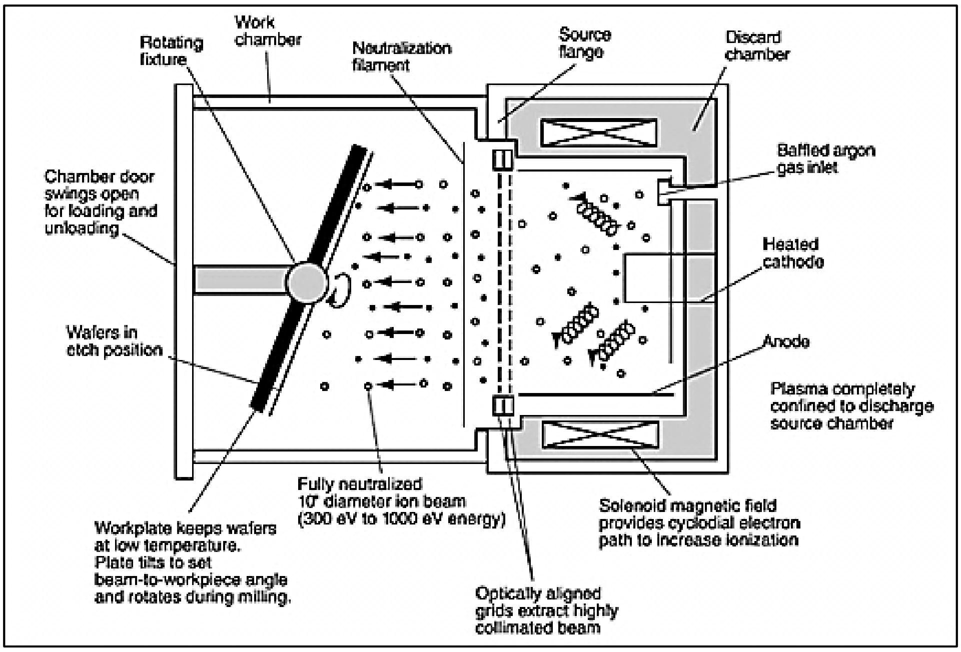
Work chamber
Rotating fixture
Neutralization filament
Source flange
Discard chamber
Baffled argon gas inlet
Chamber door swings open for loading and unloading
Heated cathode
Wafers in etch position
Anode
Plasma completely confined to discharge source chamber
Fully neutralized 10" diameter ion beam (300 eV to 1000 eV energy)
Solenoid magnetic field provides cyclodial electron path to increase ionization
Workplate keeps wafers at low temperature. Plate tilts to set beam-to-workpiece angle and rotates during milling.
Optically aligned grids extract highly collimated beam

Figure 3.4. The Ion Beam Etching chamber [42], the chamber is pumped to very low vacuum. Ar gas is pumped via the inlet and is ionized. The ionized Ar is accelerated using a high electric field and the accelerated beam is collimated to get a highly directional beam. The high energy beam hits the substrate etching the exposed material.

3.2. Device Fabrication Process Steps

3.1.1. Wafer cleaning & Thermal oxidation

The Si/SiO_2/FM contacts were fabricated on p type (B doped) silicon (100) Si substrate with 2 µm active Si layer. Silicon with three different Boron concentrations were measured to be $5x10^{19}cm^{-3}$, $15x10^{18}cm^{-3}$ and $4x10^{19}cm^{-3}$ labeled as p Si, p+ Si and p++ Si respectively. Wafer was, firstly, cleaned using standard cleaning procedure (SC1 + SC2) as described in section 3.1.1. A 300-nm-thick SiO2 insulating layer was, then, grown by dry thermal oxidation at 1150 °C.

3.1.2. Contact hole etching: Mask 1

First, substrate was cleaned by Acetone and IPA rinsing procedure as described in section 3.1.1. After the cleaning step, the oxide layer was, then, patterned by photolithography using mask 1 and etched in buffered hydrofluoric acid (BHF) for 5 minutes as described in section 3.1.3., defining contact holes for Si/SiO_2/FM contacts followed by a Acetone + IPA cleaning step again.

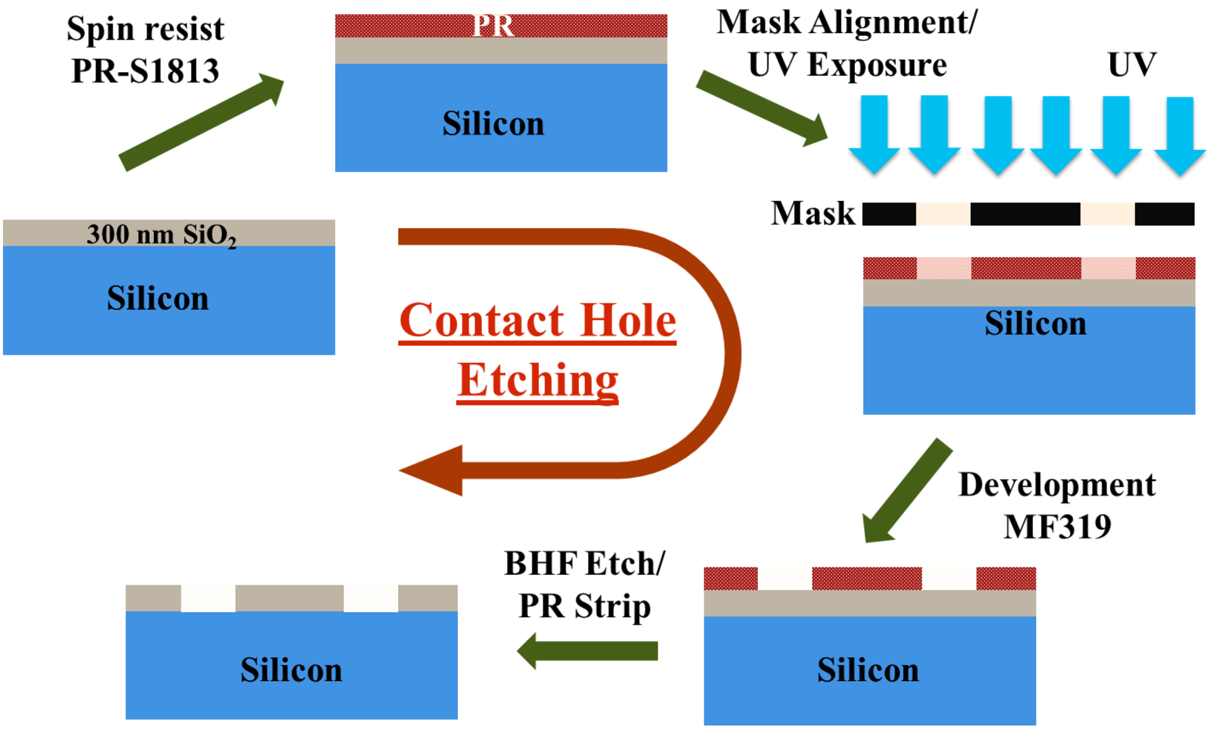
Spin resist
PR-S1813
PR
Silicon
Mask Alignment/
UV Exposure
UV
300 nm SiO_2
Silicon
Mask
Contact Hole
Etching
Silicon
Development
MF319
BHF Etch/
PR Strip
Silicon
Silicon

Figure 3.5. Contact hole etching, first UV lithography process is done and then, BHF is used to etch out the exposed SiO_2 part.

3.1.3. Tunnel barrier, Ferro Magnet (Co) and Gold (Au) deposition and Contact patterning: Mask 2

Substrate was again cleaned using Acetone + IPA cleaning step before putting in to the e-beam evaporation chamber. Then, it was followed by 30 seconds HF (2%) dipping to remove oxides layer grown during cleaning process.

Tunnel barrier was grown using Ozone oxidation method. After proper setting time for Ozone oxidation chamber, a SiO_2 tunnel barrier of thickness around 1 nm was grown using ozone oxidation with a flow rate of 1 L/min for 30 min. Ozone oxidation is self-limited oxidation process and with longer time oxidation ensures uniform oxide growth.

Then, it is transferred into the ultrahigh vacuum chamber (UHV) (base pressure 1×10^{-10} bar), layers of Ferro-magnet (Co) & gold contact, of thickness 15 nm and 10 nm respectively, were deposited sequentially from an crucible sources in the load-lock chamber. Thickness of the layers was observed using the quartz based thickness monitor present inside the chamber and e-beam evaporation was switched off after the required thickness was deposited. The ferromagnetic contacts were patterned by photolithography step using mask 2 as described in section 3.1.2. and then it was followed by Ar-ion beam etching as described in section 3.1.5.2.

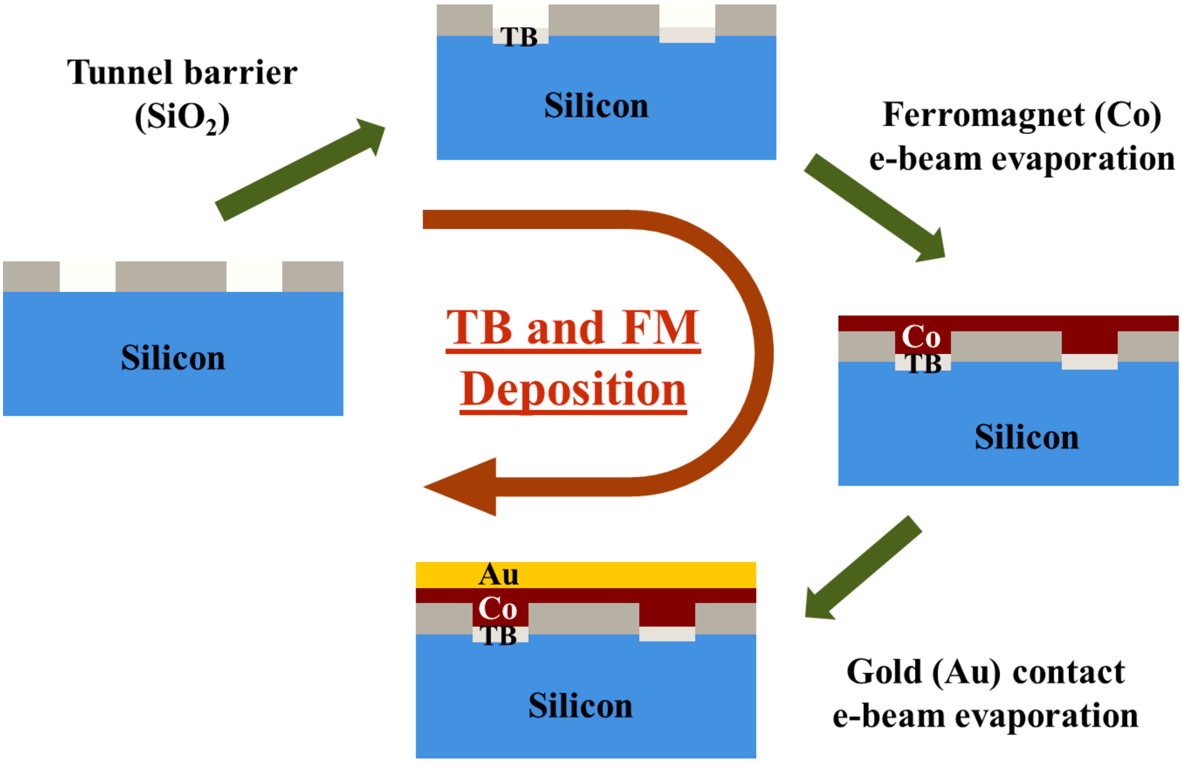
Tunnel barrier
(SiO$_2$)
TB
Silicon
Ferromagnet (Co)
e-beam evaporation
Silicon
TB and FM
Deposition
Co
TB
Silicon
Au
Co
TB
Silicon
Gold (Au) contact
e-beam evaporation

Figure 3.6. Tunnel barrier deposition by Ozone oxidation and Ferro-magnet/gold contact deposition by e-beam evaporation

Then, it is transferred into the ultrahigh vacuum chamber (UHV) (base pressure 1×10^{-10} bar), layers of Ferro-magnet (Co) & gold contact, of thickness 15 nm and 10 nm respectively, were deposited sequentially from an crucible sources in the load-lock chamber. Thickness of the layers was observed using the quartz based thickness monitor present inside the chamber and

e-beam evaporation was switched off after the required thickness was deposited. The ferromagnetic contacts were patterned by photolithography step using mask 2 as described in section 3.1.2. and then it was followed by Ar-ion beam etching as described in section 3.1.5.2.

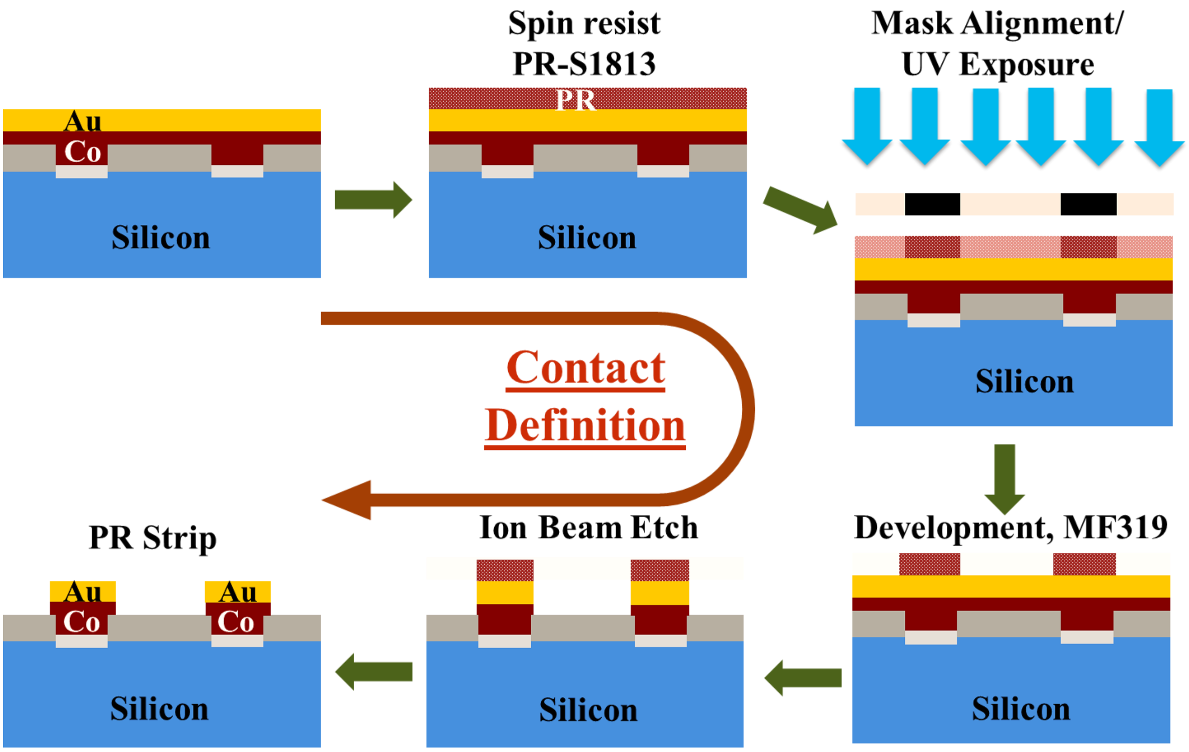

Au
Co
Silicon
Spin resist
PR-S1813
PR
Silicon
Mask Alignment/
UV Exposure
Silicon
Contact
Definition
PR Strip
Au
Co
Au
Co
Silicon
Ion Beam Etch
Silicon
Development, MF319
Silicon

Figure 3.7. Ferro-magnet/gold contact patterning, UV lithography followed by ion beam etching

3.1.4. Contact pads deposition and patterning: Mask 3

Each contact has a tunnel area of 215×100 μm^2, which allows one to attain a sufficiently good signal-to-noise ratio. The final device was designed & fabricated in a way that it consists of a Si substrate with multiple contacts, such that transport measurements can be performed in different geometries. Finally, one more photolithography step was done for patterning the chromium Cr/gold Au contact pads for connecting the chip with bond wires for measurements and Cr/Au was deposited using e-beam evaporation to the thickness of 10 nm and 100 nm respectively. The main role of Cr is to enhance the adhesion of gold contact pad over SiO_2.

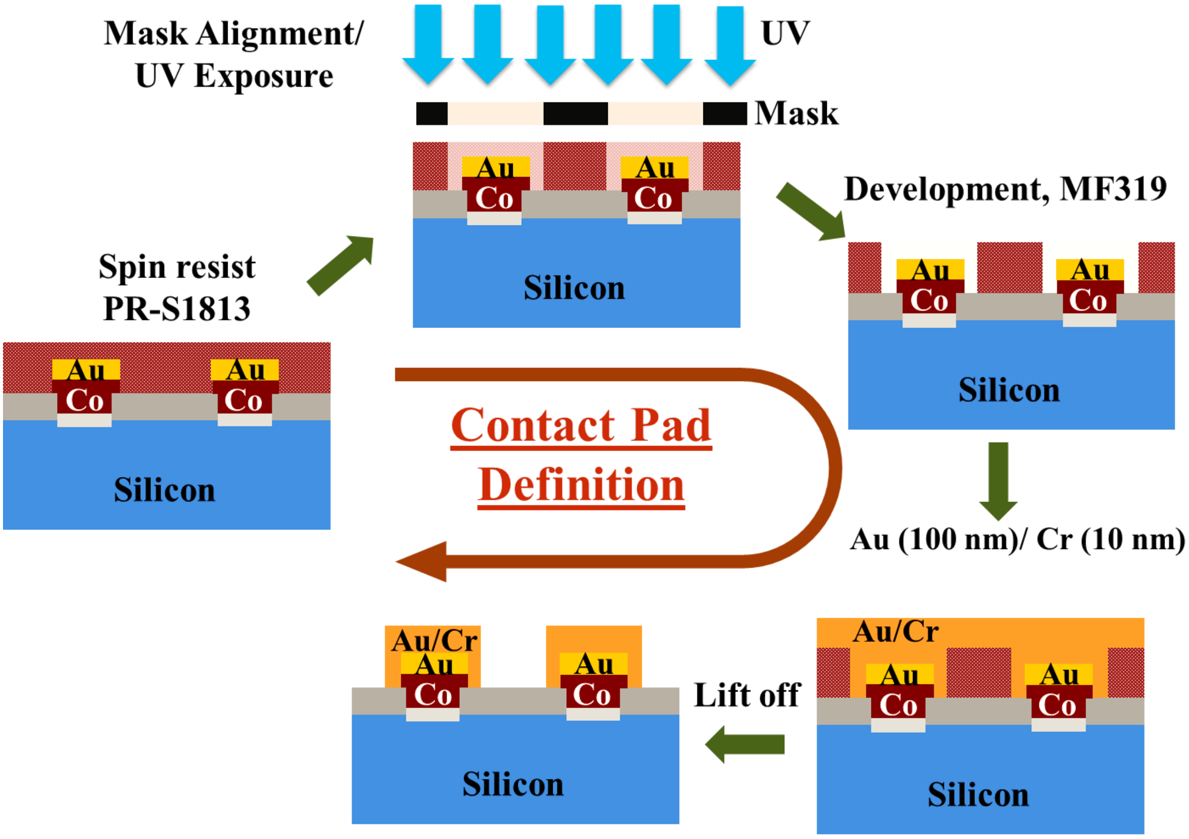
Mask Alignment/
UV Exposure
UV
Mask
Au
Co
Au
Co
Silicon
Development, MF319
Au
Co
Au
Co
Silicon
Spin resist
PR-S1813
Au
Co
Au
Co
Silicon
Contact Pad
Definition
Au (100 nm)/ Cr (10 nm)
Au/Cr
Au
Co
Au
Co
Silicon
Lift off
Au/Cr
Au
Co
Au
Co
Silicon

Figure 3.8. Contact pads definition, lift off method is used to pattern the contact pads

Chapter 4

Measurements and Discussions

In this chapter, both electrical and spin transport measurements performed on microfabricated Cobalt/SiO_2 tunnel barrier/p-type silicon devices are discussed. The Schottky barrier parameter has been tailored by changing the boron doping concentration in the silicon. These studies involve determining the carrier densities, mobility, diffusion coefficients, etc. in differently doped silicon substrates using Hall measurement technique, the Schottky barrier properties at the tunnel junction interfaces, as well as the change in the spin-signal with a magnetic field, temperature, and applied electrical bias voltage. Spin signal amplitude, spin resistance- area product, spin polarization, and spin lifetime are determined. Temperature and doping dependence measurements are discussed. The role of Schottky barrier on spin signal and anomalous spin reversal behavior are also discussed.

4.1. Hall measurement

Hall measurement is done in order to measure doping concentration and hole mobility for different p-type semiconductor [43]. Hole mobility is very much importance to determine the diffusivity of carriers inside semiconductor which helps to find out the spin diffusion length. Doping concentration is necessary to determine the Schottky barrier width and to make comparison of spin signals for different doping concentration. Determination of Schottky barrier width is very important because it changes the junction resistance that ultimately effects spin transport through the junction. Also, resistivity measurements were done on the same Hall bar structure shown in figure 4.1 by using four probe point method.

Hall bar structure shown in figure 4.1 was microfabricated on silicon to perform Hall measurement [43]. When a constant electric current I, flows through the long axis of the bar is subjected to a uniform magnetic field, directed perpendicular to the current flow, holes are subjected to Lorentz force given by,

$$\vec{F} = q\left[\vec{E} + \left(\vec{v} \times \vec{B}\right)\right] \tag{4.1}$$

where, $\vec{E}$ is electric field, $\vec{B}$ is perpendicular magnetic field, $\vec{v}$ is average carrier velocity and q is the charge of the carrier.

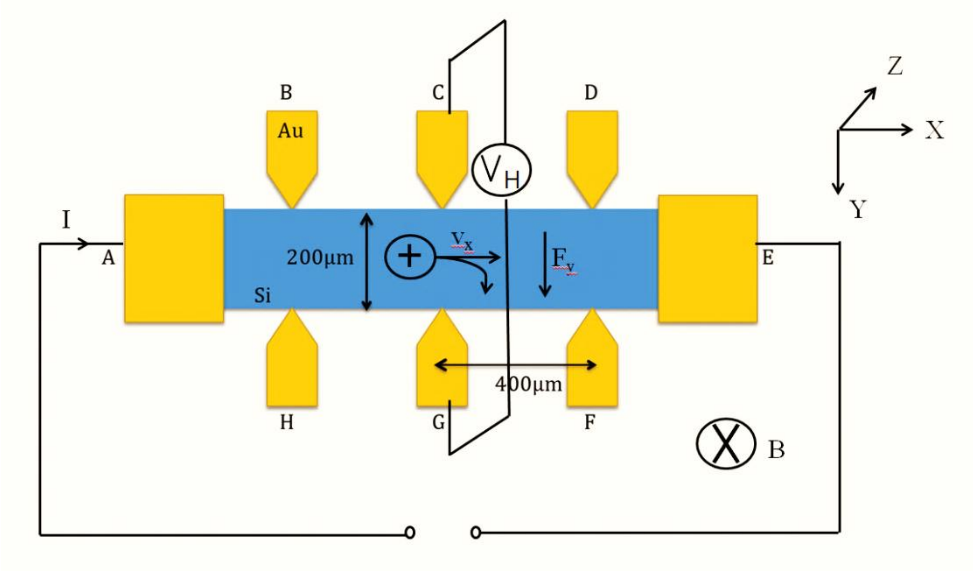

Figure 4.1. Hall bar structure for Hall effect measurement and resistivity measurement. Current is passed along x-direction from A to E. For Hall effect measurement, magnetic field is applied in z-direction and voltage can be measured between contacts B-H, C-G or D-F.

Holes are deflected to one side of the bar in the transverse direction and accumulation of positive charge occurs there whereas, there is accumulation of negative charge on the opposite side. Hence, there is a net potential difference between the two sides of the sample that can be extracted as the Hall voltage V_H [44], given by

$$\boldsymbol{V_H = \frac{IB}{qnd} = \frac{IB}{qn_s}} \tag{4.2}$$

where, I is current, d is sample thickness, n is bulk density of carriers and n_s = nd is sheet carrier density. Measured Hall voltage is negative for n-type Si whereas it is positive for p-type Si. If we know the sheet resistance of semiconductor, which can be calculated by the use of Van der Pauw resistivity measurement or four-point probe method, we can calculate the mobility, given by

$$\boldsymbol{\mu = \frac{V_H}{R_s IB} = \frac{1}{R_s I}\frac{dV_H}{dB} = \frac{1}{qn_s R_s} = \frac{1}{qnr}} \tag{4.3}$$

where, R_s is sheet resistance, r= R_sd is bulk resistance and $\boldsymbol{\frac{dV_H}{dB}}$ inverse of the slope calculated from B-V_H plot as shown in figure 4.2.

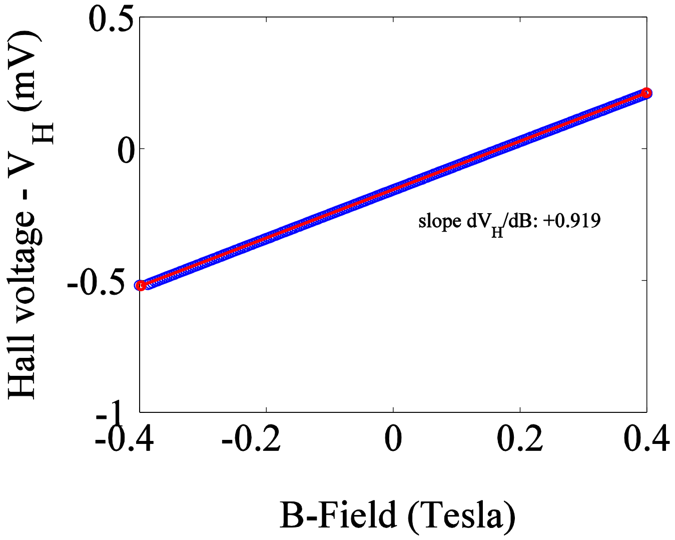

Figure 4.2. Plot between magnetic field, B Vs. Hall voltage, V_H; magnetic field was swept for hall voltage measurement and slope dV_H/dB was used to get mobility of Si with different doping concentrations.

4.1.1. Resistivity measurement

Resistivity measurement was done in order to find the sheet resistivity of silicon wafer of different doping concentration. Resistivity values are required to calculate the mobility of the carriers inside silicon and it also helps to compare the magnitude of the current transport into the silicon through the ferromagnetic tunnel contacts.

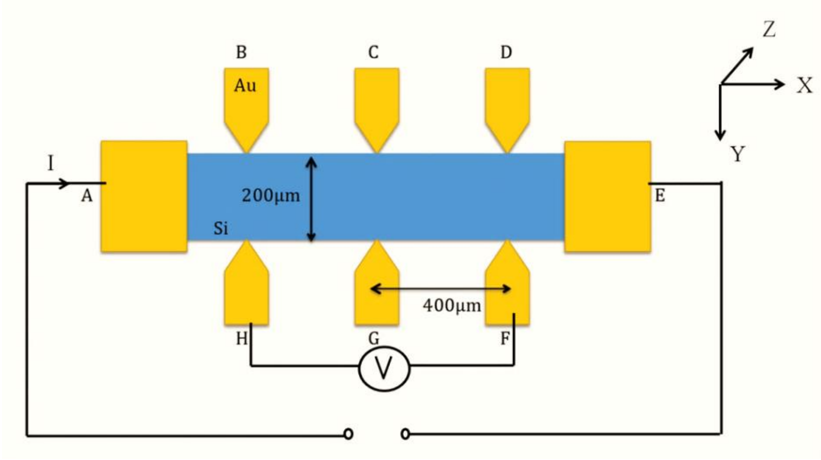

Figure 4.3. Resistivity measurement using four point probe method. Hall bar structure was used. Current was passed from contact A to E. For resistivity measurement, no magnetic field is applied and voltage can be measured between different possible combination of contacts along the same side of bar.

Same Hall bar structure was used with four point probe method to measure resistivity for p++ and p type Si. For p+ Si, Van der Pauw method was used because silicon layer was very thick and Hall measurement, which is ideal for 2D-device, was not suitable in this sample. For resistivity measurement, current was passed from contact A to E as shown in figure 4.3 and corresponding voltage was measured between two contacts of same side with different possible combination. We considered the homogeneity within the semiconductor. Note that the voltage drop across H-F is twice as large as that across H-G so that corresponding compensation should be done while taking average of resistance value.

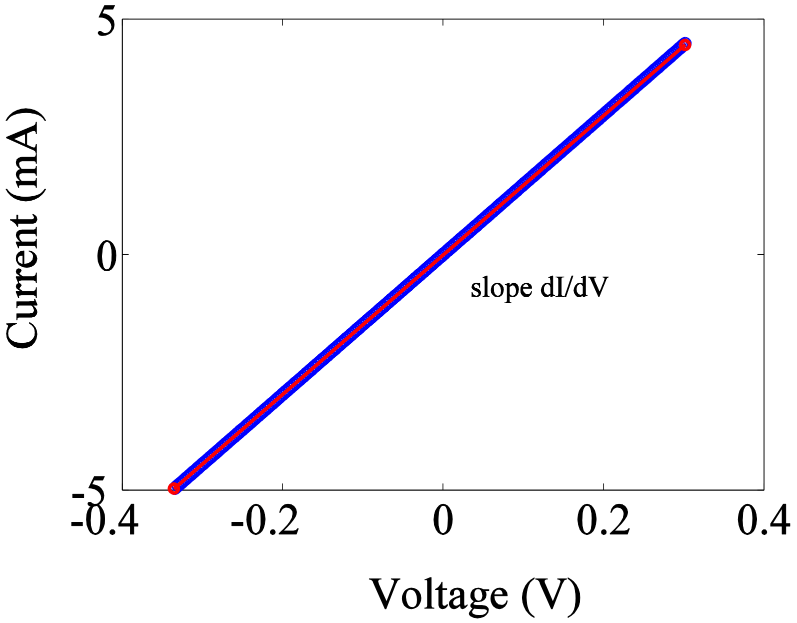

Figure 4.4. Plot between current, I and voltage, V. Voltage is swept to measure corresponding current and resistance R, was found by taking the inverse of the slope dI/dV to obtain resistivity of Si with different doping concentrations.

Then the resistivity was calculated as,

$$\boldsymbol{\rho = R\frac{Wt}{d}\ \Omega m} \qquad \textbf{(4.4)}$$

Where R=dV/dI is resistance as shown in figure 4.4, d is the distance between two contacts over which voltage is measured, W is the channel width and t is the thickness of the channel which is 2 μm for p and p++ Si devices. Calculated values of mean resistivity for p and p++ Si devices are $11\text{x}10^{-5}$ Ωm and $5\text{x}10^{-5}$ Ωm respectively.

Van der Pauw (VDP) measurement was prepared by connecting the Au wires in each corner of the p+ Si substrate which is shown in figure 4.5. Here, vertical resistance R_v and horizontal resistance R_h was measured and the resistivity of sample can be calculated by using the following VDP equation [45],

$$e^{-\pi R_v t/\rho} + e^{-\pi R_h t/\rho} = 1 \tag{4.5}$$

where, t is the thickness of the sample.

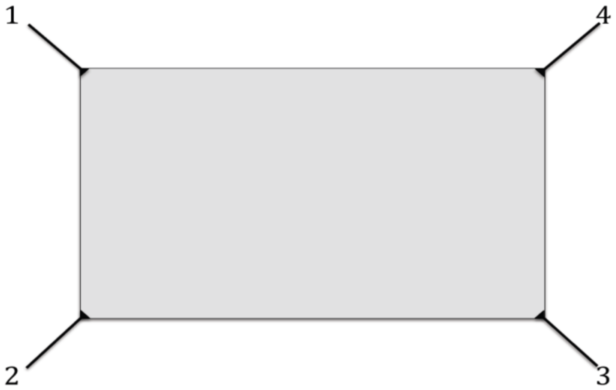

Figure 4.5. Wires are connected along the edges of four corners of Si substrate for VDP measurement

A current I_{12} was applied between terminals 1 and 2 and the voltage V_{34} is measured between contact 3 and 4. The resistance was calculated using ohm's law, $R_{12,34}= V_{34}/I_{12}$. Again, resistance $R_{21,43}$ was calculated by reversing the polarity on the both current source and the voltmeter so that it eliminated the effect of offsets in the instruments.

Then, same above procedure was repeated with current applied between the contacts 3 and 4 and voltage measured between contacts 1 and 2. The calculated resistance were $R_{34,12}$ and $R_{43,21}$. According to reciprocity theorem, $R_{12,34}= R_{34,12}$. R_v was calculated by taking average of all four measurements. The sample was square in shape and it was assumed to be isotropic so that R_h was not necessary to calculate. Hence, resistivity was calculated analytically using following equation,

$$\rho = \frac{\pi R}{ln2} t \tag{4.6}$$

where, $R= R_v= R_h$. The mean value of resistivity for p+ Si was found to be $7.2\text{x}10^{-5}\ \Omega m$.

4.1.2. Doping concentration, mobility and diffusion coefficients

Using equation 4.1, doping concentration was calculated with Hall measurement techniques. Hole carrier concentrations for p Si, p+ Si and p++ Si were found to be 5.4x10^{18} cm^{-3}, 1.5x10^{19} cm^{-3} and 2.1x10^{19} cm^{-3} respectively. Then, corresponding hole mobility was calculated using equation 4.3 which are 10.91x10^{-3} m^{2}V^{-1}s^{-1}, 5.7x10^{-3} m^{2}V^{-1}s^{-1} and 4.4x10^{-3} m^{2}V^{-1}s^{-1} respectively.

As hole has lower mobility than electron, the diffusion constant for majority carrier in p-type silicon is also lower as compared to that of n-type silicon. Diffusion constant is temperature and doping dependent [46] which is given as,

$$\boldsymbol{D = \frac{K_B T}{q}\,\mu} \qquad \textbf{(4.7)}$$

where, μ is the carrier mobility, K$_B$ is Boltzmann constant and T is the temperature. The values of D were found to be 2.72x10^{-4} m^{2}s^{-1}, 1.42x10^{-4} m^{2}s^{-1} and 1.33x10^{-4} m^{2}s^{-1} respectively for p Si, p+ Si and p++ Si. All above values are shown in table no. 4.1.

Table 4.1. Resistivity, doping concentration, carrier mobility and diffusion coefficients of different Si

Silicon	Resistivity *Ωm*	Doping concentration cm^{-3}	Carrier mobility m^{2}V^{-1}s^{-1}	Diffusion coefficients m^{2}s^{-1}
p-	10x10^{-2}	1.34x10^{15}	4.66x10^{-2}	11.65x10^{-4}
P	11x10^{-5}	5.4x10^{18}	10.91x10^{-3}	2.72x10^{-4}
p+	7.2x10^{-5}	1.5x10^{19}	5.7x10^{-3}	1.42x10^{-4}
p++	5x10^{-5}	2.1x10^{19}	5.1x10^{-3}	1.33x10^{-4}

From table 4.1, it is clearly seen that carrier mobility decreases with increase in doping concentration and the reason behind this is obviously increase in scattering. Hence, diffusivity is also decreasing with increasing doping concentration.

4.2. Schottky barrier height and width

When a metal and a semiconductor are brought in contact, an electrostatic potential barrier is created at the interface of these two materials, which is called as Schottky barrier. As Schottky barrier resistance is also a part of the junction resistance and the width of Schottky barrier, which changes with doping, is also one determining factor for the spin current transport through the ferromagnetic tunnel junction. Large Schottky barrier width leads to diode like behavior whereas small Schottky barrier width leads to tunnel device like behavior. We require tunneling current in order to have large spin accumulation.

The height of Schottky barrier is mainly determined by the differences in the work function between metal and semiconductor. However, there is still not sufficient understanding about the complete determining factors for the Schottky barrier height (SBH) [47] [48] [49]. Here, temperature dependence I-V characteristics were analyzed using thermionic emission (TE) theory to determine the SBH [48]. Very low doped p- type Si sample was prepared so that it shows rectifying behavior with good saturation reverse biased current. For highly doped case, tunneling behavior dominates and TE theory is not valid. It involves following steps:

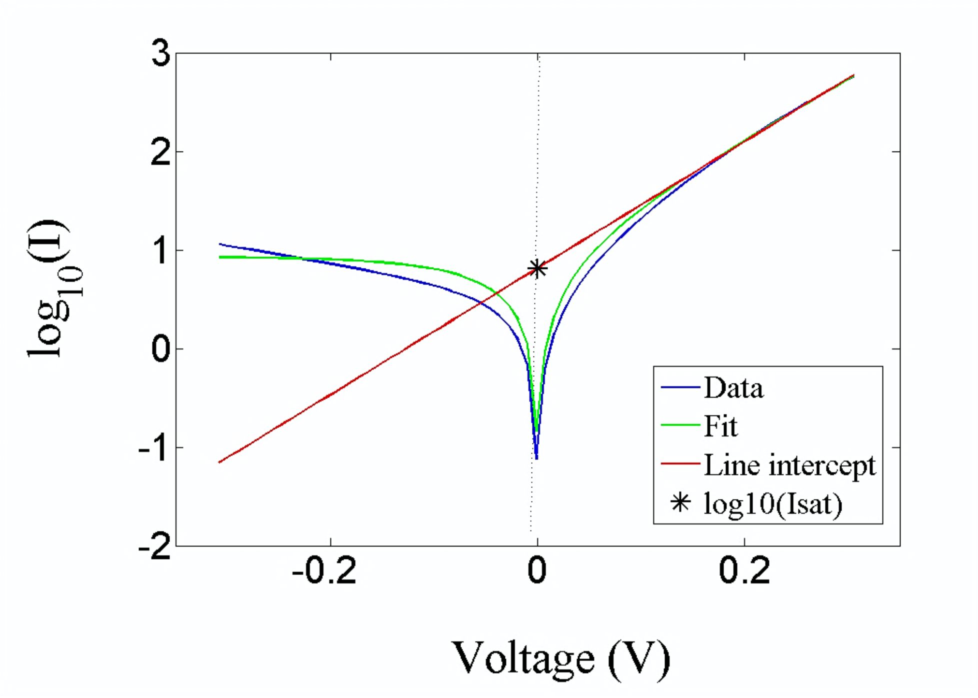

Figure 4.6. Log_{10}I Vs. V plot. Line intercept which is extended from the higher forward bias $\log_{10}$I Vs. V plot to V=0 gives saturation current.

1. The I-V characteristics in the metal to semiconductor junction can be written as

$$I = I_{sat}\left(\exp\left(\frac{qV_a}{nK_BT}\right)-1\right) \qquad \textbf{(4.8)}$$

where, I_{sat} is the saturation current that can be obtained from the straight line intercept of $\log_{10}I$ at V=0 as shown in figure 4.6. This straight line also gives slope of $\log_{10}I$ Vs. V plot at higher bias which is shown in figure 4.6. I_{sat} can also be expressed as,

$$I_{sat} = A.A^{*}T^{2}\exp\left(\frac{-\phi_B}{K_B T}\right) \qquad \textbf{(4.9)}$$

where, A is Area of junction (100*200 μm^2), A* is Richardson coefficient (1.2 x 10^{-6} Am^{-2}K^{-2}) , T is Temperature in Kelvin, K_B is Boltzmann constant (8.617 x 10^{-5} eVK^{-1}), ϕ_B is Schottky barrier height and n is ideality factor.

2. Saturation current was determined at different temperature up to 253 K. However, we could not go below 253 K because of the freezing of the carriers. We can modify expression for I_{sat} as

$$\log\left[\frac{I_{sat}}{A.A^{*}T^{2}}\right] = \frac{-\phi_B}{K_B T} \qquad \textbf{(4.10)}$$

Comparing this equation with y=mx with slope, m= $\frac{-\phi_B}{K_B}$ = $\frac{-\phi_B}{8.617e-5}$ which can be calculated from $\log\left[\frac{I_{sat}}{A.A^{*}T^{2}}\right]$ Vs. $\frac{1}{T}$ plot with linear fitting shown in figure 4.7.

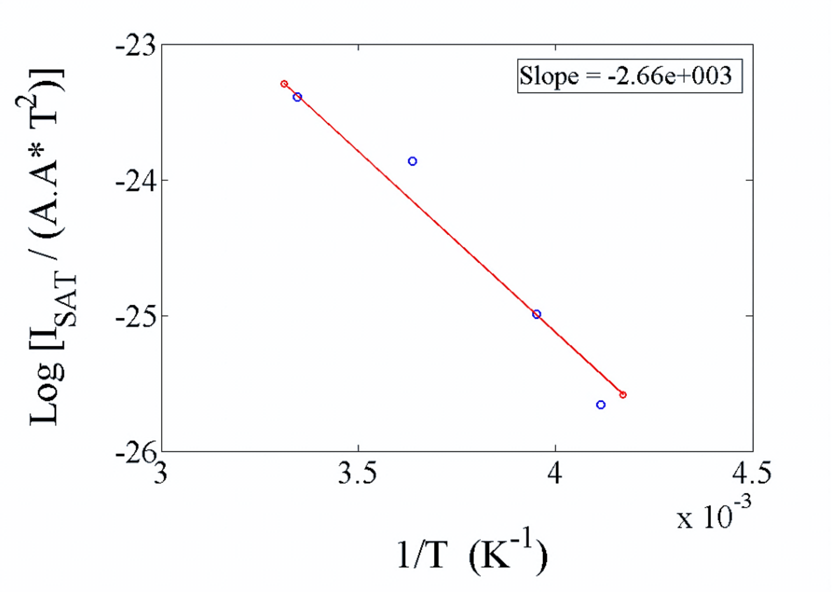

Figure 4.7. $Log\left[\frac{I_{sat}}{A.A^{*}T^{2}}\right]$ Vs. $\frac{1}{T}$ plot from which we can calculate the slope that gives SBH after multiplying with K_B.

Finally we can get schottky barrier height as,

$$\phi_B = (-slope * 8.617e-5) \quad \text{eV} \tag{4.11}$$

which was found to be 0.229 eV

Schottky barrier width can be calculated as,

$$\boldsymbol{W} = \sqrt{\frac{2\epsilon_s(V_I - V_a)}{q.n_p}} \qquad \textbf{4.12)}$$

$$\boldsymbol{W} = \sqrt{\frac{2\epsilon_s\left(\varphi_B + \frac{kT.ln\left(\frac{n_p}{n_i}\right)}{q} - V_a\right)}{q.n_p}} \tag{4.13}$$

where, $\boldsymbol{V_I = \varphi_B + \frac{kT.ln\left(\frac{n_p}{n_i}\right)}{q}}$ is built in potential, ϵ_s is the dielectric constant of the SC and n_p is the constant charge carrier density in the depletion region, q is charge, φ_B is the Schottky barrier height, $\boldsymbol{n_i = \sqrt{N_C N_V} e^{-E_g/2kT}}$ is the intrinsic charge carrier density and V_a is applied voltage [37] .

Calculated φ_B from very low doped p- Si sample was 0.23 eV, n_i is set to 10^{10} cm^{-3} [46], ϵ_s = 11.9 ϵ_o and V_a is set to 0 V. Schottky barrier width was found to be 13.52 nm,8.26 nm and 7.02 nm approximately for p, p+ and p++ Si devices respectively. For p- Si, it was found to be very high, which was 736 nm as shown in table 4.2.

Table 4.2 Schottky barrier width for different Si

Silicon	**p-**	**p**	**p+**	**p++**
Schottky barrier width (nm)	736	13.52	8.26	7.02

4.3. Hanle measurement: Spin accumulation and detection

As explained in the theory section 2.4, the existence of spin accumulation in Silicon can be verified by using the Hanle effect. This was measured in three terminal device, shown in figure 4.8, where middle electrode is FM/TB/Si contact which is used for both injection/extraction and detection, outer two electrodes are reference gold contact used for current injection/extraction and voltage detection separately. Size of middle contact is 200 µm x 100 µm. The main advantage of using 3-terminals method instead of two terminals method is that it omits channel resistance and also, reference contact resistance. As discussed, the variation of voltage with respect to applied perpendicular magnetic field for a constant current bias gives rise to a characteristic Lorentzian Hanle curve.

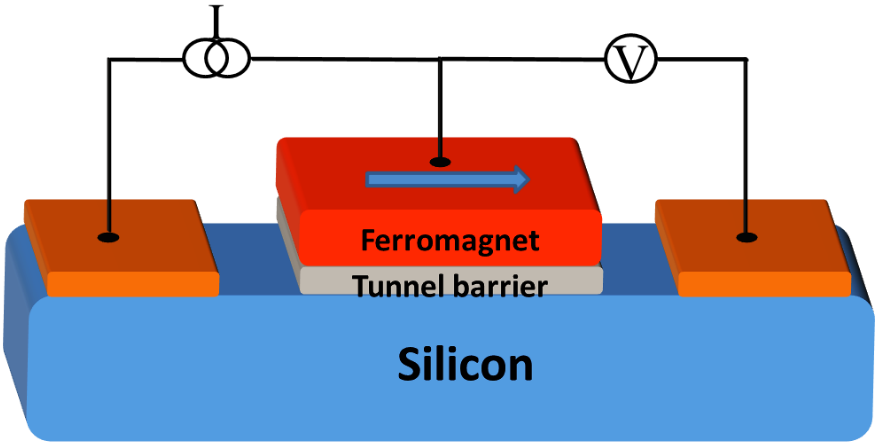

Figure 4.8. Three terminal device, where middle electrode is FM/TB/Si contact which is used for both injection/extraction and detection, outer two electrodes are reference gold contact used for current injection/extraction and voltage detection separately. Size of middle contact is 200 µm x 100 µm.

4.3.1. Very highly doped p++ Silicon

Fabrication was started with very highly doped p++ Si wafer with doping concentration of 2.1×10^{19} cm^{-3} and three terminal device with Co/Oz. SiO2/p++ Si was prepared to realize Hanle measurement. Spin injection was detected successfully as shown in figure 4.9 for -800 mV bias. The experimental data is shown by the open blue circles. The Lorentzian fit in the solid red line was calculated as per the formula, $\boldsymbol{\Delta\mu(B)} = \frac{\boldsymbol{\Delta\mu(0)}}{\boldsymbol{1+(\omega_L\tau)^2}}$ and the same was used to calculate the spin lifetime τ.

4.3.1.1. Spin Lifetime & Diffusion length

From the Hanle curve for spin injection and extraction from sample Co/Oz. SiO_2/p-Si, we could get many interesting parameters to analyze the spin transport in Silicon. The first of them as explained above is the spin relaxation time τ, from half width half maximum of Hanle curve. Spin lifetimes was found to be 49 ps for spin injection as per the fit. The diffusion length for spin is calculated as $\boldsymbol{L_D} = \sqrt{\boldsymbol{D\,\tau}}$, where D = 1.33 x 10^{-4} m^2/s, for doping concentration of 2.1×10^{19} cm^{-3}, is the diffusion constant in Si. For the device, L_D was found to be 81 nm. The extracted value should be considered as a lower limit. It has been reported that (Ref: Dash PRB, 2011), the Hanle line width is broadened by local magnetostatic field, simply called as stray field, due to the roughness of interface. Therefore, spin life time and diffusion length are higher than what is extracted from the measurement.

4.3.1.2. High Spin Polarization

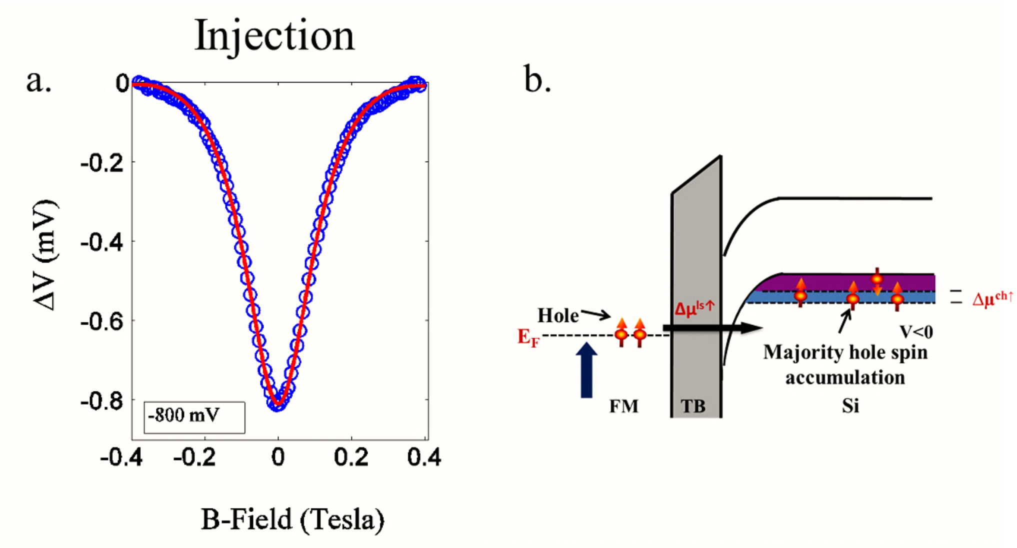

Figure 4.9. a. Hanle Lorentzian curve of spin injection for Co/Oz. SiO2/p++ Si at -800 mV bias and the amplitudes was found to be 850 μV from the Lorentzian fit; b. spin injection during reverse biased condition shown with band diagram.

The spin level splitting can be calculated from the magnitude of ΔV seen from the Hanle curve as, Δμ = 2.ΔV/TSP, where TSP = 0.35 is the tunnel spin polarization for Co/SiO_2 interface. Δμ calculated was equal to 4.85 meV. Based on these values, we could compute the spin polarization P, in Si. Spin polarization is defined as the difference between the number of majority and minority spin carriers divided by the total number of carriers. Here, splitting of valence band due to spin-orbit coupling is not taken into consideration. Hence, spin polarization can be shown to be related to Δμ, as shown below

$$\boldsymbol{P} = \frac{\Delta\mu}{2\mathrm{neD}\rho} = \frac{n^{\uparrow}-n^{\downarrow}}{n^{\uparrow}+n^{\downarrow}} \sim \mathbf{10\%} \tag{4.14}$$

Where $\rho = 5 \times 10^{-5}\Omega$m is the resistivity of p++ Si, e = $1.6\text{x}10^{-19}$ is the electron charge, D is the diffusion constant in Si & $n^{\uparrow} + n^{\downarrow}$ = n = 2.1 x 10^{19} cm^{-3} is the total carrier concentration. This, in turn gives the majority spin concentration as 1.155 x 10^{19} cm^{-3} and the minority spin concentration as 9.45 x 10^{18} cm^{-3} for spin injection. This spin polarization for hole spin injection is very high so far we have measured.

Similarly, spin extraction Hanle signal at +800 mV bias is shown in figure 4.10. The magnitude of hole spin extraction Hanle signal indicates minority hole spin accumulation inside valence band of Si and the sign of Hanle signal is also inverted. However, magnitude of Hanle signal was found to be less than that of spin injection Hanle signal. The reason behind this is explained in section 4.3.1.4. in details.

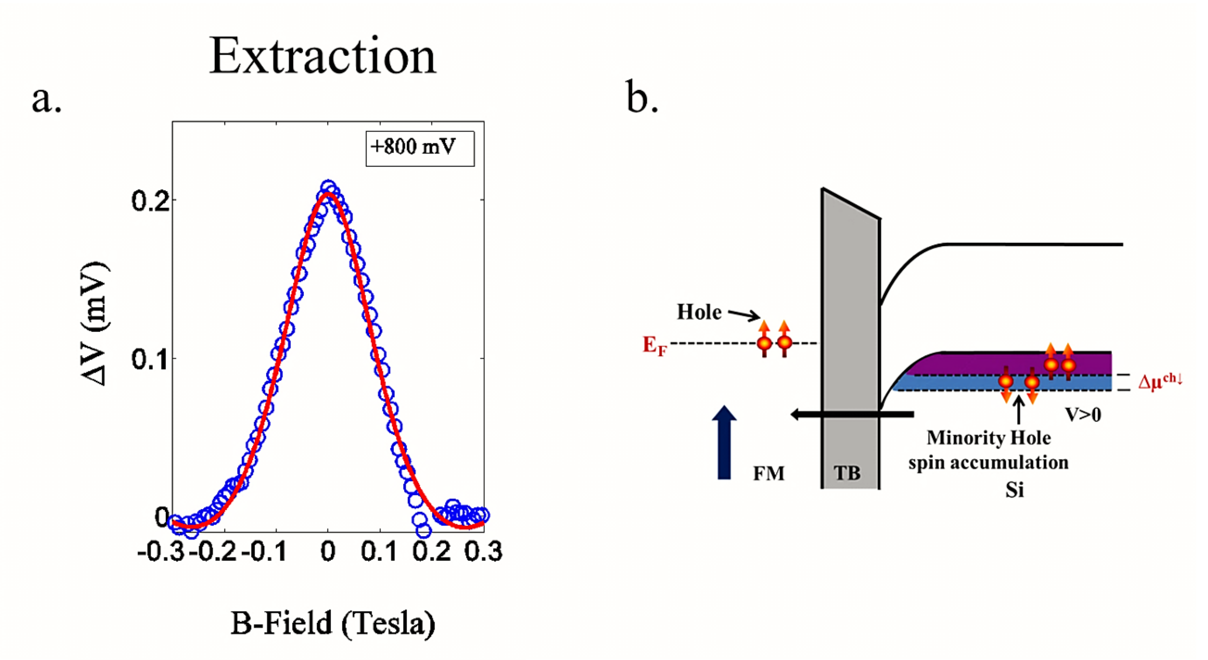

Figure 4.10. a. Hanle Lorentzian curve of spin extraction for Co/Oz. SiO2/p++ Si at +800 mV bias and the amplitudes was found to be 220 μV from the Lorentzian fit; b. spin extraction during forward biased condition shown with band diagram.

4.3.1.3. Temperature dependence Spin accumulation

Temperature dependence of spin RA signal at fixed bias -200 mV (spin injection) is shown in figure 4.11 (a), that depicts strikingly increase in spin RA signal while decreasing temperature from 300 K to 5 K. We know that the tunnel spin polarization TSP, and the spin resistance of the semiconductor r_S, depend on the temperature T, and so does the spin accumulation. For magnetic tunnel junction, TSP varies with T as $\mathbf{TSP \propto (1\text{-}\alpha T^{3/2})}$, where is constant α which depends on FM/TB interface. As we know, Hanle signal is proportional to r_s and TSP^2. TSP^2 contribute to increase in spin signal by certain factor at low temperature.

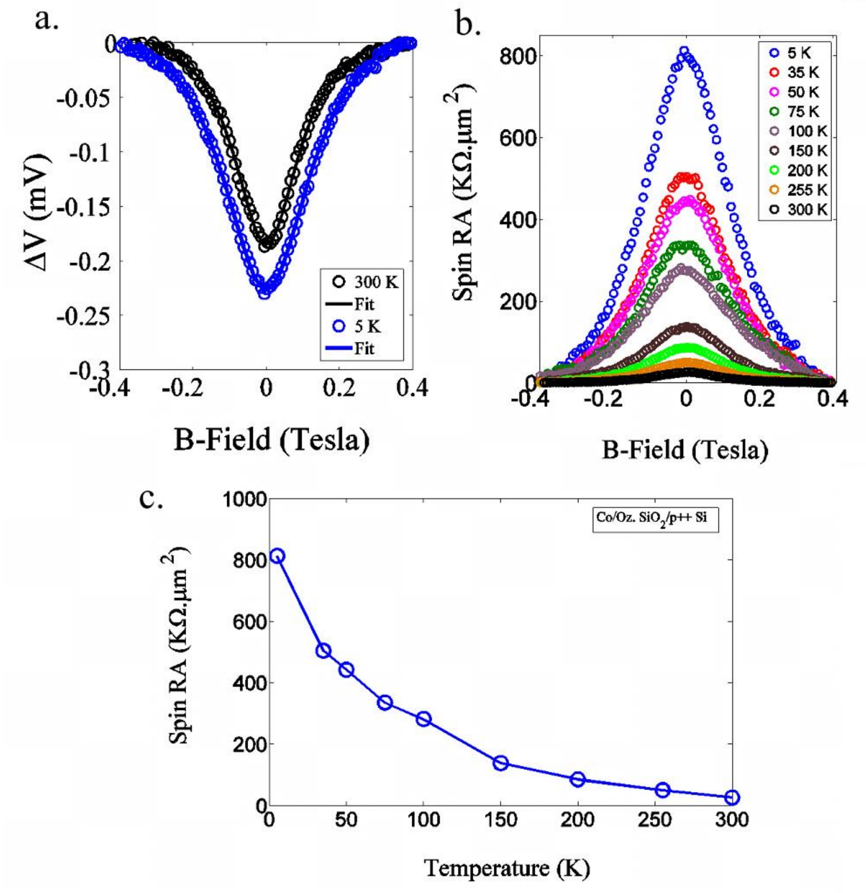

Figure 4.11. Temperature dependence of spin signal, a. Hanle signal at -200 mV, injection, variation with T, b. Spin RA variation with T, c. Spin RA amplitude variation with T

From standard theory, $r_s = \rho L_{sd}$ for spin injection and diffusion. As ρ and L_{sd} are weakly dependent on T, r_s also varies weakly with T for highly doped Si. The variation of measured spin RA amplitude with T is shown in figure 4.11 (b) and it is found to be much higher than what we expect. The reason behind this is in practice, spin RA also depends on the junction resistance and the Hanle signal was found to vary weakly with temperature but current reduces strikingly with decreasing temperature. So, spin RA increases prominently with decreasing temperature. Therefore, the temperature dependence we see in spin-RA plot is not due to change in spin signal but due to change in resistance of the contact itself.

4.3.1.4. Bias dependence plot

For each bias voltage, the magnitude of spin accumulation was detected and variations of electrical Hanle signal (ΔV) and the spin RA product (ΔV/J) of the Co/SiO2/p++Si are shown in figure 4.12 (a) and figure 4.12 (b) respectively. Both figures depict strong bias dependence which are asymmetric with respect to voltage polarity. The Hanle signal increases gradually with the reverse bias (spin holes injection V_{Si}-V_{FM} < 0), but varies slightly with the forward bias (spin holes extraction, V_{Si}-V_{FM} > 0). Spin injection produces net excess of holes with majority spin inside p++ Si. Spin extraction produces net excess of holes with minority spin inside p++ Si due to preferential extraction of holes with majority spin.

Spin RA product, which is usually taken as standard to compare different devices, decays with increase in forward bias (V_{Si}-V_{FM} > 0), while it is varying slightly with increase in reverse bias (V_{Si}-V_{FM} < 0).However, bias asymmetry case is not universal. Bias dependence spin polarization has been shown in figure 4.12 (c). With increase in Hanle spin signal amplitude, spin polarization also increases and vice-versa.

In order to understand the asymmetric bias dependence of the spin signal (or spin RA product), we can use following equation which describe the spin signal at the Si interface:

$$\boldsymbol{Spin\ RA = \Delta V/J = \gamma_d \gamma_{i/e} r_{ch} = \gamma_d \gamma_{i/e} \rho \sqrt{D\tau}} \qquad \textbf{(4.15)}$$

Where, $\boldsymbol{\gamma_d}$ is the TSP for the detection of induced spin accumulation at the Si interface, $\boldsymbol{\gamma_{i/e}}$ is the TSP for the injection/extraction of holes, $\boldsymbol{\tau}$ is spin lifetime and $\boldsymbol{r_{ch}}$ is the spin-flip resistance corresponding to Si bulk channel. Variation of spin lifetime with bias voltage is also shown in figure 4.12 (e). From this above equation, we can see that $\Delta\mathbf{V/J}$ is proportional to $\boldsymbol{\gamma_d \gamma_{i/e} \tau}$ at a given temperature (T), which depends on bias voltage. Assuming $\boldsymbol{\gamma_{d=}\gamma_{i/e}}$, bias dependence of TSP^2 ($\boldsymbol{\gamma_d \gamma_{i/e}}$) has been plotted in figure 4.12 (d).

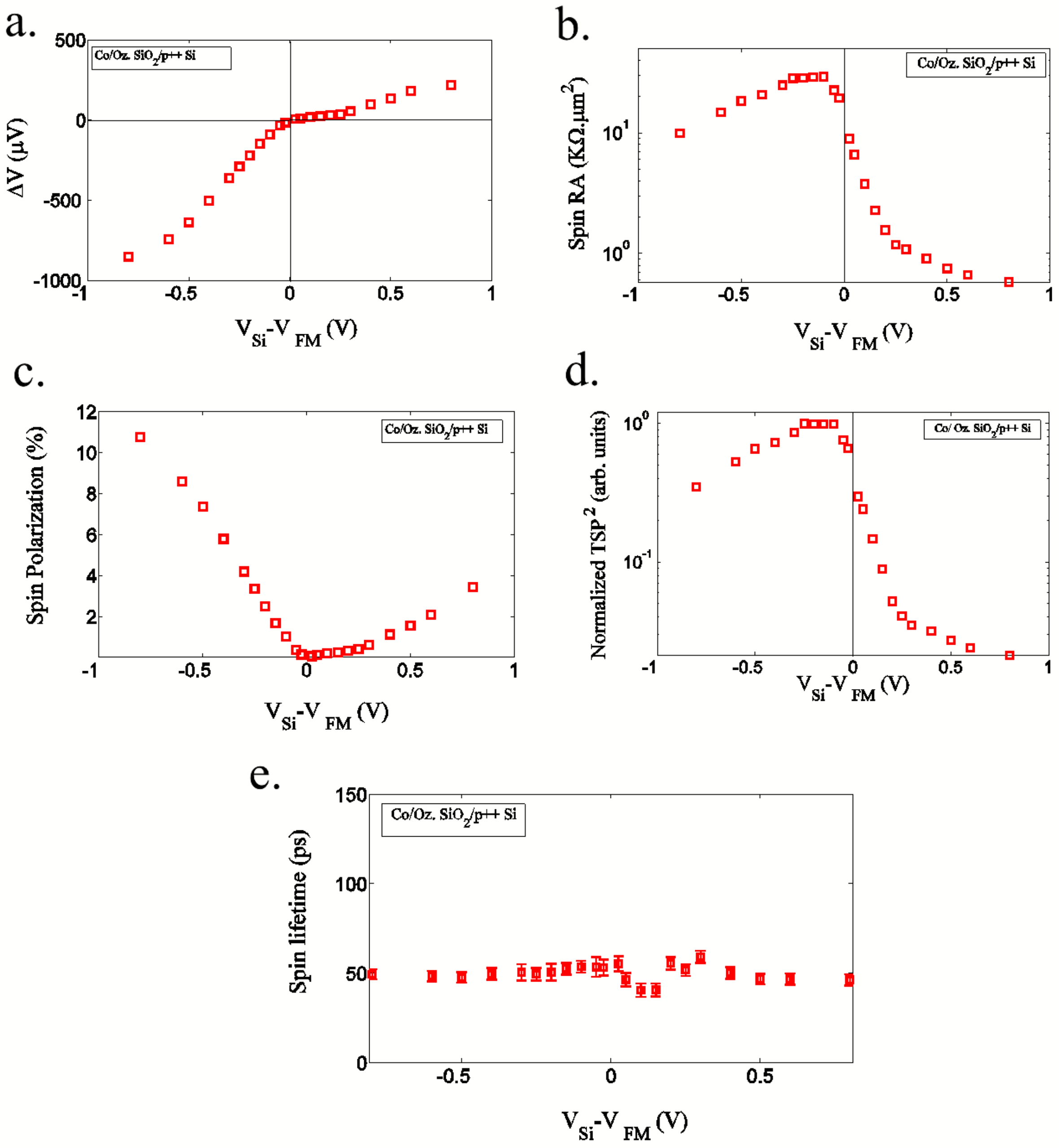

Figure 4.12. Bias dependence plots for Co/Oz. SiO2/p++ Si device, (a) Variation of spin signals with bias voltage for Co/SiO2/p++Si, measured at 295 K. Bias asymmetry Hanle signal amplitude is shown, (b) Spin RA product $\Delta \boldsymbol{V}/\boldsymbol{J}$,which is showing bias asymmetry feature. (c) Spin polarization varying with bias. It is linearly increase with bias, significantly during injection but slowly during extraction. (d) Normalized TSP2 at room temperature (e) Spin lifetime variation with bias.

The voltage dependence of the TSP^2 at room temperature was determined up to the voltages near the breakdown of the tunnel junctions. We have found that the dynamic spin polarization of the holes tunneling out of Ferro-magnet (spin holes injection V_{Si}-V_{FM} < 0) is weakly bias dependent for p++ Si. However, it drops strongly when tunneling into Ferro-magnet (spin holes extraction, V_{Si}-V_{FM} > 0). Valenzuela et al. described about this asymmetry of TSP which is due to the intrinsic asymmetry of the tunneling process [50]. During spin injection, holes originated near the Fermi level of ferromagnet are tunneling out with large polarization whereas during spin extraction, holes tunnel into the state above the Fermi level for which the polarization is significantly reduced. This means TSP above Fermi level is less than TSP below Fermi level.

4.3.2. Doping dependence – Schottky barrier width variation

In order to understand the effect of Schottky barrier width in spin injection/extraction, doping dependence of spin signal was experimented by taking p type silicon of different Boron doping concentration and were labeled Silicon as p- Si(very low doped), p Si (low doped), p+ Si(medium doped) and p++ Si (Highly doped). Corresponding doping concentration were 1.34×10^{15} cm^{-3}, 5.4×10^{18} cm^{-3}, 1.5×10^{19} cm^{-3} and 2.1×10^{19} cm^{-3} respectively. We know, width of Schottky barrier increases with decrease in doping concentration and hence, the resistance of Schottky barrier is also increased.

Considering the role of localized states at the interface, the new model has been proposed by Jansen et al [51] where two-step tunneling via localized states at the interface in parallel with direct tunneling has been treated and shown in figure 4.13. For two-step tunneling transport, R_1 is the resistance for the current transport between FM and localized state while R_2 is the resistance for the current transport localized state and Si. R_1 is mainly tunnel barrier resistance which we can assume here to be constant. R_2 is the resistance mainly contributed by Schottky barrier width. R_{tun} is the tunneling resistance for direct tunneling current.

By varying the doping concentration, the resistance R_2 was varied and corresponding spin signal behavior was observed successfully. For highly doped sample Co/Oz. SiO_2/p++ Si, all the measurement has already been demonstrated in the previous section. Next, discussions are made for medium doped sample Co/Oz. SiO_2/p+ Si.

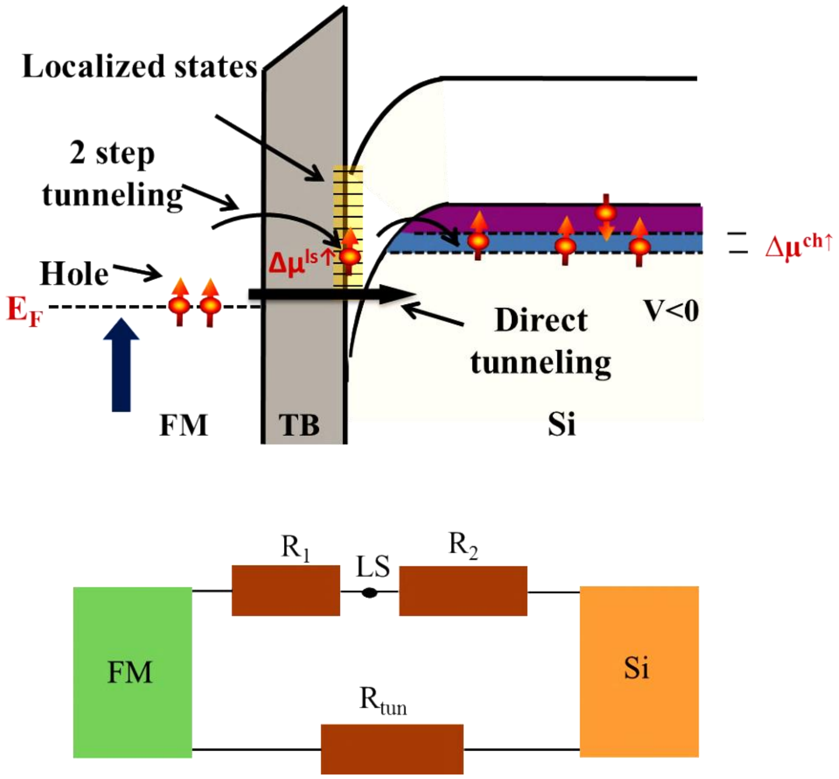
Localized states
2 step tunneling
Hole
E_F
$\Delta\mu^{ls\uparrow}$
$\Delta\mu^{ch\uparrow}$
Direct tunneling
V<0
FM
TB
Si
R_1
LS
R_2
FM
Si
R_{tun}

Figure 4.13. Two-step tunneling via localized states at the interface in parallel with direct tunneling [51]. For two-step tunneling transport, R_1 is the resistance for the current transport between FM and localized state while R_2 is the resistance for the current transport between localized state and Si. R_{tun} is the tunneling resistance for direct tunneling current.

4.3.2.1. Medium doped p+ Silicon

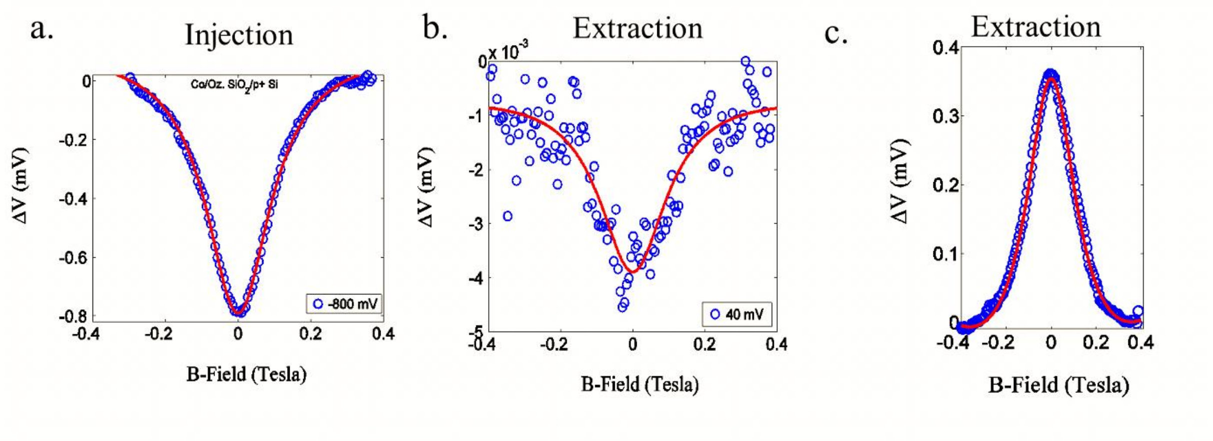

Figure 4.14. Hanle Lorentzian curve for spin injection and extraction for Co/Oz. SiO2/p+ Si at (-/+)800 mV bias showing normal spin signal and at +40 mV bias showing spin reversal. However, all spin reversal signals were noisy and extracted life-times were also less compared to normal signal.

For medium doped sample Co/Oz. SiO2/p+ Si, both hole spin injection and extraction were successfully done however, unusual behavior of spin signal, reversing of sign of spin signal, was observed below +140 mV i.e. during spin extraction, shown in figure 4.14. The detailed treatment about this effect is discussed in the section 4.3. Other complete information about Hanle signal amplitude, spin polarizarion, spin RA, spin lifetime, etc. are shown in bias dependent plots.

Bias Dependent plots

For each bias voltage, the magnitude of spin accumulation was detected and variations of electrical Hanle signal (ΔV) and the spin RA product (ΔV/J) of the Co/SiO2/p+ Si are shown in figure 4.15 (a) and figure 4.15 (b) respectively. Both figures depict strong bias dependence which are asymmetric with respect to voltage polarity. The Hanle signal increases gradually with the reverse bias (spin holes injection V_{Si}-V_{FM} < 0) however, reversal of spin signals were seen in the forward bias (spin holes extraction, 150 mV >V_{Si}-V_{FM} > 0). It increases slowly with forward bias and reaches maximum at +75 V and becomes zero at around +140 mV. Then above +140 V, normal extraction Hanle signal was observed with slow increment with higher forward bias.

Spin RA product decays with increase in forward bias (V_{Si}-V_{FM} > 0) while it is almost constant with increase in reverse bias (V_{Si}-V_{FM} < 0) . Bias dependence spin polarization has been shown in figure 4.15 (c). With increase in Hanle spin signal amplitude, spin polarization also increases and vice-versa. Normalized TSP^2 shown in figure 4.15 (d) is decreasing rapidly during spin hole extraction while it is almost constant during spin hole injection. Spin lifetime for different bias are shown in figure 4.15 (e) which is on average around 50 ps.

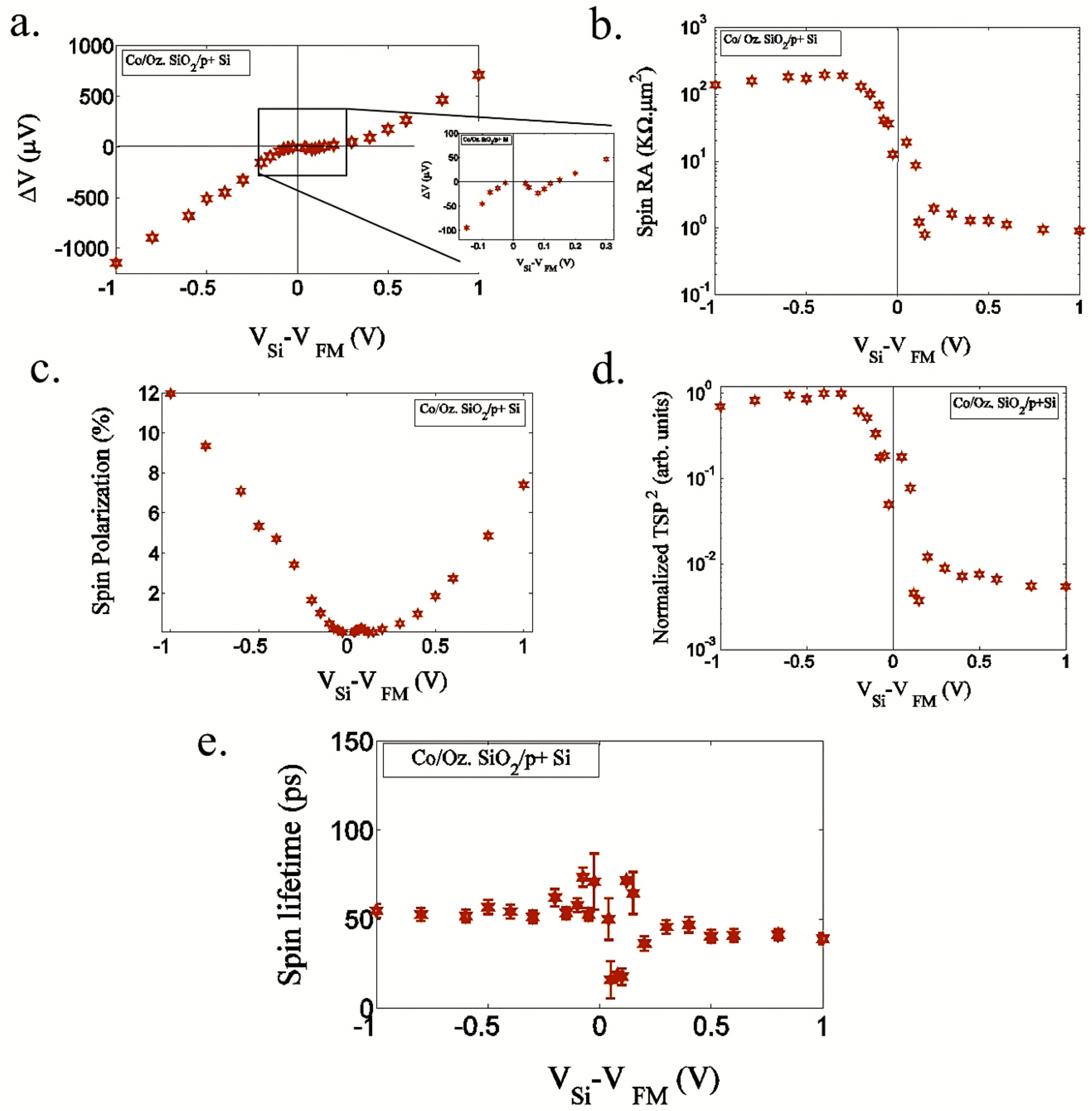

Figure 4.15. Bias dependence plots for Co/Oz. SiO2/p+ Si, (a) Variation of spin signals with bias voltage for Co/SiO2/p+ Si, measured at 295 K. Bias asymmetry Hanle signal amplitude and spin signal reversal are shown, (b) Spin RA product $\Delta V/J$,which is showing bias asymmetry feature. (c) Spin polarization varying with bias. It is linearly increase with bias, significantly during injection but slowly during extraction. (d) Normalized TSP^2 at room temperature (e) Spin lifetime variation with bias.

4.3.2.2. Low doped p Silicon

For low doped sample Co/Oz. SiO2/p Si, both hole spin injection and extraction were successfully done however, unusual behavior of spin signal, changing of sign of spin signal, was observed for both spin injection and spin extraction during low bias regime (-600 mV < V_{Si}-V_{FM} < 400 mV). This means, with increase in Schottky barrier width, the effect is becoming more prominent, which can be due to the dominant two steps tunneling with the effect of localized states at the interface.

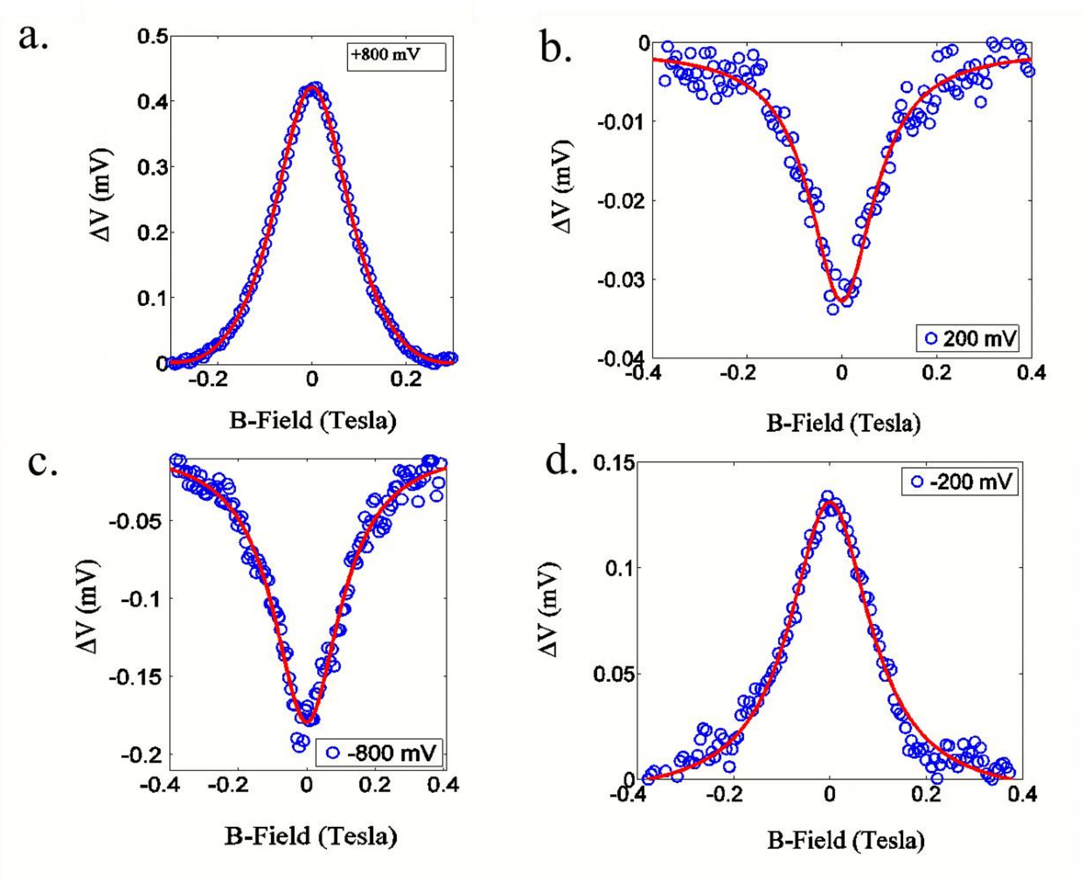

Figure 4.16. Hanle Lorentzian curve for spin injection and extraction for Co/Oz. SiO2/p+ Si at (-/+)800 mV bias showing normal spin signal and at (-/+)40 mV bias showing spin reversal, a. Normal spin extraction at 800 mV bias b. Spin reversal at 200 mV c. Normal spin injection at -800 mV bias d. Spin reversal at -200 mV.

Bias Dependent plots

For each bias voltage, the magnitude of spin accumulation was detected and variations of electrical Hanle signal (ΔV) and the spin RA product (ΔV/J) of the Co/SiO2/p Si are shown in

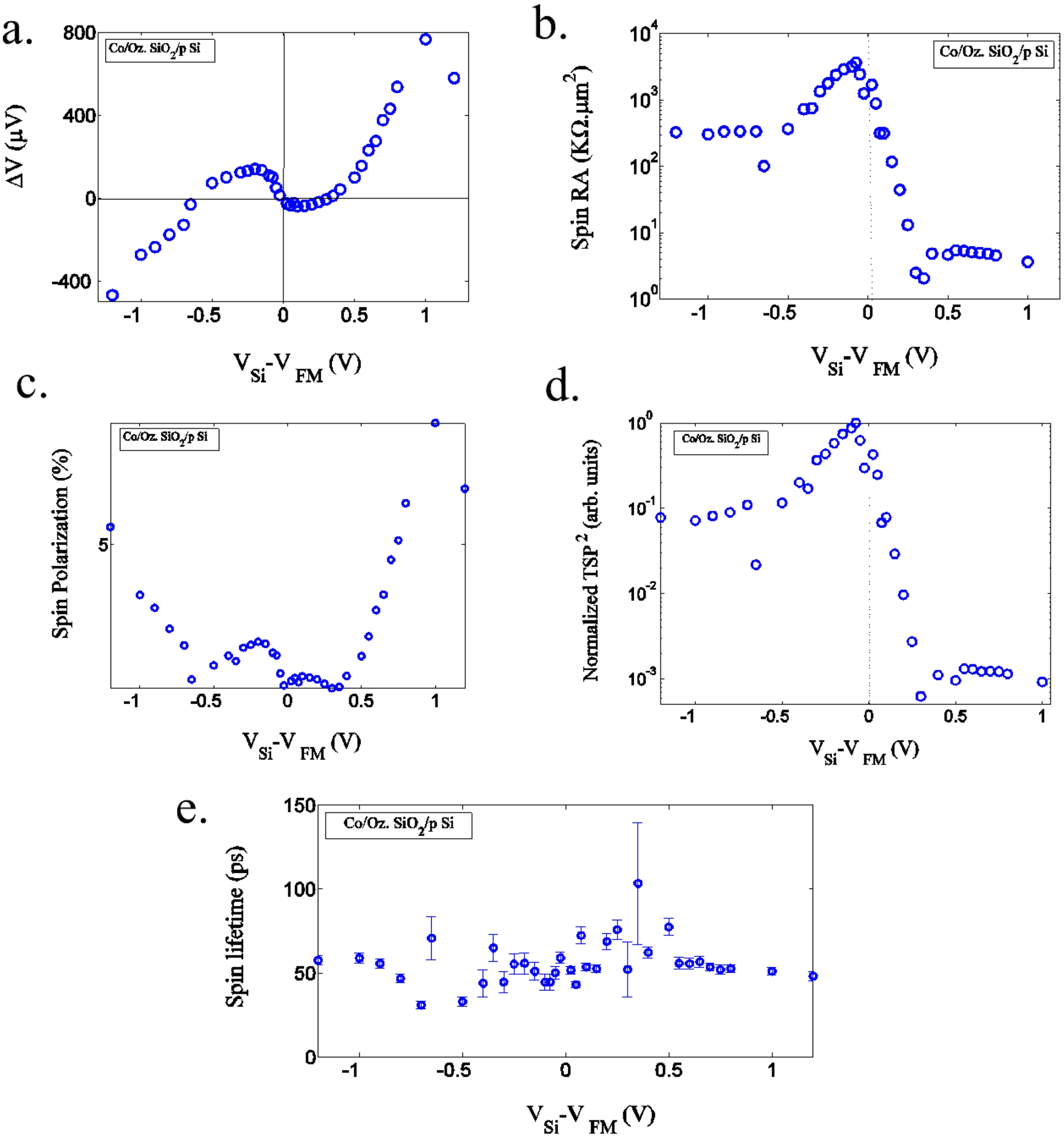

Figure 4.17. Bias dependence plots for Co/Oz. SiO2/p+ Si, (a) Variation of spin signals with bias voltage for Co/SiO2/p++Si, measured at 295 K. Bias asymmetry Hanle signal amplitude and spin signal reversal are shown, (b) Spin RA product $\boldsymbol{\Delta V/J}$,which is showing bias asymmetry feature. (c) Spin polarization varying with bias. It is linearly increase with bias, significantly during injection but slowly during extraction. (d) Normalized TSP^2 at room temperature (e) Spin lifetime variation with bias.

figure 4.17 (a) and figure 4.17 (b) respectively. Both figures depict strong bias dependence which are asymmetric with respect to voltage polarity. The Hanle signal increases gradually with the reverse bias (spin holes injection V_{Si}-V_{FM} < 0) however, reversal of spin signals were seen during the reverse low bias regime, which reaches maximum at around -200 mV, decreases gradually and crosses zero at around -600 mV. Then, it increases in normal direction gradually with bias above -600 mV. Also, for forward bias (spin holes extraction, V_{Si}-V_{FM} > 0), sign reversal of spin accumulation was observed during low bias regime, which reaches maximum at around +150 mV, decreases gradually and crosses zero at around +350 mV. Then, above +350 V, normal extraction Hanle signals were observed with significant increment with higher forward bias. Spin RA product decays rapidly with increase in forward bias (V_{Si}-V_{FM} > 0) while it is decreasing slowly with increase in reverse bias (V_{Si}-V_{FM} < 0) . Bias dependence spin polarization has been shown in figure 4.17 (c). With increase in Hanle spin signal amplitude, spin polarization also increases and vice-versa. Normalized TSP^2, as shown in figure 4.17 (d), is decreasing rapidly during spin hole extraction while decreasing slowly during spin hole injection. Spin lifetime for different bias are shown in figure 4.17 (e) which is on average around 50 ps.

4.3.2.4. Very low doped p- Silicon

Then, fabrication was done for very low doped p- Si whose doping concentration was 1.34×10^{15} cm^{-3}. Surprisingly, spin injection was not successful because of extremely large Schottky barrier width which further increases with reverse bias. However, spin extraction process was successfully detected which contradict our previous assumption that there is no possibility of observing spin extraction unless there is spin injection. As, spin injection signal (majority spin accumulation) are larger than spin extraction (minority spin accumulation), it used to say that spin extraction Hanle signal can only be observed when there is a detection of spin injection Hanle signal. Hanle signal for sample Co/Oz. SiO_2/p-Si is shown in figure 4.18, which clearly depicts that spin extraction signal can be observed first, mostly because of decreased barrier height and also, due to thinner Schottky barrier width, being forward biased case. Schottky barrier width during reverse bias is very large from where we could hardly expect any tunneling.

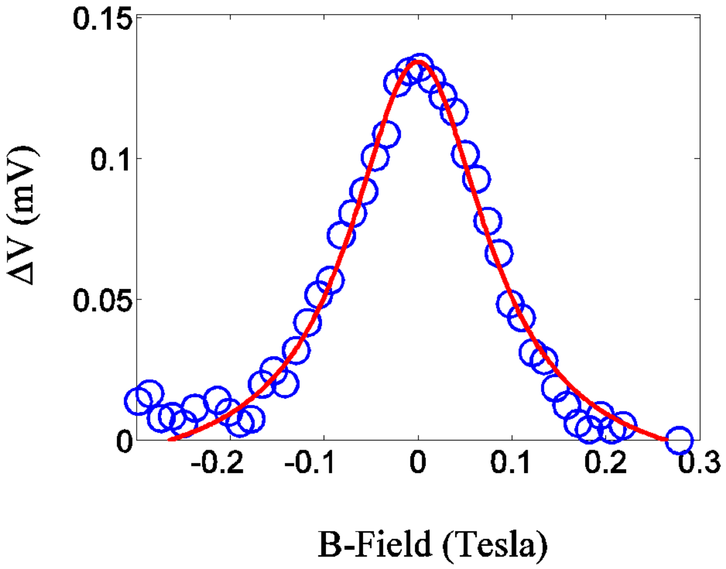

Figure 4.18. Hanle plot for spin extraction from sample Co/Oz. SiO_2/p-Si interface at room temperature. Applied bias voltage is 500 mV and Hale signal amplitude ΔV, is found to be 140 V. Spin lifetime calculated from HWHM was 63 ps.

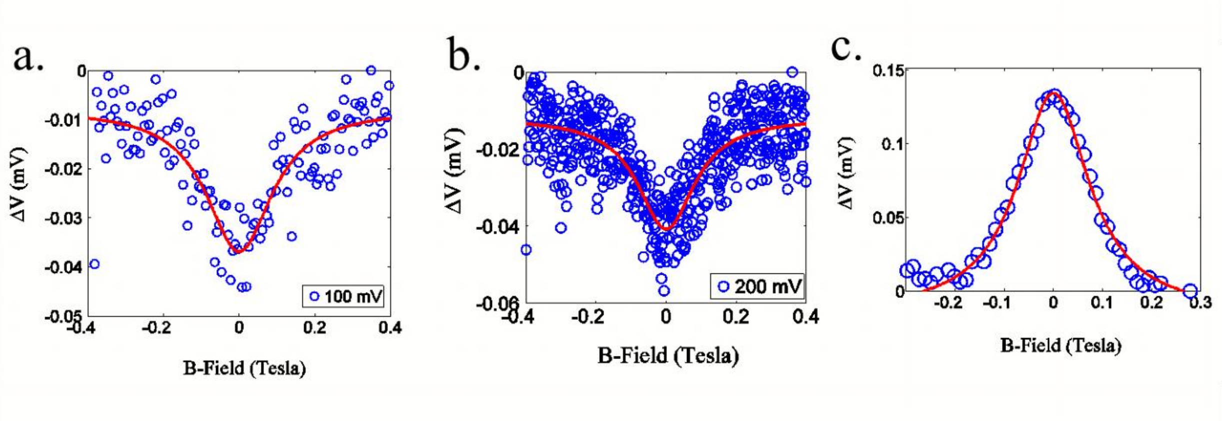

Figure 4.19. Hanle plot for spin extraction from sample Co/Oz. SiO_2/p- Si interface showing sign reversal Hanle signal at a. bias 100 mV b. bias 200 mV and normal Hanle signal at c. bias 500 mV

Sign reversal phenomena were even observed for this device. At lower bias for spin hole extraction, i.e. forward bias (+300 mV > V_{Si}-V_{FM} > 0), Hanle signals were just opposite to the normal Hanle signal for spin hole extraction, shown in figure 4.19. However, Hanle signals detected were very noisy as compared to Normal Hanle signal. This even supports the fact that at larger Schottky barrier resistance due to larger Schottky barrier width, something strange phenomena is dominating from the interface. We could think most probably the effect of localized states at the interface which already have created so many problems in semiconductor devices. Detail treatment is done in next section to explain about this weird behavior of spin accumulation signal.

4.3.2.5. Detailed comparison – Doping dependence

Complete comparison for three different doping namely p, p+ and p++ are shown in figure 4.19. Hanle signal was found to be increase with doping during spin injection whereas during spin extraction, just opposite is the case, as shown in figure 4.20. (a). It requires further detailed study to find out the exact reason. Also, spin reversal phenomena were eliminated partly for p+ doping and completely for p++ doping. Spin RA signal is decreasing with increase in doping concentration as shown in figure 4.20. (b), which is basically due to increase in current through the ferromagnetic tunnel junction with decrease in junction resistance, as shown in figure 4.20. (e). Change in junction resistance with doping is mainly due to change in Schottky barrier width.

Spin polarization, as shown in figure 4.20. (c), is found to increase in doping due to increase in current injection with reduced junction resistance. There is optimal doping concentration at which we will get maximum spin polarization, above which scattering limits its value. Normalized TSP^2, as shown in figure 4.20.(d), is decreasing rapidly during spin extraction and it is varying weakly during spin injection for all kind of samples. About spin lifetime, it is found to be almost same for three different doping and average value is shown as 50 ps in figure 4.20. (f). This one is different than what we expect. In reality, spin lifetime should decrease with increase in doping because in Si, Elliot-Yafet spin relaxation mechanism is dominating which is due to series of scattering that increases with increase in doping. This means, spin lifetime is mainly dominated by ferromagnetic proximity effect.

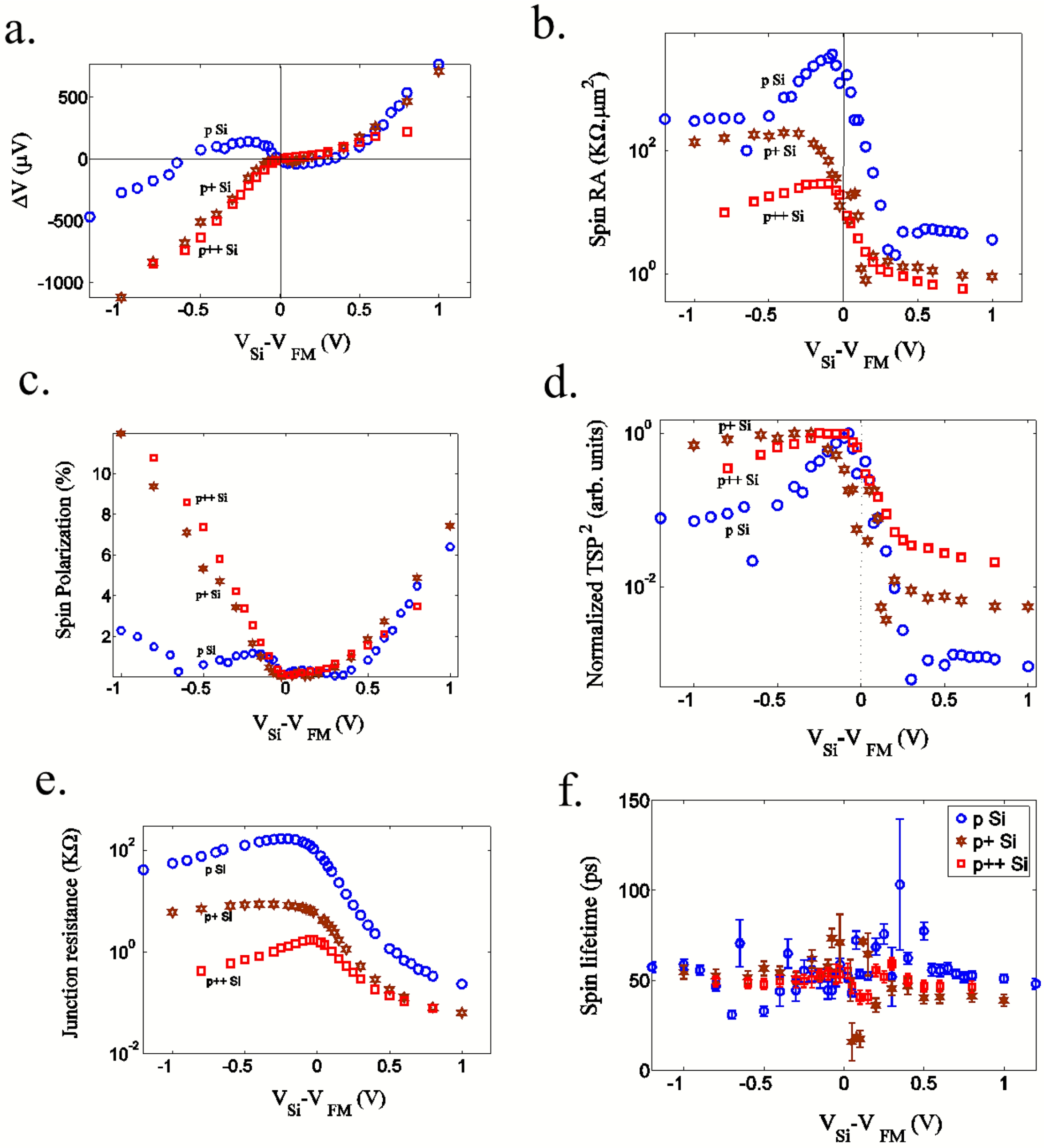

Figure 4.20. Comparison between three different doping samples for a. Bias dependent Hanle signal, b. Bias dependent spin RA signal, c. Bias dependent spin polarization, d. Bias dependent normalized TSP^2, e. Bias dependent junction resistance, f. Bias dependent spin lifetime.

4.3.3 Role of Localized states at the interface

So many theoretical and experimental studies have been done in the injection of spin polarized carriers from the ferromagnet to the semiconductor. However, the reverse process, the extraction of spin-polarized carriers from the semiconductor to the ferromagnet, has not been explored properly with the physics behind it. We have found that the amplitude of the extracted spin-polarized current is considerably smaller than the amplitude of injected spin-polarized current. Yuriy et. al. described about the concept of spin blocking effect [52], the accumulation of minority spins near the interface in the semiconductor side limits the majority spin current through the junction at the critical current level. It was described due to the presence of local spin dipole at the interface. We have found that localized states at the interface also plays significant role behind this discrepancy in amplitude.

Spin injection from ferromagnet to semiconductor was described with two-step, sequential transport model by Tran et. al. and has been attributed to the enhanced spin signals observed in experiments as compared to the theoretical predicted value [53]. It was predicted that localized states act as intermediate state for spin injection and spin accumulation $\Delta\boldsymbol{\mu}^{\mathbf{ls}}$, in the localized states can be much larger than the spin accumulation $\Delta\boldsymbol{\mu}^{\mathbf{ch}}$, induced in the semiconductor channel, under certain conditions. Very recently, Jansen et al. did some correction on Tran's model considering two-step tunneling via localized states in parallel with direct tunneling [51]. However, he emphasized about the enhancement role of localized states at the interface by the additional spin current through it and the measured Hanle signal in 3-T device is the weighted average of $\Delta\boldsymbol{\mu}^{\mathbf{ls}}$ and $\Delta\boldsymbol{\mu}^{\mathbf{ch}}$. Here, we have proposed that role of localized states at the interface can be different for spin current injection and spin current extraction, where accumulation of majority spin carriers and minority spin carriers occur in the semiconductor interface during spin injection and spin extraction respectively while in the localized states at the interface, role of majority spin carriers is dominant due to two-step tunneling.

4.3.1 Role of Localized states at the interface for Spin injection and extraction

We consider that measured Hanle signal amplitude from 3-Terminal device (FM/TB/SC) consists of both spin accumulation in semiconductor channel and spin accumulation in the localized states at the interface. For highly doped sample, Schottky barrier is very thin and the barrier resistance R_2 is very small so that there is coupling between spin resistance of localized states r_{ls}, and spin resistance of channel r_{ch}, below the interface.

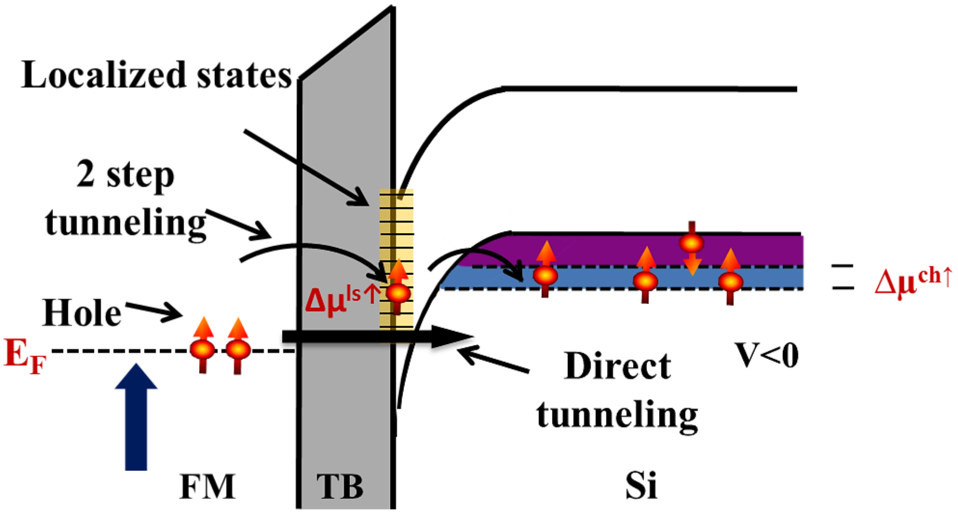

Figure 4.21. Spin hole injection from ferromagnet to semiconductor. During spin current injection, majority spin accumulation(↑) occurs in both localized states at the interface and semiconductor channel below the interface which leads to the enhanced Hanle signal amplitude.

As direct tunneling is dominant during higher bias regime for extraction and injection process, role of localized states are negligible. For reverse bias case (injection), Schottky barrier height is increasing with lowering of Fermi level but near the apex, barrier width is also decreasing and carriers can tunnel through thinner barrier near to the apex of the Schottky barrier. For forward bias case (extraction), Schottky barrier height and width are reduced and hence carriers tunnel through smaller Schottky barrier resistance. During spin injection, majority spin-holes (↑) are injected from ferromagnet into semiconductor by direct tunneling and also via localized states at the interface through sequential tunneling. Spin polarization occurs not only in semiconductor channel below the interface but also in the localized states at the interface. During spin current injection, majority spin accumulation occurs in both localized states at the interface and semiconductor channel below the interface which leads to the enhanced Hanle signal amplitude. During spin current extraction, we extract majority spin holes from semiconductor to ferromagnet by both direct and sequential tunneling. However, spin accumulation in the semiconductor channel below the interface is due to minority spin (↓) whereas spin accumulation in the localized states at the interface can be due to majority spin (↑), shown in figure 4.21 and 4.22. So, spin accumulation in the semiconductor channel below the interface and spin accumulation in the localized states at the interface are counteracting each other which can also be the one reason behind the smaller Hanle signal amplitude during spin electron extraction. One should note that direct tunneling dominates at higher bias and smaller Schottky barrier resistance.

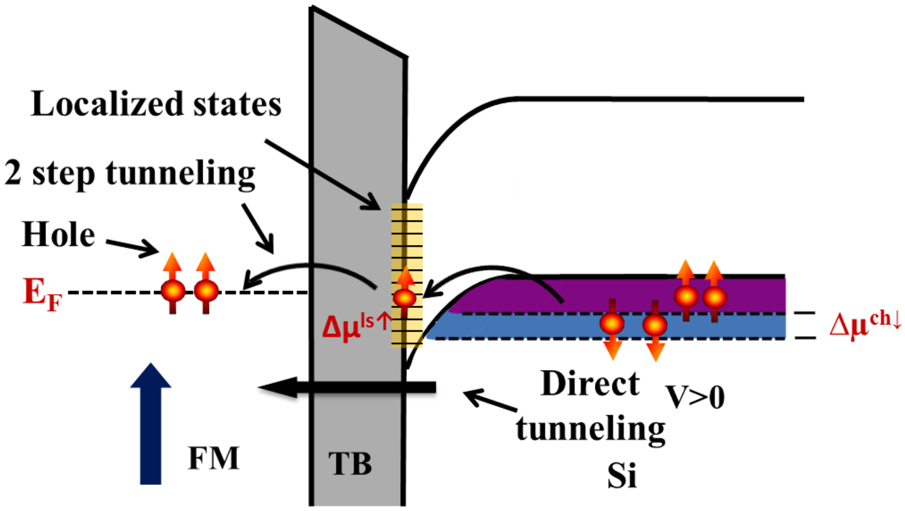

Figure 4.22. Spin hole extraction from semiconductor to ferromagnet. During spin current extraction, we extract majority spin holes from semiconductor to ferromagnet by both direct and sequential tunneling. However, spin accumulation in the semiconductor channel below the interface is due to minority spin (↓) whereas spin accumulation in the localized states at the interface can also be due to majority spin (↑)

For sample (Co/Oz. SiO2/p++ Si) with Si doping $p=2.1e^{19}$ cm^{-3} , during spin hole injection (reverse bias), spin accumulation at localized states and semiconductor channel below interface are $\Delta\mu^{ls}$ (↑) and $\Delta\mu^{ch}$ (↑) respectively, where ↑ indicates for majority spin, contributing the net spin accumulation. So, in this case we can expect majority spin accumulation with enhancement. During spin extraction (forward bias), spin accumulation at localized states and semiconductor channel below interface are $\Delta\mu^{ls}$ (↑) and $\Delta\mu^{ch}$ (↓) respectively, where ↑ and ↓ represent majority and minority spin respectively, counteracting each other. So, there is competition between $\Delta\mu^{ls}$ (↑) and $\Delta\mu^{ch}$ (↓) and this can also be one of the reasons behind smaller magnitude of spin extraction signal.

4.3.2 Spin reversal during spin extraction at lower bias

Anomalous spin reversal behavior was already been observed by Lou et. al. [54] in n-GaAs during spin extraction. However, precise reason behind this phenomenon is still unknown. Dery et al. assumed the mechanism behind this anomalous behavior of bias dependent spin polarization was due to presence of bound states at the interface [55] which arises due to non-homogenous doping profile. Brief explanation about bound states was explained by Song et al [56]. It was mentioned that there is competition between escape current from bound states and tunneling current from the bulk semiconductor. When escape current dominates, spin reversal behavior is observed because minority spin escapes faster than majority spin. However, it was claimed that with increase in doping, the escape current dominates the forward J-V curve due to which the spin polarization in the semiconductor is always along the majority spin direction during extraction process, which is not valid in our experiment.

We have also found that the reversal of spin polarization at both lower reverse bias and lower forward bias regimes. During spin hole extraction, for sample Co/Oz. SiO2/p Si with Si doping p=5.4e^{18} cm^{-3} and Schottky barrier width of 13.52 nm, reversal of spin polarization was observed during both lower forward bias (spin hole extraction) and lower reverse bias (spin hole injection). Also, for sample Co/Oz. SiO2/p+ Si with B doping p+=1.5e^{19} cm^{-3} and Schottky barrier width of 8.26 nm, spin reversal phenomena were seen but only during lower forward bias with lower critical forward bias (+150 mV), above which normal Hanle signals were observed. However, for similar sample with B doping p++=2.1e^{19} cm^{-3} and Schottky barrier width of 7.02 nm, no sign reversal of spin polarization was observed. We assumed that, role of localized states at the interface was suppressed at that degenerately doping level. Role of localized states at the interface is significant only when a barrier with sufficiently large resistance R_2 (here, Schottky barrier with sufficient depletion width) separates the localized states at the interface from Semiconductor. Role of localized states at the interface is also bias dependent. Dery et. al assumed the mechanism behind this anomalous behavior of bias dependent spin polarization was due to presence of bound states at the interface which arises due to non-homogenous doping profile [55]. However, our samples have homogenous doping profile which depicts no role of any surface bound states on spin polarization reversal.

4.3.2.1 Proposed reason for spin reversal during extraction

Spin reversal during spin extraction is much easier to interpret. During spin extraction (forward bias), spin accumulation at localized states and semiconductor channel below interface are $\Delta\boldsymbol{\mu}^{\mathbf{ls}}$ (↑) and $\Delta\boldsymbol{\mu}^{\mathbf{ch}}$ (↓) respectively, where ↑ and ↓ represent majority and minority spin respectively, counteracting each other. So, there is competition between $\Delta\mu^{ls}$ (↑) and $\Delta\mu^{ch}$ (↓). Also, localized states are paramagnetic in nature. This means, during majority spin accumulation in the localized states at the interface, there can be enhanced spin accumulation due to exchange interaction. Also, it is said that escape time of spin carriers from localized states increases with decrease in doping density of silicon [56]. For lowly doped Si sample, the Schottky barrier resistance is significantly higher which can act as good spin filter like tunnel barrier and also cause spin to stay more inside localized state during two step tunneling. So, there is overall significant enhancement of spin accumulation inside localized states at interface and it becomes dominant at lower forward bias and hence, spin reversal occurs. However, for higher forward bias, direct tunneling is dominant, due to negligible Schottky barrier height and hence, role of localized states. Measured junction RA (Resistance Area product) at V_{Si}-V_{FM} = 200 mV for (Co/Oz. SiO2/p Si) sample is 27.62 x10^4 KΩ.µm^2, which is much higher than that at V_{Si}-V_{FM} = 800 mV given by 0.678 x10^4 KΩ.µm^2 shown in table no. 4.3. This difference has been attributed to the role of Schottky barrier.

Table 4.3. Junction RA, Tunneling RA and Spin RA against doping

Doping	Junction RA (KΩ.µm^2) @-200mV V_{Si}-V_{FM}	Junction RA (KΩ.µm^2) @+200mV V_{Si}-V_{FM}	Junction RA (KΩ.µm^2) @-800mV V_{Si}-V_{FM}	Junction RA (KΩ.µm^2) @+800mV V_{Si}-V_{FM}	Tunneling RA (KΩ.µm^2)	Spin resistance of channel r_{ch} (KΩ.µm^2)
p	338x10^4	27.62 x10^4	151.9 x10^4	0.678 x10^4	1 x10^4	5.74 x10^{-2}
p+	16.68 x10^4	2.26 x10^4	14.23 x10^4	0.164 x10^4	1 x10^4	2.71 x10^{-2}
p++	2.6 x10^4	1.068 x10^4	0.853 x10^4	0.156 x10^4	1 x10^4	1.41 x10^{-2}

With increase in doping, Schottky barrier resistance decreases, shown by decreased junction RA from 27.62 x10^4 KΩ.µm^2 to 1.068 x10^4 KΩ.µm^2 at V_{Si}-V_{FM} = 200 mV while increasing doping from p to p++. So, the effective spin filtering capability is reduced and there is strong spin coupling between localized states and Si channel below interface. This suppresses the localized spin accumulation and hence, direct tunneling dominates.

4.3.3. Spin reversal during spin injection at lower reversed bias

Reversal of spin polarization was seen at lower reverse biased condition for sample Co/Oz. SiO2/p Si. This was quite unexpected behavior and it is very hard to interpret about this behavior. Nobody have seen such spin reversal behavior during reverse biased condition before this experiment. Here, we try to correlate this behavior with Schottky resistance. From table 4.3., it can be seen that junction RA was reduced drastically from $338\text{x}10^4$ to KΩ.μm^2 16.68 $\text{x}10^4$ KΩ.μm^2 when doping concentration was increased from p to p+. For sample Co/Oz. SiO2/p+ Si, spin reversal behavior was not seen due to higher doping and sharp decrease in Schottky barrier resistance. So, is the case for sample Co/Oz. SiO2/p++ Si.

So, we assume that when there is very high Schottky barrier resistance during spin injection, there is dominant tunneling between ferromagnet and localized states at interface and the semiconductor channel is almost decoupled from localized states. Hence, there can be spin flipping in the localized states which causes minority spin accumulation there. At higher bias V_{Si}-V_{FM} = -800 mV, it was found that junction RA was reduced by half as compared to that at V_{Si}-V_{FM} = -200 mV and the spin signal was observed to normal direction at that higher bias. We need further research in this field to find out the exact reason.

4.3.2.1. Tunneling between Ferromagnet and Localized states

When Schottky barrier resistance R_2 is above critical resistance ($R_2 > R_2^*$), we assumed that tunneling between ferromagnet and localized states is significant which we should consider in the theoretical modeling too. Localized states at the interface includes so many defects, where interface defects Dit and trivalent Si defects Pb center are dominant defects.

Chang et al. explained about the importance of tunneling between interface states and metal in Metal-Insulator-Semiconductor (MIS) when the tunnel barrier thickness is less than 5 nm [57]. Gaussian like donor and acceptor states [58] was assumed and different occupation function for donor and acceptor states during accumulation, depletion and inversion modes were shown. From mid-gap to Valence band, there are donor interface states and from mid-gap to Conduction band, there are acceptor interface states Donor interface state is neutral when occupied by electron and becomes charged (positive) after donating an electron. Acceptor interface state is neutral when it is empty and becomes charged (negative) after accepting an electron.

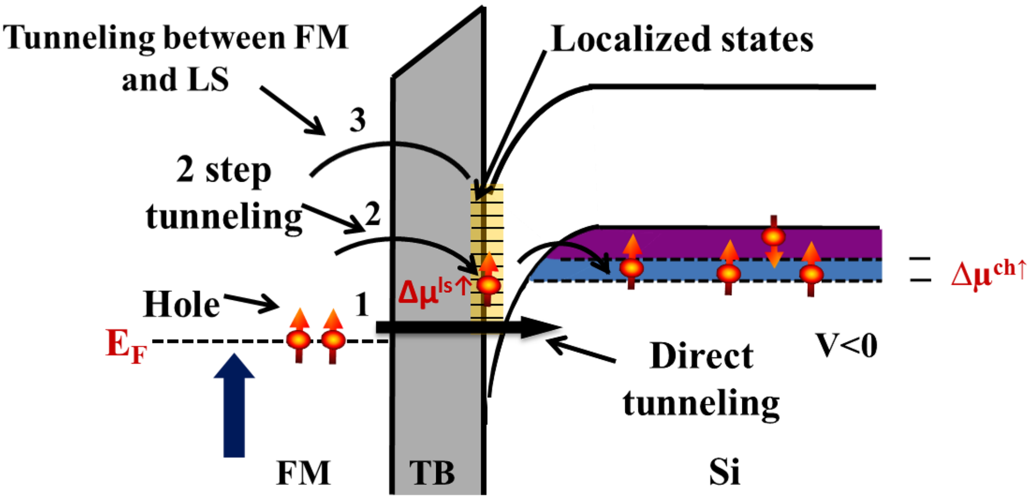

Figure 4.23. Three different cases for spin transport in FM/TB/SC device, 1. Direct tunneling between FM and Si, 2. Two-step tunneling, 3. Tunneling between FM and Localized states

For tunnel barrier thickness less than 5 nm, the occupation function of interface state in the MIS tunnel structure are quite different from that of recombination centers in the bulk of semiconductor which is mostly because of the tunneling process between metal and interface states [57]. For Larger than 5 nm oxide barrier, interface states behave similar to recombination centers. Tunneling of carriers between ferromagnet and interface states can also be one reason behind this spin reversal behavior. For exact reason to define, one must study properly about the role of interface states in semiconductor spintronic devices. Whether the donor and acceptor states are playing any roles or not regarding spin reversal behavior. It needs to be studied properly.

Also, Pb centers are paramagnetic in nature and they have found to be responsible for spin flipping process. Role of Pb centers can also be the reason behind this spin reversal process which is dominant when Schottky barrier resistance is very high. This also requires further research in this silicon spintronics.

So, we have defined three major types of spin transport shown in figure 4.23, which we should consider while modeling about the spin transport behavior.

1. Direct tunneling between FM and Si: It is dominant when Schottky barrier resistance is low (higher doping case). It is also dominant at higher bias even when Schottky barrier resistance is high. Mostly, direct tunneling is parallel to two-step tunneling.

2. Two step tunneling via localized states: When value of Schottky barrier resistance lies in certain range so that it can also act as good spin filter like tunnel barrier, two step tunneling is significant. It can play either enhancement role or suppressed role in getting spin accumulation signal, already discussed in section 4.3.2. It is not significant during higher bias regime.
3. Tunneling between FM and localized states: This one is dominant when Schottky barrier resistance is very high and applied bias is low. Acceptor and donor roles of interface states can be responsible for spin reversal behavior. Also, role of paramagnetic Pb centers can be correlated with spin reversal behavior.

Chapter 5

Conclusions & Outlook

In conclusion, large spin accumulation using SiO_2 tunnel barrier made by ozone oxidation method was successfully created inside highly doped (Boron concentration – $2.1 * 10^{19}$ cm^{-3}) p-type silicon. The polarization was found to be ~10 %. The lower limit of lifetime was found to be 50 ps on average. For different Boron doping concentration inside Si, average lifetime was found to be almost similar which indicates that the Hanle linewidth is artificially broadened by external factors such as stray field due to roughness of ferromagnet-tunnel barrier interface. Hence, it supports that actual spin lifetime is greater than measured lifetime from Hanle effect.

Weak temperature dependence of spin signal in highly dope Si indicates that there is true spin accumulation inside Si over full temperature range and there is not any amplification of spin signals due to interface states.

With the change of Boron doping concentration inside silicon, the Schottky barrier resistance was varied by changing Schottky barrier width and the spin transport behavior for spin injection and extraction processes were observed successfully. Spin accumulation was found to be increasing with doping concentration because of reduced Schottky barrier resistance that leads to large current injection inside silicon. Schottky barrier resistance higher than lower critical resistance results in dominant two-step tunneling spin transport which can results in anomalous spin signal reversal behavior during spin extraction process at lower bias regime. If Schottky barrier resistance is higher than upper critical resistance, then spin signal reversal behavior is observed during lower reversed bias regime also. It seems like that, localized states at the interface, which are paramagnetic in nature, are playing major role in creating this anomalous spin reversal behavior. For large doping and higher bias regime, contribution of Schottky barrier for junction resistance was found to be very low which indicates dominant direct tunneling spin transport due to which normal sign spin signals were observed during full bias range of injection and extraction processes. Overall, we can say that the Schottky barrier resistance is determining the spin transport behavior, which can be dominated by either direct tunneling or two-step tunneling. Local spin dipole formation at the interface during two step tunneling on extraction process can be considered as one reason behind less magnitude of spin extraction signal than that of spin injection for the same bias.

To understand the full effects of localized states at the interface, mainly the effect of interface states, Dit, and trivalent Si defects, Pb centre, we need to do further research in this field. Spin flipping at the Pb center have been found by using electron spin resonance measurement. So, how Pb centers can effect this spin accumulation during injection and extraction should be studied properly. This also requires generating improved models for semiconductor spintronic fields so that we can have experimental values similar to theoretical ones. The change of the tunnel barrier resistance can also be made by varying tunnel barrier thickness and the change in the regime of spin sign reversal phenomena can be observed. This helps to observe the competition between the tunnel barrier resistance and Schottky barrier resistance in determining the spin transport behavior.

Bibliography

[1] N. F. Mott, *Proc. Roy. Soc.,* vol. 153, p. 699, 1936.

[2] N. F. Mott, *Proc. Roy. Soc.,* vol. 156, p. 368, 1936.

[3] A. Fert and I. Campbell, *Phys. Rev. Lett.,* vol. 21, p. 1190, 1968.

[4] A. Fert and I. Campbell, *J. Phys. F,* vol. 6, p. 849, 1976.

[5] S. Datta and B. Das, *Appl. Phys. Lett.,* vol. 56, p. 665, 1990.

[6] G. Lampel, *Phys. Rev. Lett.,* vol. 20, p. 491, 1968.

[7] R. Jansen, *Nature Mat.,* vol. 11, p. 400, 2012.

[8] B. T. Jonker, G. Kioseoglou, A. T. Hanbicki, C. H. Li and P. E. Thompson, *Nature Phys.,* vol. 3, p. 542, 2007.

[9] S. P. Dash, S. Sharma, R. S. Patel, M. P. de Jong and R. Jansen, *Nature,* vol. 462, p. 491, 2009.

[10] K. R. Jeon, B. C. Min, Y. H. Jo, H. S. Lee, I. J. Shin, C. Y. Park, S. Y. Park and S. C. Shin, *Phys. Rev. B,* vol. 84, p. 165315, 2011.

[11] P. M. Tedrow and R. Meservey, *Phys. Rev. Lett.,* vol. 26, p. 192, 1971.

[12] M. Julliere, *Phys. Lett. A,* vol. 54, p. 225, 1975.

[13] D. Hagele, M. Oestreich, W. W. Ruhle, N. Nestle and K. Eberl, *Appl. Phys. Lett.,* vol. 73, p. 1580, 1998.

[14] J. M. Kikkawa and D. D. Awschalom, *Nature,* vol. 397, p. 139, 1999.

[15] J. M. Kikkawa and D. D. Awschalom, *Phys. Rev. Lett.,* vol. 80, p. 4313, 1998.

[16] C. Chappert, A. Fert and F. N. Van Dau, *Nature Mat.,* vol. 6, p. 813, 2007.

[17] I. A. Campbell, A. Fert and A. R. pomeroy, *Phil. Mag.,* vol. 15, p. 977, 1967.

[18] R. J. Soulen, *Science*, vol. 282, p. 85, 1998.

[19] A. Jain, "Injection de spin dans le germanium," *Phd. Thesis, University of Grenoble,* 2011.

[20] A. T. Filip, B. H. Hoving, F. J. Jedema, B. J. van Wees, B. Dutta and S. Borghs, *Phys. Rev. B,* vol. 62, p. 9996, 2000.

[21] G. Schmidt, D. Ferrand, L. W. Molenkamp, A. T. Filip and B. J. van Wees, *Phys. Rev. B,* vol. 62, p. 4790, 2000.

[22] E. I. Rashba, *Phys. Rev. B,* vol. 62, p. 16267, 2000.

[23] R. Klasges, C. Carbone and W. Eberhardt, *Phys. Rev. B,* vol. 56, p. 10801, 1997.

[24] B. C. Min, K. Motohashi, J. C. Lodder and R. Jansen, *Nature Mater.,* vol. 5, p. 817, 2006.

[25] B. C. Min, J. C. Lodder, R. Jansen and K. Motohashi, *J, Appl. Phys.,* vol. 99, p. 08S701, 2006.

[26] A. Fert and H. Jaffres, *Phys. Rev. B,* vol. 64, p. 184420, 2001.

[27] H. Jaffres and A. Fert, *J. Appl. Phys.,* vol. 91, p. 8111, 2002.

[28] A. Fert, J. M. George, H. Jaffres and R. Mattana, *IEEE Trans. Elec. Dev.*, vol. 54, p. 921, 2007.

[29] S. Yuasa and D. D. Djayaprawira, *J. Phys. D: Appl. Phys.,* vol. 40, p. R337, 2007.

[30] J. Nitta, T. Akazaki, H. Takayanagi and T. Enoki, *Phys. Rev. Lett.,* vol. 78, p. 1335, 1997.

[31] J. Fabian, A. Matos-Abiague, C. Ertler, P. Stano and I. Zutic, *Acta Physica Slovaca,* vol. 57, p. 565, 2007.

[32] S. P. Dash, S. Sharma, J. C. Le Breton, J. Peiro, H. Jaffres, J.-M. George, A. Lemaitre and R. Jansen, *Phys. Rev. B,* vol. 84, p. 054410, 2011.

[33] Y. Yafet, *Phys. Rev.,* vol. 85, p. 478, 1952.

[34] R. J. Elliott, *Phys. Rev.,* vol. 96, p. 266, 1954.

[35] G. Feher and E. A. Gere, *Phys. Rev.,* vol. 114, p. 1245, 1959.

[36] I. Zutic, J. Fabian and S. D. Sarma, *Rev. Mod. Phys.,* vol. 76, p. 323, 2004.

[37] B. V. Zeghbroeck, "Principle of semiconductor devices," *URL http://ecee.colorado.edu/~bart/book/start.htm,* Accessed 2012-06-01.

[38] [Online]. Available: http://www.memsnet.org/mems/processes/deposition.html. [Accessed May 2012].

[39] C. K. Fink, K. Nakamura, S. Ichimura and S. J. Jenkins, *J. Phys. Condens. Matter,* vol. 21, p. 183001, 2009.

[40] N. Kameda, T. Nishiguchi, Y. Morikawa, M. Kekura, H. Nonaka and S. Ichimura, *J. Electrichem. Soc.,* vol. 154, pp. 8181-6, 2007.

[41] [Online]. Available: http://wwwold.ece.utep.edu/research/webedl/cdte/Fabrication/index.htm. [Accessed May 2012].

[42] [Online]. Available: http://www.ionbeammilling.com/about_the_ion_milling_process. [Accessed May 2012].

[43] E. H. Hall, *American Journal of Mathematics,* vol. 2(3), p. 287, 1879.

[44] C. Kittel, Introduction to Solid State Physics, 8 ed., John Wiley & Sons, 2005.

[45] L. J. van der Pauw, *Philips Research Reports,* vol. 13(1), p. 1, 1958.

[46] S. M. Sze and K. K. Ng, Physics of Semiconductor Devices, 3 ed., John Wiley & Sons, 2007.

[47] R. van de Walle, R. L. van Meirhaeghe, W. H. Lafkre and F. Cardon, *J. Appl. Phys.,* vol. 74(3), p. 1885, 1993.

[48] E. H. Rhoderick and R. Williams, in *Metal-Semiconductor Contacts*, vol. 48, Clarandon Press, Oxford University Press, 1988, p. 20.

[49] K. Potje-Kamloth, *Chem. Rev.,* vol. 108, p. 367, 2008.

[50] S. O. Valenzuela, D. J. Monsma, C. M. Marcus, V. Narayanamurti and M. Tinkham, *Phys. Rev, Lett.,* vol. 94, p. 196601, 2005.

[51] R. Jansen, M. Deac, H. Saito and S. Yuasa, *Phys. Rev. B,* vol. 85, p. 134420, 2012.

[52] V. P. Yuriy and M. D. Ventra, *Phys. Rev.,* vol. 75, p. 193301, 2007.

[53] M. Tran, H. Jaffres, C. Deranlot, J. M. George, A. Fert, A. Miard and A. Lemaitre, *Phys. Rev. Lett.,* vol. 102, p. 036601, 2009.

[54] X. Lou, C. Adelmann, S. A. Crooker, E. S. Garlid, J. Zhang, K. S. M. Reddy, S. D. Flexner, C. I. Palmstrom and P. A. Crowell, *Nat. Phys.,* vol. 3, p. 197, 2007.

[55] H. Dery and L. J. Sham, *Phys. Rev. Lett.,* vol. 98(4), p. 046602, 2007.

[56] Y. Song and H. Dery, *Phys. Rev. B,* vol. 81, p. 045321, 2010.

[57] C. Y. Chang and S. J. Wang, *Solid-St. Electron,* vol. 28, p. 1181, 1985.

[58] E. Poon and W. Hwang, *Solid-St. Electron,* vol. 25, p. 699, 1982.